MAX-PLANCK-INSTITUT
FÜR METEOROLOGIE

IMPRS-ESM
International Max Planck Research School on Earth System Modelling

# Illuminating convective cold pools with a dense station network

Bastian Kirsch

Hamburg 2022

Berichte zur Erdsystemforschung
*Reports on Earth System Science*

257
2022

## Hinweis

Die Berichte zur Erdsystemforschung werden vom Max-Planck-Institut für Meteorologie in Hamburg in unregelmäßiger Abfolge herausgegeben.

Sie enthalten wissenschaftliche und technische Beiträge, inklusive Dissertationen.

Die Beiträge geben nicht notwendigerweise die Auffassung des Instituts wieder.

Die "Berichte zur Erdsystemforschung" führen die vorherigen Reihen "Reports" und "Examensarbeiten" weiter.

## Anschrift / Address

Max-Planck-Institut für Meteorologie
Bundesstrasse 53
20146 Hamburg
Deutschland

Tel./Phone: +49 (0)40 4 11 73 - 0
Fax: +49 (0)40 4 11 73 - 298

name.surname@mpimet.mpg.de
www.mpimet.mpg.de

## *Notice*

*The Reports on Earth System Science are published by the Max Planck Institute for Meteorology in Hamburg. They appear in irregular intervals.*

*They contain scientific and technical contributions, including PhD theses.*

*The Reports do not necessarily reflect the opinion of the Institute.*

*The "Reports on Earth System Science" continue the former "Reports" and "Examensarbeiten" of the Max Planck Institute.*

## *Layout*

*Bettina Diallo and Norbert P. Noreiks*
*Communication*

## *Copyright*


*Photos on the back from left to right:*
*Christian Klepp, Jochem Marotzke,*
*Christian Klepp, Clotilde Dubois,*
*Christian Klepp, Katsumasa Tanaka*

# Illuminating convective cold pools with a dense station network

Bastian Kirsch

Hamburg 2022

Bastian Kirsch
aus Winsen, Deutschland

Max-Planck-Institut für Meteorologie
The International Max Planck Research School on Earth System Modelling
(IMPRS-ESM)
Bundesstrasse 53
20146 Hamburg

Tag der Disputation: 27. September 2022

Folgende Gutachter empfehlen die Annahme der Dissertation:
Prof. Dr. Felix Ament
Dr. Cathy Hohenegger

Vorsitzender des Promotionsausschusses:
Prof. Dr. Hermann Held

Dekan der MIN-Fakultät:
Prof. Dr.-Ing. Norbert Ritter

Titelfoto: Bastian Kirsch



ISSN 1614-1199 - doi: 10.17617/2.3432702

*If the doors of perception were cleansed*
*every thing would appear to man as it is,*
*Infinite.*

— William Blake (1793)

This document was typeset using `classicthesis` developed by André Miede and Ivo Pletikosić available at https://bitbucket.org/amiede/classicthesis/.

# PREFACE

The main part of this cumulative dissertation is a unifying essay that discusses the essence of three studies forming the basis of this work. The essay includes an introduction into the overarching scientific gap it aims to fill, summarizes and interprets the findings of the studies in a larger scientific context, and provides an overall conclusion. The three studies and two published data sets are explicitly listed on page xi. The studies are added as appendices and my contribution to each of them is stated at the beginning of the respective appendix.

# ABSTRACT

Cold pools are mesoscale bodies of cool and dense air that form underneath precipitating clouds and spread horizontally on the Earth's surface. Lifting of environmental air at their leading edge constitutes the importance of cold pools for the development and organization of atmospheric convection. Although being explicitly represented in hectometer-scale numerical simulations, cold pools and especially their spatial properties are hardly captured by existing observation systems. This dissertation presents a comprehensive characterization of cold pools in Germany, discusses factors controlling their strength, and describes the Field Experiment on Sub-mesoscale Spatio Temporal Variability in Lindenberg (FESSTVaL) that determines the morphology of cold pools (i. e., their size, shape, and structure) for the first time ever using in situ observations.

The first part presents a preparatory study on the analysis of nearly 500 cold pool passages at a 280-m high tower in Hamburg (northern Germany) observed over 14 years. The sampled cold pools most likely occur in July and in the afternoon. The near-surface temperature perturbation $\Delta T$ exhibits a median of -3.3 K and can be as strong as -10.8 K. $\Delta T$ is more strongly correlated with the saturation deficit of the pre-event air mass ($r = -0.71$) than with the event-accumulated rainfall amount ($r = -0.35$), emphasizing that the cold pool strength is mainly controlled by evaporative cooling by precipitation. This process becomes occasionally superposed by the downward transport of upper-level air masses in convective downdrafts.

The second part describes the realization of FESSTVaL that took place at the Meteorological Observatory Lindenberg – Richard Aßmann Observatory (MOL-RAO) in eastern Germany from May to August 2021. The experiment featured a dense network of 99 measurement stations at sub-mesoscale resolution ($\mathcal{O}(100)$ m – $\mathcal{O}(10)$ km) that covered a circular area of about 30 km in diameter. For this purpose, novel, custom-designed Autonomous cold POoL LOgger (APOLLO) stations equipped with fast-response air temperature and pressure sensors as well as supplementary Weather Transmitter (WXT) stations were developed, which proved to operate reliably. The impacts of the COVID-19 pandemic delayed the main experiment by one year and motivated the implementation of the precursor experiment FESST@HH in Hamburg during summer 2020, which was facilitated by the support of volunteers.

The last part focuses on the evaluation of the FESSTVaL and FESST@HH data sets. The spatial interpolation of the $\Delta T$ signals allows to define individual cold pool objects. The derived sample of about 1300 cold pool objects during 39 events exhibits a median size of 8.4 km, whereas the size of cold pools increases with their strength. Contrarily to common assumption, the cold pools are not circularly shaped, which is independent of their size and strength. The analysis of four selected events suggests that cold pools grow linearly with the spatially-integrated rainfall accumulation and cool most efficiently early in their life cycle, confirming the cold air production by precipitation.

This dissertation demonstrates that dense station networks illuminate the previously obscured morphology of cold pools and allow to more precisely describe the underlying processes required for the validation and improvement of weather and climate simulations. Furthermore, the work provides valuable guidance for the implementation of future measurement campaigns.

# ZUSAMMENFASSUNG

Cold Pools sind mesoskalige Körper kalter und dichter Luft, die sich unterhalb regnender Wolken bilden und horizontal an der Erdoberfläche ausbreiten. Durch die Hebung umgebender Luftmassen an ihrer Vorderseite sind Cold Pools von großer Bedeutung für die Entwicklung und Organisation von atmosphärischer Konvektion. Obwohl sie explizit in Hektometer-skaligen numerischen Simulationen dargestellt werden können, werden Cold Pools und insbesondere ihre räumlichen Eigenschaften nur unzureichend von bereits existierenden Beobachtungssystemen erfasst. Diese Dissertation präsentiert eine umfassende Charakterisierung von Cold Pools in Deutschland, diskutiert Einflussfaktoren für ihre Stärke und beschreibt die Messkampagne *Field Experiment on Sub-mesoscale Spatio Temporal Variability in Lindenberg* (FESSTVaL), die erstmals überhaupt die Morphologie von Cold Pools, d. h. ihre Größe, Form und Struktur, mithilfe von In-situ-Beobachtungen bestimmt.

Der erste Teil präsentiert eine vorbereitende Studie zur Auswertung von nahezu 500 Cold-Pool-Durchgängen an einem 280 m hohen Messturm in Hamburg (Norddeutschland), die über einen Zeitraum von 14 Jahren beobachtet wurden. Die untersuchten Cold Pools treten am häufigsten im Juli und am Nachmittag auf. Die bodennahe Temperaturstörung $\Delta T$ weist einen Median von -3.3 K auf und erreicht eine Stärke von bis zu -10.8 K. $\Delta T$ ist stärker mit dem Sättigungsdefizit der Luftmasse vor dem Ereignis korreliert ($r = -0.71$) als mit der akkumulierten Regenmenge des Ereignisses ($r = -0.35$), was unterstreicht, dass die Cold-Pool-Stärke im Wesentlichen von Verdunstungsabkühlung durch Niederschlag bestimmt wird. Dieser Prozess wird in Einzelfällen durch den Abwärtstransport von darüberliegenden Luftmassen in konvektiven Abwinden überlagert.

Der zweite Teil beschreibt die Durchführung des Messexperimentes FESSTVaL, das von Mai bis August 2021 am Meteorologischen Observatorium Lindenberg – Richard-Aßmann-Observatorium (MOL-RAO) im Osten Deutschlands stattfand. Das Messexperiment zeichnete ein dichtes Netzwerk aus 99 Messstationen in sub-mesoskaliger Auflösung ($\mathcal{O}(100)$ m – $\mathcal{O}(10)$ km) aus, das ein kreisförmiges Gebiet mit 30 km Durchmesser abdeckte. Zu diesem Zweck wurden neuartige, anwendungsspezifische *Autonomous cold POoL LOgger* (APOLLO)-Stationen mit trägheitsarmen Sensoren für Lufttemperatur- und druck sowie ergänzende *Weather Transmitter* (WXT)-Stationen entwickelt, deren zuverlässiger Betrieb nachgewiesen wurde. Die Auswirkungen der COVID-19-Pandemie verzögerten das Hauptexperiment um ein Jahr und begründeten die Umsetzung des Vorläuferexperimentes FESST@HH in Hamburg im Sommer 2020, welches durch die Unterstützung Freiwilliger ermöglicht wurde.

Der letzte Teil behandelt die Auswertung der Datensätze von FESSTVaL und FESST@HH. Die räumliche Interpolation des $\Delta T$-Signals erlaubt es individuelle Cold-Pool-Objekte zu definieren. Die analysierte Stichprobe mit etwa 1300 Cold-Pool-Objekten aus 39 Ereignissen weist eine Median-Größe von 8.4 km auf, wobei die Größe der Cold Pools mit ihrer Stärke zunimmt. Im Widerspruch zur verbreiteten Annahme sind die Cold Pools nicht kreisrund geformt, was unabhängig von ihrer Größe und Stärke gilt. Die Analyse von vier ausgewählten Ereignissen deutet darauf hin, dass Cold Pools linear mit der räumlich integrierten akkumulierten Niederschlagssumme wachsen und sich zu Beginn ihres Lebenszyklus am effizientesten abkühlen, was die Kaltluftproduktion durch Niederschlag bestätigt.

Diese Dissertation unterstreicht, dass dichte Messnetze die vormals unbekannte Morphologie von Cold Pools beleuchten und es ermöglichen die zugrundeliegenden Prozesse präziser zu beschreiben, was notwendig für die Validierung und Verbesserung von Wetter- und Klimasimulationen ist. Darüber hinaus gibt die Arbeit wertvolle Hinweise für die Umsetzung zukünftiger Messkampagnen.

# PUBLICATIONS RELATED TO THIS DISSERTATION

## Appendix A

**Kirsch, Bastian**, Felix Ament, and Cathy Hohenegger (2021). "Convective cold pools in long-term boundary layer mast observations." In: *Mon. Weather Rev.* 149.3, pp. 811–820. DOI: 10.1175/MWR-D-20-0197.1. © American Meteorological Society. Used with permission.

## Appendix B

**Kirsch, Bastian**, Cathy Hohenegger, Daniel Klocke, Rainer Senke, Michael Offermann, and Felix Ament (2022). "Sub-mesoscale observations of convective cold pools with a dense station network in Hamburg, Germany." In: *Earth Syst. Sci. Data* 14.8, pp. 3531–3548. DOI: 10.5194/ESSD-14-3531-2022.

## Appendix C

**Kirsch, Bastian**, Cathy Hohenegger, and Felix Ament (2022). "The morphology and growth of convective cold pools in a dense station network." *in preparation*.

## DATA SETS

**Kirsch, Bastian**, Cathy Hohenegger, Daniel Klocke, Rainer Senke, Michael Offermann, and Felix Ament (2021). *FESST@HH meteorological network measurements, version 00-2*. Integrated Climate Data Center, Universität Hamburg. DOI: 10.25592/UHHFDM.10172.

**Kirsch, Bastian**, Cathy Hohenegger, Daniel Klocke, and Felix Ament (2022). *Meteorological network observations by APOLLO and WXT weather stations during FESSTVaL 2021, version 00-2*. Integrated Climate Data Center, Universität Hamburg. DOI: 10.25592/UHHFDM.10179.

# ACKNOWLEDGMENTS

Every PhD project undergoes a certain development as its focus is modified and sharpened to adapt to newly achieved results or unforeseen complications. However, when I started this project in January 2019, I could have never envisioned what would happen throughout the following 3½ years and how this dissertation would actually look like. First ideas of what should become FESSTVaL 2020 date back to (at least) 2017. However, in spring 2020 the COVID-19 pandemic turned the world upside down, transformed our established mode of working within days, and made all plans for the experiment obsolete. Within two intense and challenging months, the home-office experiment FESST@HH was conceived and realized, which not only unexpectedly provided me with an extra data set but also made my PhD a truly unique and exciting journey, completed by the very successful FESSTVaL 2021.

First of all, I thank my primary supervisor Felix Ament for always providing valuable scientific and non-scientific advice but even more importantly for being my mentor, meaning to help me to put things into perspective and to remind me to appreciate also the small achievements. I also thank my secondary supervisor Cathy Hohenegger for being a reliable source of scientific guidance and for inspiring and challenging me with her ideas and feedback. Moreover, I am thankful to Dirk Notz for serving as a conscientious and helpful chair of my PhD advisory panel and to Antje Weitz and the IMPRS office for assisting with organizational issues.

Several further people made essential contributions to the success of my PhD project, which I want to acknowledge. First to mention here is Rainer Senke whose dedication and technical know-how needed to create the APOLLO stations provided the basis for the realization of the two experiments. Next, the hands-on work and logistical planning by Ingo Lange and Marco Clemens were crucial to bring the instruments (efficiently) into the field and to keep them running. I am also thankful to Sarah Wiesner and Kristina Lundgren for smoothly organizing the experiments and everything related to it. Furthermore, I thank the entire FESSTVaL community from all over Germany and the DWD staff at Lindenberg, especially Frank Beyrich, for making the experiments and four-year project phase such a successful and joyful experience.

Beyond that, doing a PhD is not only about science. First, I have to emphasize the importance of the AMPM group that is my scientific home for seven years now. I am very thankful for the regular stand-up meetings with Amelie, Finn, Henning, Jule, Tobi, and our scrum master Heike, which became a fixed appointment in my daily schedule and helped me through two winters of endless home office and video meetings. Similarly, the Tuesday Wettermast meeting was the ideal place to discuss new results and ideas but also to chat away on random topics. I also thank Moritz and Theresa for helping to assemble the instruments in productive and enjoyable lab sessions before and during the lockdown. And thank you, Marco, for the supply with coffee and the seat on your couch.

I am very thankful to Amelie, Frosi, Henning, and Lucas for reading through earlier versions of this manuscript and for proving me with many helpful and valuable tips for improvement.

Finally, I thank my family for constantly supporting me although I am pretty sure they were not always fully understanding what I am actually doing here. And most importantly, thank you Lucas, Janne, and Frosi for always being there for me.

# CONTENTS

# ACRONYMS

| | |
|---|---|
| **APOLLO** | Autonomous cold POoL LOgger |
| **FESST@HH** | Field Experiment on Sub-mesoscale Spatio Temporal variability at Hanseatic city of Hamburg |
| **FESSTVaL** | Field Experiment on Sub-mesoscale Spatio Temporal Variability in Lindenberg |
| **HOPE** | HD(CP)$^2$ Observational Prototype Experiment |
| **LCZ** | local climate zone |
| **MOL-RAO** | Meteorological Observatory Lindenberg – Richard Aßmann Observatory |
| **NTC** | negative temperature coefficient |
| **WMH** | Weather Mast Hamburg |
| **WXT** | Weather Transmitter |

# Part I

# UNIFYING ESSAY

# 1 INTRODUCTION

## 1.1 COLD POOLS IN ATMOSPHERIC CONVECTION

*Warm air rises, cold air sinks.*

This simplified version of Archimedes' principle can be considered as common knowledge and is a fundamental mechanism in the Earth system. The principle is not only essential to maintain the balance of heat, moisture, and momentum in the atmosphere but is also the main cause for atmospheric motion on various spatial scales (Fernando, 2003). As the most prominent example, horizontal differences in the net input of radiative energy between the equator and the poles drive the global-scale general circulation of the atmosphere (Stull, 2017). On much smaller scales, thermally direct circulations in the form of vertical and highly turbulent motion of buoyant air are referred to as convection (Emanuel, 1994). In case of moist convection, rising air masses lead to the condensation of atmospheric water vapor and become apparent by the formation of clouds. For deep updrafts, also precipitation, i. e., liquid rain drops, solid ice particles, or any combination of both phases, forms inside the cloud and eventually falls to the ground. Strong convection in the form of thunderstorm clouds is often accompanied by hazardous phenomena like heavy rainfall, hail, lightning, wind gusts, and tornadoes (Stull, 2017).

While the upward branch of the convective overturning circulation produces spectacular and beautiful clouds that are hard to overlook, the downward branch is rarely visible and attains much less attention although being at least equally important. When rain drops and melting ice particles fall through the cloud and into the atmospheric sub-cloud layer, they reach drier, under-saturated air masses and start to re-evaporate (Figure 1.1). This process cools and moistens the environmental air, which becomes negatively buoyant and sinks down to the surface. The outflow air hits the surface and spreads horizontally away from the precipitation area forming a body of cold and dense air, referred to as a cold pool. At the leading edge of the propagating cold pool front, lighter environmental air eventually gets lifted and forms a new cloud, initiating a new convective life cycle (Figure 1.2).

As the formation of cold pools is directly linked to atmospheric convection, their appearance is similarly small-scale, short-lived, and highly variable. Since cold pools constantly grow throughout their life cycle, and the areal coverage of convection itself varies considerably between different events, the size of cold pools reported in numerical (Romps and Jeevanjee, 2016; Tompkins, 2001) and observational studies (Feng et al., 2015; Terai and Wood, 2013) ranges from less than 10 km to up to several hundreds of km (Zuidema et al., 2017). These length scales are commonly referred to as the atmospheric mesoscale (Orlanski, 1975). Accordingly, the typical life time of cold pools is in the order of hours (Feng et al., 2015; Romps and Jeevanjee, 2016; Tompkins, 2001). By definition, cold pools are characterized by a lower air temperature than their environment and, consequently, a higher air density. The hydrostatic cooling effect, i. e., the additional weight of the cooler air in the atmospheric column, also leads to an increase in air pressure. Further pressure excess is caused by the downward drag of falling precipitation particles on the air, called liquid-water loading or ice loading, and a dynamical component when

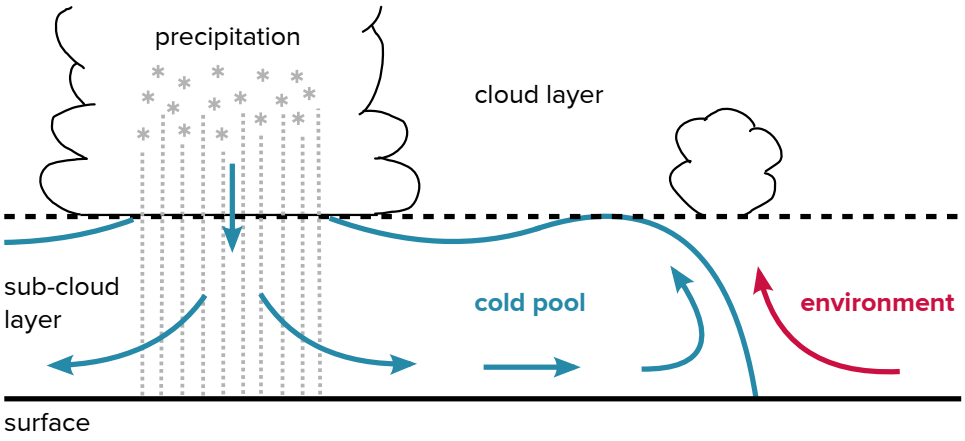


Figure 1.1: Schematic of cold pool formation: Precipitation (liquid rain drops or solid ice particles; gray dots and asterisks) forms inside a convective cloud, falls into the sub-cloud layer, and cools the air by evaporation. The pool of cold and dense air propagates horizontally on the Earth's surface (blue arrows), forms a vertical circulation at its leading edge, and lifts warmer environmental air (red arrow), which eventually triggers a new convective cloud.

the descending air hits the ground. The horizontal pressure difference pushes the cold pool air outwards and drives the propagation on the Earth's surface, which is usually compared to a so-called density current. A distinct gust front and a vertical circulation called head, which reaches higher than the rest of the cold pool body, often form at the leading edge of the air mass boundary (as indicated in Figure 1.1; Markowski and Richardson, 2010; Stull, 2017). The horizontal differences in temperature, pressure, and wind speed between a cold pool and its environment strongly vary from event to event and can reach magnitudes of more than 10 K, 5 hPa, and 15 $m\,s^{-1}$, respectively (e. g., Engerer et al., 2008; Feng et al., 2015; Goff, 1976). One important factor for the variability in cold pool strength, as discussed later in this dissertation, is the thermodynamical potential for evaporation of the atmosphere, i. e., its temperature and humidity. This is one reason why cold pools over land are found to be generally stronger than over oceans (Zuidema et al., 2017).

## 1.2 SIGNIFICANCE OF COLD POOLS

The interest in cold pools is justified by their critical role in initiating new convection and shaping its appearance. Rotunno et al. (1988) found an interplay between cold pools and low-level wind shear that systematically controls the strength and longevity of line-shaped convection. The leading edge of a cold pool front is proven to be a location of preferential triggering of new convection due to mechanical lifting by the dense air masses, moisture accumulation in the lower atmosphere (Feng et al., 2015; Tompkins, 2001; Torri et al., 2015), and collisions with other cold pool fronts (Meyer and Haerter, 2020; Torri and Kuang, 2019). Cold pools also favor the transition from shallow (i. e., weak) to deep (i. e., strong) convection, since they support the formation of wider and deeper clusters that are less diluted by the turbulent import of dry environmental air (Boeing et al., 2012; Khairoutdinov and Randall, 2006; Schlemmer and Hohenegger, 2014). Moreover, cold pools are believed to critically impact the process of convective self-aggregation, which describes the spontaneous segregation of an initially homogeneous atmosphere into cloudy and

Figure 1.2: Cloud formation at the leading edge of a thunderstorm outflow south-east of Hamburg (Germany) on 27 June 2020 at 20:50 CEST (photograph by the author).

cloud-free areas and is a important factor for the distribution of clouds in the atmosphere (Haerter, 2019; Jeevanjee and Romps, 2013; Nissen and Haerter, 2021; Wing, 2019).

The understanding of processes related to atmospheric convection, cold pool formation, and their interplay has several critical implications. Due to evolving computational resources over the past decades, numerical simulations at the km-scale and below are able to directly resolve convective clouds and precipitation on regional domains (Stevens et al., 2020) and even globally (Satoh et al., 2019). In this context, cold pools have shown to impact the correct simulation of the diurnal cycle of precipitation (Kurowski et al., 2018; Rio et al., 2009) and total rainfall amounts (Grant and Heever, 2015). Since the representation of convection propagates to the large-scale evolution of numerical weather prediction models (Peters et al., 2019), it is a critical factor for short-term weather forecasts, especially given the potentially hazardous and life-threatening impacts of severe weather caused by strong thunderstorms. Furthermore, clouds have been identified as an essential albeit very uncertain parameter for climate sensitivity and projecting global warming (Nuijens and Siebesma, 2019; Siebesma et al., 2020). Current research especially focuses on oceanic shallow cumulus clouds and their interplay with atmospheric circulations including cold pools, which is believed to have a substantial impact on Earth's radiation budget and global-mean cloud feedbacks (Bony et al., 2017). In conclusion, cold pools are not only crucial to understand and correctly represent atmospheric convection in numerical simulations but their role in determining the distribution of clouds also makes them a key component in the changing climate of our Earth.

## 1.3 OBSERVATIONAL BLIND SPOT

Highly resolved information in space and time is required to appropriately describe the characteristics of cold pools due to their small-scale and transient appearance. Modern hectometer-scale numerical simulations, often referred to as Large-Eddy simulations, have been established as a standard tool to conveniently and comprehensively approach scientific questions related to cold pools. Accordingly, our knowledge about the morphology of cold pools, i. e., their size, shape, and structure, as well as their evolution in time is mostly based on such high-resolution simulations, often applied on idealized setups. Consistent with observational evidence, the reported sizes of simulated cold pools range

from below 5 km (Drager et al., 2020) to several tens of km (e. g., Romps and Jeevanjee, 2016; Tompkins, 2001). This does not only reflect the highly dynamic character of cold pools but also the variety of parameters that can be used for the cold pool identification, e. g., temperature, buoyancy, or radial wind velocity (Drager and van den Heever, 2017). The shape of cold pools is often assumed to be circular (e. g., Haerter et al., 2019; Meyer and Haerter, 2020; Romps and Jeevanjee, 2016), but Torri and Kuang (2019) also found that they quickly lose their initially circular shape as they grow and merge into larger clusters. The most poorly determined spatial property of cold pools is their structure. While for theoretical considerations often a uniform temperature is assumed (e. g., Romps and Jeevanjee, 2016), other simulation-based studies find a ring-like structure, which is attributed to the gust front formation and moisture accumulation at the leading edge of cold pools (e. g., Langhans and Romps, 2015; Zuidema et al., 2017). However, the recent findings are still inconsistent regarding the fact if cold pools are coldest in their centers (Drager et al., 2020) or at their boundaries (Meyer and Haerter, 2020).

Also several observational studies aim at describing the size, life cycle, and horizontal and vertical structure of cold pools based on stationary point measurements (e. g., Engerer et al., 2008; Goff, 1976; Kruse et al., 2022; Touzé-Peiffer et al., 2022; Vogel et al., 2021), aircraft observations (Terai and Wood, 2013), or ship observations (Feng et al., 2015). In a recent study, van den Heever et al. (2021) introduced a measurement campaign that characterized the spatial variability of cold pool temperature on scales between $\mathcal{O}(100)$ m and $\mathcal{O}(1)$ km using uncrewed aerial systems, radiosondes, and three closely-spaced surface stations. Although these studies apply a large variety of approaches to describe the spatial characteristics of cold pools and provide valuable results, this challenging task was not yet satisfactorily addressed. A common weakness of observational studies dedicated to cold pools is that the limited number of measurement points does not allow to capture the extent and structure of cold pools. Furthermore, the analyzed samples of events are either biased to strong events (Engerer et al., 2008) or focus on single, strong events (Borque et al., 2020). Therefore, we lack reliable in situ observations of the horizontal dimension of cold pools that cover a wide range of intensities and event types (i. e., weak, strong, isolated, or widespread convection). As a consequence, the morphology of cold pools as found in numerical simulations or being used as a starting point for theoretical considerations cannot be sufficiently validated, which considerably limits our understanding of cold pools and the factors controlling their characteristics.

## 1.4 NEW APPROACH

Since cold pools are mesoscale phenomena with typical sizes between $\mathcal{O}(1)$ km and $\mathcal{O}(100)$ km, observations that appropriately capture their horizontal structure need to cover length scales of about one order of magnitude smaller, i. e., $\mathcal{O}(100)$ m – $\mathcal{O}(10)$ km. We refer to these scales as the sub-mesoscale, formally part of the meso-$\gamma$ and micro-$\alpha$ scale (Orlanski, 1975). Conventional meteorological station networks, e. g., the operational surface network of the German Weather Service, have a typical resolution of 25 km, i. e., mesoscale resolution. The delicate trade-off between spatial resolution and coverage required for a measurement setup especially dedicated to cold pool observations might be the main reason why such a challenging and ambitious enterprise was not yet realized to date. In this dissertation, I present the Field Experiment on Sub-mesoscale Spatio Temporal Variability in Lindenberg (FESSTVaL) that addresses this scientific gap. The main idea of this measurement campaign is to describe the morphology of cold pools (size, shape, and structure) for the first time using in situ observations of a sub-mesoscale network of

measurement stations especially designed for this purpose. The fundamental hypothesis that the present work aims to test is the following:

*A dense observational station network at sub-mesoscale resolution is suitable to enhance our understanding of cold pools.*

More specifically, I will elaborate on the following research questions:

- What new information on cold pool characteristics does a dense station network provide compared to single-point observations?
- Which factors control the strength and size of cold pools?
- What challenges are related to the operation of a dense station network and evaluation of its observations?

The answers to these questions will not only help to test our established conceptual model of the appearance of cold pools but also to illuminate potentially new properties that were previously obscured by the insufficient resolution and coverage of existing observation networks. This dissertation approaches the task in the following way: Chapter 2 introduces a statistical characterization of cold pool passages based on multi-year observations at a boundary layer tower that serves as a reference for the single-point view on cold pools and design of the experiment (Study A). Chapter 3 describes the implementation and organizational challenges related to the realization of FESSTVaL, including its preceding Field Experiment on Sub-mesoscale Spatio Temporal variability at Hanseatic city of Hamburg (FESST@HH) in summer 2020 (Study B) and the main experiment in summer 2021 (Study C). Chapter 4 presents preliminary results of the experiments according to unpublished analyzes of Study C, followed by a summary and interpretation of the overall findings as well as perspectives of the unique data sets in Chapter 5.

# 2 COLD POOLS IN LONG-TERM TOWER OBSERVATIONS

Cold pools are a common meteorological phenomenon. At a given location, cold pool front passages are as frequently observed as summery rainfall or thunderstorms occur. By definition, the arrival of an air mass cooler than the present one becomes evident by a drop in local air temperature. In case of a cold pool, such event typically takes place on a time scale of minutes and is accompanied by disturbances in air pressure, humidity, and wind speed. Although we know that these signals are characteristic for cold pool passages, their individual amplitude, sharpness, and even sign strongly vary between different events. The evaluation of single-point measurements is the classical and most convenient approach to describe cold pools in observations. Existing studies, however, restrict their analysis to small samples of pre-selected events (e. g., Goff, 1976) or specific types of events (usually strong convection; e. g., Engerer et al., 2008). As a new contribution, Study A uses multi-year tower observations that allow to robustly quantify the signal strength of cold pools over land, including their vertical dimension, over a wide range of meteorological conditions and event types. Additionally, the results provide a reference data set for the design of instruments to use in a dense station network during the FESSTVaL measurement campaign and for the interpretation of the spatial cold pool observations with respect to the single-point view.

## 2.1 CHARACTERIZATION OF COLD POOL PASSAGES

### 2.1.1 *Detection*

In Study A, we detect cold pool front passages based on co-located near-surface measurements of 2-m temperature $T_2$ and rainfall rate $R$. The algorithm designed for this investigation (Kirsch, 2020) identifies temperature drops of at least 2 K within 20 min as cold pool events if $R$ is non-zero within a period of 60 min after the begin of the temperature drop $t_0$. The amplitude of the temperature perturbation $\Delta T$ is defined as the difference between the minimum value within 60 min after $t_0$ and the median value of the 30-min period prior to $t_0$, meaning that $\Delta T$ is typically negative. In a similar fashion, we use this scheme to quantify the perturbations in further meteorological variables that go along with the temperature drop. This simple approach allows to objectively and consistently analyze cold pools in a multi-year data set with minimal assumptions on the type and strength of the signal.

The analysis method is applied on measurements performed at the Weather Mast Hamburg (WMH) observation site. The WMH is a 305-m high television broadcasting tower located in the eastern outskirts of Hamburg (northern Germany) that is equipped with meteorological sensors at heights between 2 m and 280 m above ground (Bruemmer et al., 2012). For the analysis, we use data of air temperature $T$, pressure $p$, specific humidity $q$, equivalent potential temperature $\Theta_e$, horizontal wind speed $U$, and vertical wind speed $w$ at five height levels (2 m [10 m for wind], 50 m, 110 m, 175 m, and 280 m) recorded at 1-min resolution during 14 extended summer seasons (1 April to 30 September) between 2006 and 2019.

### 2.1.2 *Occurrence of events*

The detection algorithm identifies a total number of 489 cold pool events for the 14-year period with an average of 34.9 events per summer season. While the yearly number of events varies randomly, the annual and diurnal cycles of occurrence show distinct peaks in July and at 15:00 local time, respectively (Figure 2.1). This as expected for phenomena related to convection over land, which is generally tied to the diurnal cycle of solar heating. Although the detection method does not consider information on the source of the temperature drops, this result confirms that the analysis is not severely contaminated by synoptic cold front passages, which occur randomly over the course of the day.

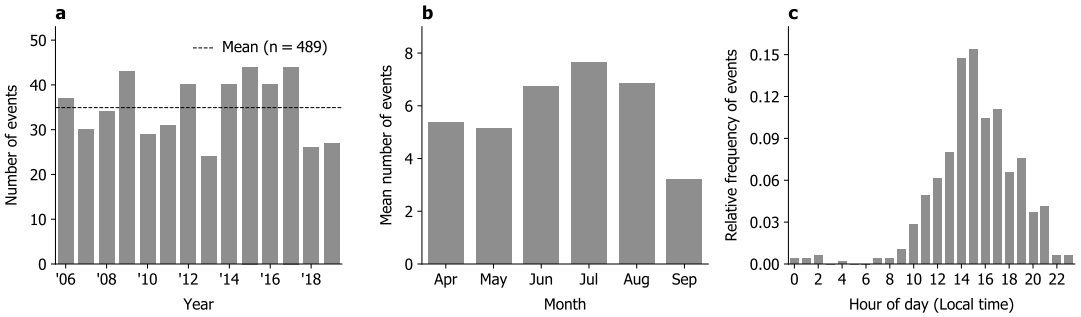


Figure 2.1: Occurrence of cold pool events detected at WMH between 2006 and 2019: (a) Number of events per summer season (1 April to 30 September), (b) mean annual cycle, and (c) mean diurnal cycle.

### 2.1.3 *Temperature perturbation*

A further look into the temporal and vertical temperature structure of the signal allows to better understand the characteristics of the sampled cold pool passages and related processes. The maximum temperature perturbation $\Delta T$ for all 489 cold pool events exhibits a median of -3.3 K near the surface (i. e., 2-m height) and reaches -10.8 K for the strongest event. The signal strength generally weakens with height, indicating a weaker vertical temperature decrease, i. e., more stable stratification, inside the cold pool than in its environment as expected. The mean time series of the signal shows that the temperature drop is strongest just after $t_0$ and reaches its largest amplitude after 20 to 25 min independent of the observation height (Figure 2.2a). However, the average temperature signal recovers only marginally at least 1 h after the initial drop, since the majority of events occurred in the afternoon, i. e., after the diurnal maximum of solar heating.

### 2.1.4 *Cold pool height*

Consistent with the hydrostatic relationship, the additional weight of the approaching dense air masses leads to an increase in air pressure (Figure 2.2b). The median amplitude $\Delta p$ at the surface for the sampled cold pools is 0.7 hPa and the strongest event reaches a signal of 5.9 hPa. Along with $\Delta T$, the amplitude of $\Delta p$ constantly decreases with height, since the hydrostatic pressure signal is only determined by the weight of the air column above a given level. Moreover, the decrease in $\Delta p$ is approximately linear and less affected by short-term fluctuations from local effects than $\Delta T$, which allows us to estimate the

vertical extent of the observed cold pool bodies. We define the cold pool height $h_{CP}$ (or referred to as cold pool *depth* in Study A) as the height where the linearly extrapolated pressure signal $\Delta p$ vanishes. This analysis reveals a median $h_{CP}$ of 746 m and values ranging between a few hundred meters and almost 2 km, which matches typical heights reported for continental convective outflows (Markowski and Richardson, 2010).

### 2.1.5 *Wind perturbation*

Cold pool passages go along with substantial disturbances of the local wind field. The horizontal wind speed experiences a median increase of 3.6 m s$^{-1}$ at 10-m height, which increases to 5.4 m s$^{-1}$ at 50 m and above. According to the mean time series, the wind speed maximum is confined to a distinct peak coinciding with the strongest temperature drop, reflecting the well-known gust front typically associated with convective outflows (Figure 2.2e). At heights of 110 m and above, a prominent peak in vertical wind speed a few minutes before $t_0$ becomes apparent, which is followed by a weaker and longer-lived peak of opposite sign (Figure 2.2f). This combination and timing of horizontal and vertical wind speed signatures clearly proves the existence of a lifting-induced overturning circulation at the leading edge being a critical factor for the importance of cold pools for triggering new convection.

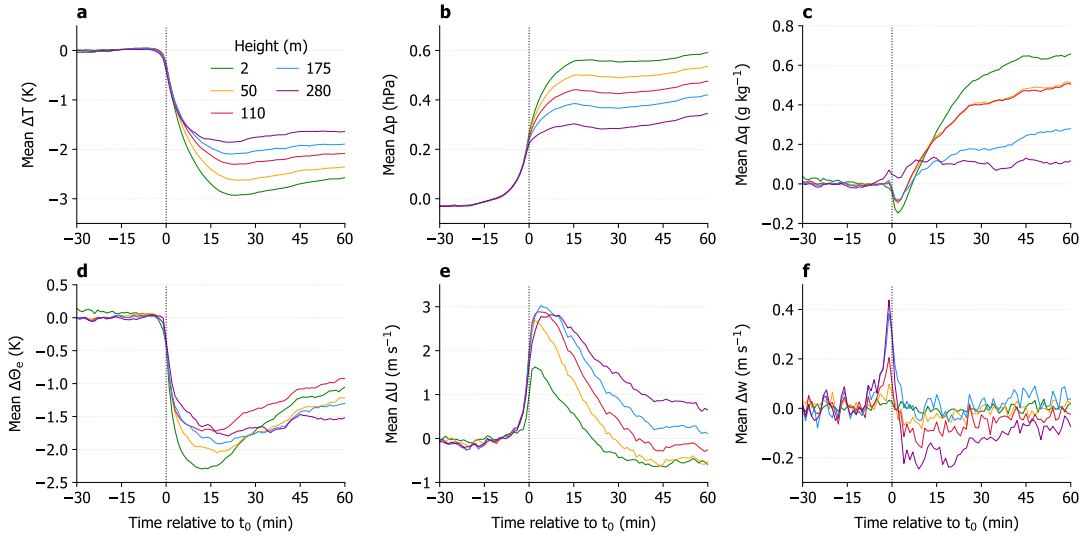


Figure 2.2: Height-dependent mean temporal evolution of (a) air temperature $T$, (b) pressure $p$, (c) specific humidity $q$, (d) equivalent potential temperature $\Theta_e$, (e) horizontal wind speed $U$, and (f) vertical wind speed $w$ relative to $t_0$ during cold pool passages at WMH between 2006 and 2019. Note that in (c) the temporary dip in $\Delta q$ just after $t_0$ is not of physical nature but can be attributed to an instrumental issue.

## 2.2 FACTORS FOR COLD POOL STRENGTH

The surface footprint of a cold pool observed at one point largely varies from event to event. The strength, here defined in terms of temperature perturbation $\Delta T$, of nearly 500 cold pool passages during 14 extended summer seasons ranges from the detection

threshold of -2 K to extreme cases of almost -11 K. Do we understand which factors control the observed cold pool strength?

### 2.2.1 *Evaporation of precipitation*

We know that cold pools are generated by evaporation of precipitation underneath convective clouds. In most simple terms, we would expect that a strong convective cell also produces a strong cold pool. A common measure to determine the strength of convection is rainfall. Since the typical life time of a cold pool is on the scale of hours, we consider the absolute rainfall accumulation over the 90-min cold pool event. Figure 2.3a shows that $\Delta T$ at 2-m height actually increases with the accumulated rainfall amount, which confirms the posed assumption. However, the decimal logarithm of the rainfall amount and $\Delta T$ are only moderately correlated for all 489 events according to a linear correlation coefficient $r$ of -0.35.

Another factor for evaporative cooling is the environment in which the precipitation falls. If an air mass is not saturated with water vapour, its potential for cooling by evaporation of additional water increases with decreasing relative humidity. Similarly, the absolute amount of evaporable water increases with the temperature of the air mass. Consequently, a warm and dry air mass provides the most favorable conditions for strong cooling by evaporation of precipitation. To measure both effects by a single parameter, we introduce the absolute saturation deficit $q_{\mathrm{sat}} - q$, given by the difference between saturation specific humidity and actual specific humidity. Similar to the rainfall amount, the strength of observed cold pool events constantly increases with higher saturation deficits near the surface averaged over a 30-min period prior to the event (Figure 2.3b). The higher correlation coefficient ($r = -0.71$) shows that the pre-event saturation deficit is actually a much better predictor for the temperature perturbation of a cold pool than the rainfall amount.

We further investigate the role of evaporation with a simple time-dependent thermodynamical model. The model takes the individual pre-event temperature and humidity conditions as input and simulates the idealized cooling and moistening process of the air mass assuming that an unlimited amount of rainfall is available for evaporation. When assuming that the evaporation process does not stop before the air is saturated, the simulated temperature drops agree reasonably well with the observed temperature drops according to $r = 0.67$. This value increases to $r = 0.80$, when we take into account how much the air was actually moistened during the cold pool passages (Figure 2.2c) and stop the simulated cooling process at this value. Therefore, we conclude that the thermodynamical potential for evaporative cooling explains at least 64 % of the variability in observed cold pool strength. This result is particularly impressive, since we do not use information on the actual precipitation that evaporated. It is also unclear where in the atmosphere the evaporation took place that caused the temperature signal and if the near-surface conditions are actually representative for this air mass.

### 2.2.2 *Convective downdrafts*

Although evaporative cooling explains large parts of the cold pool strength, it is not the only process relevant for the formation of convective outflows. When a given air mass is solely cooled by evaporation, its equivalent potential temperature $\Theta_e$ is conserved by definition. However, for the observed cold pool passages, $\Delta\Theta_e$ is generally not zero but

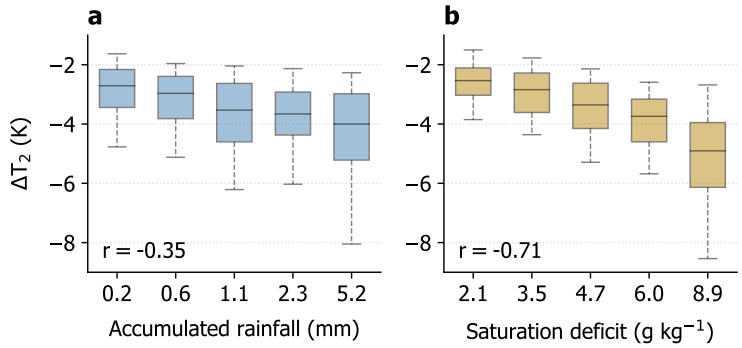


Figure 2.3: Distribution of cold pool 2-m air temperature perturbation $\Delta T_2$ dependent on (a) event-accumulated rainfall and (b) pre-event median saturation deficit $q_{\text{sat}} - q$. Box plots use 20-percentile interval bins labeled with the median values of each bin. Vertical lines, boxes, and whiskers mark the median, interquartile range, and the 5th/95th percentiles, respectively. The linear correlation coefficient $r$ indicated in (a) is calculated between the decimal logarithm of the rainfall amount and $\Delta T_2$.

exhibits on average a similar magnitude as $\Delta T$ (Figure 2.2d). The change in $\Theta_e$ indicates the arrival of an air mass different from the pre-convective state, which is most likely related to the vertical transport of mid-tropospheric air into the sub-cloud layer by downdrafts, i. e., downward currents of air that locally form inside strong precipitation. We show that the agreement between the observed cold pool strength and the strength simulated by the evaporation model is lower for events that experience a strong negative signal in $\Theta_e$ and vice versa. Therefore, the cooling signal during cold pool passages is determined both by evaporation of precipitation and vertical advection of potentially (i. e., height-corrected) cooler upper-level air masses in convective downdrafts. We observe events that are clearly dominated by one or the other process, however, generally both of them act on the cold pool formation and can hardly be disentangled.

## 2.3 IMPLICATIONS

The analysis of long-term tower observations presented in Study A draws a clear and robust picture of the average cold pool properties over northern Germany. The mean annual cycle of detected cold pool passages shows that the summer period from June to August is the season with highest likelihood to capture cold pool events and, therefore, the ideal time to conduct FESSTVaL. The perturbations in analyzed measurement variables also suggest that air temperature, pressure, and wind speed are the most reliable parameters to identify cold pools and to be included into the instrument design for the field experiment.

Apart from the technical considerations, Study A allows us to better understand the mechanisms that control the variability in cold pool strength. Although the two identified main factors, evaporation of precipitation and import of upper-level air masses by downdrafts, are well-known processes, the considerably larger explanatory power of the pre-event saturation deficit for the cold pool strength compared to the rainfall amount is a new finding. This also contradicts the common assumption in literature that rainfall is the most important factor for the cold pool strength. Still, about one third of the observed variability in the temperature signal remains unexplained and cannot be explained without further knowledge about the individual cold pool events. By definition, single-point

observations miss information about the history and structure of the sampled cold pool, i. e., when it was initiated and where its center is located relative to the measurement location. Anecdotal evidence from observations and high-resolution simulations tells us that the strength of a cold pool largely varies throughout its life cycle and within its spatial extent. However, we still lack direct observations that help to put local measurements into context. Furthermore, Study A does not consider spatial information of precipitation that can be related to properties of a cold pool usually propagating away from its parent convective cell.

# 3 REALIZATION OF DENSE STATION NETWORKS

The lack of direct observational evidence of the horizontal dimension of cold pools motivated the idea for the ambitious FESSTVaL experiment, the central component of this dissertation. The measurements of a dense station network represent a substantial progress in quantifying the morphology of cold pools for the first time and help us to better interpret the signals and processes derived from single-point observations as in Chapter 2. In this chapter, I present the considerations that were required for the design and planning of the experiment, the challenges related to its realization, and the performance of the measurement instruments.

## 3.1 DESIGN OF INSTRUMENTS

### 3.1.1 *Requirements*

Observing the horizontal dimension of cold pools is challenging, which might be one reason why this task has not yet been satisfactorily addressed in the past. Indications from various observational platforms and high-resolution model simulation tell us that the size of cold pools typically ranges from a few to tens of kilometers but can even reach hundreds of kilometers (e. g., Zuidema et al., 2017). To capture not only the full extent of a cold pool but also its inner structure, the observations need to have a spatial resolution of one order of magnitude smaller, i. e., $\mathcal{O}(100)$ m – $\mathcal{O}(10)$ km, which we refer to as the sub-mesoscale. Based on the rough estimation for a 10-km$\times$10-km domain with 1-km resolution, we identified 100 as a reasonable number of measurement points for a ground-based network that allows to compromise between coverage and resolution. Here, we call such station network a dense network. Fortunately, the pyranometer network operated within the framework of the HD(CP)$^2$ Observational Prototype Experiment (HOPE) campaign (Madhavan et al., 2016) gave us confidence that a station network of this extent is actually realizable and manageable. Moreover, HOPE provided us with a role model for the design of instruments required for the network.

Measurement stations used in a dense network for observing cold pool signals not only have to be scalable to a number of 100, meaning to be financially inexpensive, but also need to fulfil several technical specifications. Most importantly, the instruments need to be equipped with meteorological sensors that precisely respond to rapid changes in signal strength as expected for cold pool front passages and sample at intervals $t \leq 10$ s. To limit both the constraints for measurement locations and the effort for station maintenance, the instruments have to operate independently of external power for about two weeks. Moreover, the instruments should be easy to install and to service. Since no ready-to-use solution fulfilling all of these requirements was available from commercial providers, we decided to produce the instruments by ourselves. The development of instruments, including design, assembling, and testing, took about three years and involved (part-time) work of one engineer, two student workers, and myself. The result is two types of measurements stations as introduced in Study B.

### 3.1.2 *APOLLO stations*

The backbone of our field experiment are the so-called Autonomous cold POoL LOgger (APOLLO) stations. Inspired by the pyranometer stations of the HOPE campaign (Madhavan et al., 2016), we designed the measurement stations based on simple masts that can be deployed virtually anywhere. Reflected by their working title *TP poles*, we decided to only include sensors for air temperature and pressure. This choice was made on the one hand to consider the findings of Study A and on the other hand to avoid the technical and financial effort needed for reliable sensors for, e. g., humidity. Furthermore, the exclusion of wind sensors owes to the additional restrictions on the choice of measurement locations that accurate wind observations would require.

The main component of an APOLLO station is a low-cost data logger optimized for low power consumption, which is based on a micro controller board located inside a logger box (Figure 3.1a). The temperature and pressure measurements are performed by a small (7 mm × 1.2 mm) and fast-response negative temperature coefficient (NTC) thermometer placed inside a passively-ventilated radiation shield at the top of the mast and a digital sensor inside the logger box, respectively. Both variables are sampled at 1-s resolution and logged to a micro-SD memory card. For initial time synchronization and drift correction of the internal clock in post-processing, an on-board GPS module is briefly activated once per hour, which minimizes the required power consumption. The logger can also establish a local WiFi hotspot for on-site control, data inspection, and fast access to measurement data via download. The power source of the data logger is a standard 20 Ah USB power bank battery that allows for an autonomous operation time of 10 to 14 d and is placed inside a separate plastic tube. All components are mounted on a 3-m mast that is anchored in the soil with a ground screw. The material costs for all required parts sum up to around EUR 300 per station.

The APOLLO stations prove their suitability to adequately capture signals of cold pool passages in several tests measurements. Experiments in a wind tunnel laboratory show that the time required for the shielded NTC temperature sensor to respond to rapid temperature changes (i. e., *e*-folding time constant) strongly decreases for increasing ventilation and is smaller than 14 s ± 10 % for a wind speed of $\geq 3\,\mathrm{m\,s^{-1}}$. This property compensates for the lack of active ventilation that is common to more precise (in absolute terms) but slower-responding temperature measurements. As a result, the APOLLO captures the amplitude and shape of the rapid cooling signature during a cold pool event without apparent lag compared to an inertia-free ultrasonic sensor. Furthermore, the relative accuracy of the air pressure sensor proves to be sufficient to identify changes in barometric pressure equivalent to differences in altitude of less than 1 m.

### 3.1.3 *WXT weather stations*

The Weather Transmitter (WXT) stations are the bigger sisters of the APOLLO stations (Figure 3.1b). They are designed to form a secondary, less-dense network and provide information about parameters not measured by the APOLLO network. The name of the WXT weather stations refers to their main component, the Vaisala Weather Transmitter WXT536. The WXT536 is a commercial compact multi-parameter sensor that is usually used for climate monitoring and combines a multi-parameter sensor for temperature, pressure, and humidity, an ultrasonic anemometer for measurements of horizontal wind speed and wind direction, and a piezoelectrical module sensing impacts of rain drops and hail stones. To compensate for the rather slow-responding internal thermometer, the

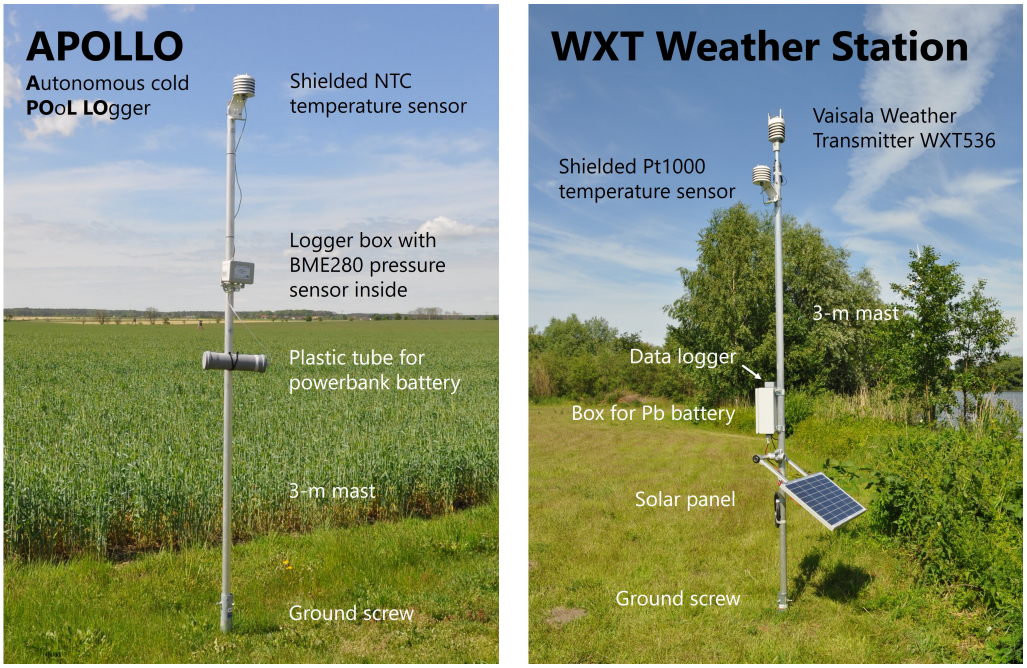


(a) (b)

Figure 3.1: Components of (a) APOLLO station and (b) WXT weather station.

WXT station is equipped with an external Pt1000 thermometer inside a separate radiation shield that exhibits response times smaller than 55 s±10 % for a wind speed of $\geq 3\,\mathrm{m\,s^{-1}}$. All measurement data are sampled at 10-s resolution and written onto an SD memory card by a data logger that is synchronized with an integrated GPS module. Each station is powered by a 12-V lead battery that is recharged by a solar panel, which allows for autonomous operation over an extended summer period. Similar to the APOLLO stations, the components of the WXT station are attached to a 3-m mast that is anchored in the soil with a ground screw. Since the wind observations are very sensitive to disturbances of the local flow field by surrounding obstacles like buildings or vegetation, the WXT measurement sites are carefully chosen to minimize this impact.

## 3.2 IMPLEMENTATION OF FIELD EXPERIMENTS

The initial plan for the FESSTVaL experiment was to set up a network of about 100 APOLLO and WXT weather stations in the surrounding of the Meteorological Observatory Lindenberg – Richard Aßmann Observatory (MOL-RAO) located in eastern Germany about 60 km south-east of Berlin. The MOL-RAO is operated by the German Weather Service and was chosen given the variety of already existing operational measurement systems and the combination of relatively flat terrain and frequent convective activity during the summer. To sample a reasonable number of cold pool events, the experiment was planned to cover an extended summer period from May to August 2020.

In early 2020, the assembling of measurement stations and preparations for FESSTVaL were in full swing. However, soon the plans turned out to be not realizable. In March 2020 the impacts of the COVID-19 pandemic also seriously affected Germany and made any travels for the experiment impossible. Without knowing when and if at all we could

resume the original plan, a fundamental modification of the experiment was required. Not least to generate a data set usable for this dissertation, we decided in April 2020 to postpone FESSTVaL by one year and to replicate a home office-conform version of the experiment in Hamburg in summer 2020, named Field Experiment on Sub-mesoscale Spatio Temporal variability at Hanseatic city of Hamburg (FESST@HH).

### 3.2.1 *FESST@HH 2020*

Study B describes the implementation of FESST@HH. The modification of plans left us with the task to acquire about 100 measurement locations over the greater area of Hamburg less than two months before the intended start of the experiment. As the most feasible and least bureaucratic approach we identified to ask existing institutional partners as well as colleagues and friends of the Meteorological Institute of the University of Hamburg and the local Max Planck Institute for Meteorology to host measurement stations on their premises and in their private backyards. Thanks to the short-notice support of the numerous partners, we were actually able to set up 82 APOLLO and 21 WXT weather stations over an area of about 50 km × 35 km (Figure 3.2). The installation of instruments started in late May 2020 and took about three weeks, while the official measurement period of FESST@HH ran from 1 June to 31 August. The resulting network covered the urban center of Hamburg and parts of its rural surrounding, whereas the approach of site acquisition caused a random distribution of stations over the area with the tendency of higher density near the city center. Despite that, the sites for WXT stations were not only chosen to allow for weakly disturbed wind measurements but also to cover the network approximately uniformly. The average nearest-neighbor distance for all 103 measurement stations of 1.85 km with a standard deviation of 1.42 km shows that the rapidly implemented FESST@HH network still satisfies the requirements to study cold pools on the sub-mesoscale.

Besides the quick and simple acquisition of measurement locations, another benefit of the community approach of the experiment was that it significantly reduced the individual work load associated with the maintenance of the instruments. Station hosts could volunteer to take over maintenance duties, which included to regularly change the battery, check the measurement data, and upload them to an FTP server. The remaining stations were serviced by colleagues and student workers living nearby. Instead of a small team servicing the entire network, the maintenance work was shared between nearly 40 people. Since many of them were laypersons for meteorological instruments, the project unintentionally included a citizen science component. Although its impact was not evaluated, it is still a unique and valuable feature of the experiment.

### 3.2.2 *FESSTVaL 2021*

Although delayed by one year, we were able to successfully conduct the FESSTVaL experiment at the MOL-RAO in the desired format in summer 2021. The experience of the previous year allowed us to optimize the process of instrument installation, which reduced the time needed to set up a network of similar size by roughly half. The design of the FESSTVaL station network was developed based on an idealized triangular grid that forms concentric rings and radially decreases in density. The purpose of this design was to compromise between sub-km-scale resolution and sufficient spatial coverage as well as to use triangles of measurement points to estimate the propagation velocity of cold pool fronts. Instead of asking individual landowners for permission to install the stations at the desired locations,

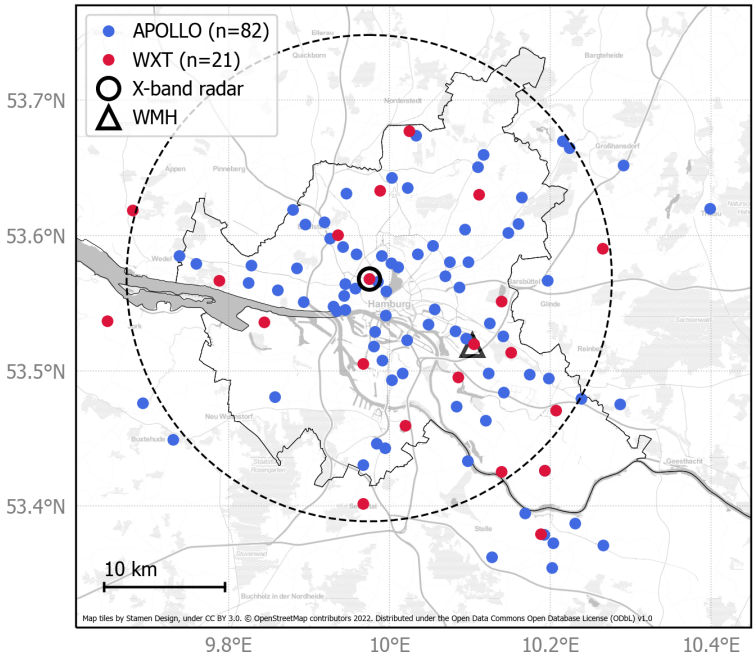


Figure 3.2: Map of measurement locations of APOLLO and WXT weather stations during the FESST@HH 2020 experiment. Indicated are also the location and the 20-km scanning range (dashed line) of the X-band rain radar and the Weather Mast Hamburg (WMH). Black solid line marks the city limits of Hamburg.

the concept for site acquisition was to approach only a small number of local authorities for permission to set up the stations on the about 5-m wide strip of public ground along major roads. The final positions of measurement sites were then determined according to these boundary conditions by shifting the locations of the idealized network to the closest public road. As described in Study C, the FESSTVaL network consisted of 80 APOLLO and 19 WXT stations covering a circular area of about 30 km in diameter, with its center at the Falkenberg boundary layer measurement site situated about 5 km south of the MOL-RAO (Figure 3.3a). The experiment area is located in a sparsely populated environment that is characterized by forests, scattered lakes, and mostly flat terrain. Although being slightly smaller and more structured, the network exhibits a spatial resolution similar to the FESST@HH network according to an average nearest neighbor distance of 1.98 km and a standard deviation of 1.26 km.

The measurement period of FESSTVaL ran from 17 May to 27 August 2021. Thanks to a sophisticated maintenance plan including optimized routes for five pre-defined sectors of the network, all 99 measurement stations could be serviced by a single person within five working days. However, one major drawback of the strategy to set up the measurement stations along public roads was the vulnerability of instruments to undesired interventions by unknown persons. The number of incidents like theft of batteries and manipulation or destruction of stations actually increased from one to 27 compared to FESST@HH, whereas the majority of incidents occurred as an apparently coordinated attack during the last days of the measurement period[1].

1 Comment: This demonstrates that the installation of 99 suspiciously looking masts at prominent locations is actually a brave idea...

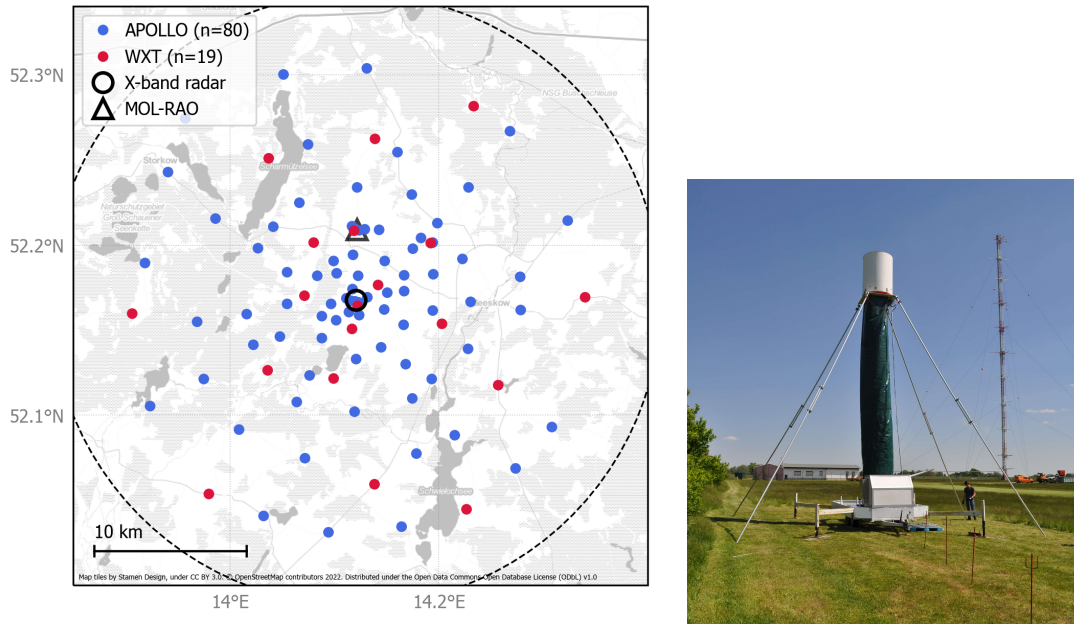


(a) (b)

Figure 3.3: (a) Map of measurement locations of APOLLO and WXT weather stations during the FESSTVaL 2021 experiment. Indicated are also the location and the 20-km scanning range (dashed line) of the X-band rain radar and the MOL-RAO. (b) X-band rain radar installed on the platform of a trailer at the Falkenberg measurement site.

### 3.2.3 *Data sets*

After completion of the observation periods, the generated raw measurement data were further processed and prepared for publication. This task mainly included the GPS correction of the logged time stamps, the removal of erroneous data caused by technical flaws or external impacts, and the homogenization into a standardized NetCDF data format. The finalized data set of FESST@HH (Kirsch et al., 2021) exhibits an overall availability of quality controlled APOLLO and WXT data of 90.0 % and 94.3 %, respectively, if only the period after the completion of the installation phase in mid-June is considered (Figure 3.4a). For the FESSTVaL data set (Kirsch et al., 2022), these numbers are even slightly higher (92.0 % and 98.1 %), whereas the considerably decreased availability of APOLLO data during the first days of the observation period marks the successive activation of stations after their installation two weeks before (Figure 3.4b). The FESST@HH and FESSTVaL data sets also include meta data describing the local thermal climate of the measurement sites based on standardized local climate zone (LCZ) classes introduced by Stewart and Oke (2012). This information is of interest especially for the FESST@HH observations, since the re-design of the experiment meant to move the network to an area consisting of a mixture of urban and rural environments compared to the mostly rural setting of the MOL-RAO. Therefore, the strengths of the data set are not limited to the analysis of cold pools but also allow to study urban effects like the nocturnal urban heat island of Hamburg or variations of turbulent temperature fluctuations in different urban and natural environments, which are well captured by the fast-response NTC thermometers of the APOLLO stations.

During FESSTVaL 2021, the dense network of APOLLO and WXT stations was accompanied by a myriad of in situ and remote sensing observations performed operationally by the

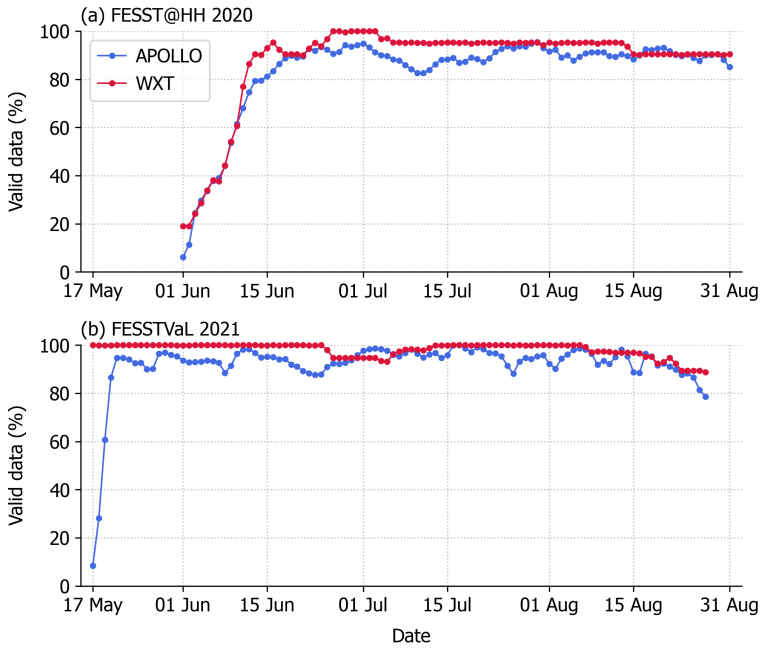


Figure 3.4: Daily mean availability of quality controlled APOLLO and WXT station measurement data for (a) FESST@HH (1 June to 31 August 2020) and (b) FESSTVaL (17 May to 27 August 2021).

German Weather Service at the MOL-RAO or other research groups in the framework of the experiment. These include a 99-m high boundary layer tower at the Falkenberg site, several Doppler wind lidars, swarms of uncrewed aerial vehicles, and energy balance measurements at three dedicated supersites. Particularly relevant for the investigation of cold pool formation and further analyses in this dissertation is the data set of an X-band rain radar (Burgemeister et al., 2022b) at the center of the station network, which was temporarily installed for the experiment period and operated by the University of Hamburg (Figure 3.3b). According to an established measurement principle, the radar horizontally scans the atmosphere with electromagnetic radiation (frequency $f = 9.4\,\mathrm{MHz}$; X-band region of the electromagnetic spectrum) and the backscatter signal allows to derive spatial information on rainfall intensity at resolutions of 60 m in range, 1° in azimuth, and 30 s in time and a maximum range of 20 km. Similar measurements are also available for FESST@HH, since an identical radar instrument is permanently installed on the rooftop of the 85-m high *Geomatikum* building in the city center of Hamburg. However, the radar scan radius does not cover the entire station network (Figure 3.2) and the data are only available for the last month of the observation period due to downtimes of the instrument (Burgemeister et al., 2022a).

## 3.3 LESSONS LEARNED

The successful realization of the FESST@HH and FESSTVaL experiments represents a substantial scientific contribution and teaches several helpful lessons for future observational campaigns. First of all, this project demonstrates that the construction and operation of a sub-mesoscale station network dedicated to the observations of cold pools is actually practicable although never done before. The strategy to design and manufacture about

100 custom-built, low-cost instruments proves feasible according to the reliable operation of APOLLO and WXT stations and indicated by the remarkably high availability of quality controlled measurement data. The greatest challenges regarding the execution of the field experiment are the acquisition of suitable measurement sites and the choice of the maintenance strategy. Owing to the boundary conditions set by the COVID-19 pandemic, FESST@HH and FESSTVaL represent two different approaches to these challenges without one being clearly superior to the other. While the custom-designed FESSTVaL network ensures homogeneous site conditions and keeps the acquisition effort small, the installation of instruments on secured premises during FESST@HH reduces the risk of manipulation and damage by external persons. The highly coordinated maintenance strategy involving few but well-instructed persons probably accounts for the slightly improved overall data availability during FESSTVaL. However, FESST@HH demonstrates that a community effort supported by laypersons, although being implemented on short notice, has the potential to substantially ease the operation of a dense station network.

# 4 COLD POOLS IN DENSE STATION NETWORKS

To the same degree as the realization of FESST@HH and FESSTVaL were ambitious and challenging considering the extraordinary circumstances, the generated data sets are unique. For the first time, the data allow a glimpse into previously obscured properties of cold pools based on in situ observations. Without claiming to exploit the data sets already to their full potential, this chapter showcases a possible approach to analyze the measurements of the dense station networks for illuminating the spatial dimension of cold pools.

## 4.1 SPATIO-TEMPORAL ANALYSIS

The evaluation of the FESST@HH and FESSTVaL data sets involves a considerably higher degree of complexity compared to single-point observations. More specifically, the detection and analysis of cold pools need to be expanded from one dimension (time) to three dimensions (time and horizontal space), which opens up numerous possibilities of how to approach this task. We decided to first compile a list of cold pool events sampled by the station networks and subsequently apply a spatial interpolation method to identify individual cold pool objects.

### 4.1.1 *Identification of events*

When atmospheric convection affects an area of the size as the considered experiment domain, i. e., several tens of km in diameter, it typically lasts for a few hours and may produce one or more cold pools. We refer to such events as cold pool events. Given the high spatial density of the network, the cold pools are expected to be recorded by multiple stations albeit not simultaneously but over the course of several minutes or even hours. To identify all cold pool events observed over the 3-month experiment period, we apply the detection algorithm introduced in Study A on the individual single-point observations. We define potential cold pool events as periods when five or more stations detect temperature drops. However, to include cold pool passages without local rainfall, we omit the rainfall criterion used in Study A and verify the plausibility of potential events based on the visual inspection of operational precipitation radar imagery. All events are analyzed over a maximum event duration of 4 h.

As presented in Study B and C, the method identifies a total number of 37 and 42 cold pool events sampled during FESST@HH and FESSTVaL, respectively. Here, the number of about 12 events per month is considerably larger than the corresponding average frequency for June to August (around 7 per month) observed at the WMH site (Figure 2.1b; Study A). This indicates that single-point observations frequently miss cold pools in close proximity. Moreover, the variability of observed temperature perturbations within the network for single events is even larger than the variability in average signal strength between the different events. However, we still need to determine the number and structure of involved cold pools.

### 4.1.2 *Identification of cold pool objects*

Study C describes our approach to identify individual cold pool objects in the analyzed events. We define a cold pool object as a spatially connected area of temperature perturbation $\Delta T$ in the horizontal field reconstructed from the station signals. First, this requires the definition of a robust reference state in space and time that estimates a hypothetical, unperturbed temperature field, i. e., without the presence of a cold pool. Here, we simply use the same linear temperature trend $T_{\mathrm{ref}}(t)$ as a time-dependent reference temperature for all stations. $T_{\mathrm{ref}}(t)$ is given by the (unperturbed) average temperature trend over all stations during the first 60 min of the event, which is extrapolated over the entire event period. Then, we calculate $\Delta T$ at every station from the difference between the current temperature and $T_{\mathrm{ref}}$, and spatially interpolate $\Delta T$ to a regular 1-km×1-km grid using the ordinary kriging method (Murphy et al., 2021; Wackernagel, 2003). Cold pool objects are defined as four-connected clusters of grid points with $\Delta T \leq -2\,\mathrm{K}$ larger than 10 $\mathrm{km}^2$, whereas multiple cold pool objects per time step are allowed.

Figure 4.1 showcases the spatial interpolation of $\Delta T$ for cold pool events *Elphi*, recorded during FESST@HH on 10 August 2020, and *Jogi*, recorded during FESSTVaL on 29 June 2021, which are two of a few selected cases that were named. The good overall match in spatial structure between the temperature perturbation and rainfall intensity field does not only provide confidence in the reliability of the two independent observation systems but also confirms our perception of cold pools initially forming in the area of strongest precipitation and propagating horizontally away from their origin. Not least, this is actually the first ever spatial view of cold pools based on in situ observations.

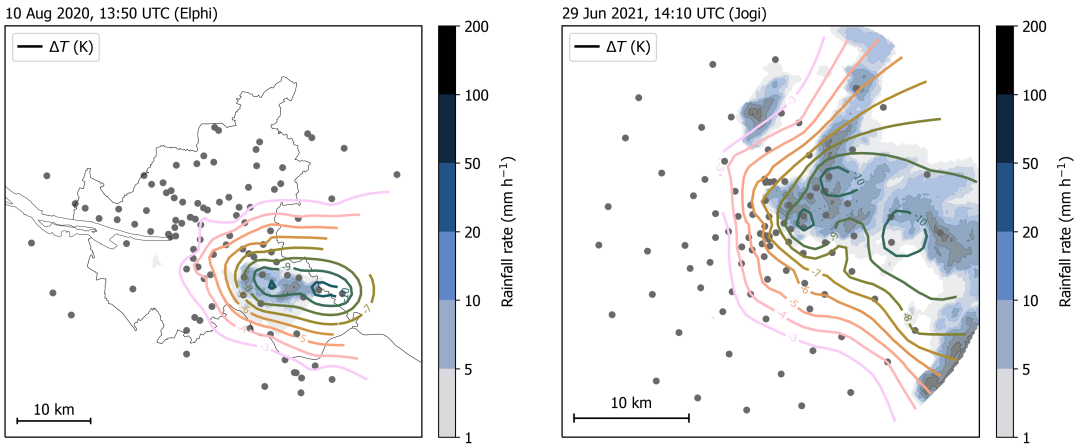


(a) (b)

Figure 4.1: Snapshots of interpolated temperature perturbation $\Delta T$ (colored isolines) observed by the dense station networks (gray dots) and radar-measured rainfall rate (blue shading): (a) cold pool *Elphi* on 10 August 2020 at 13:50 UTC during FESST@HH and (b) cold pool *Jogi* on 29 June 2021 at 14:10 UTC during FESSTVaL (color maps by Crameri, 2018).

## 4.2 MORPHOLOGY OF COLD POOLS

The introduced analysis method finally allows us to explore the novel data sets and derive previously unobserved properties of cold pools (Study C). For now, we focus on the size

and shape of cold pools as well as the mean temperature perturbation over their extent. More specifically, we robustly quantify the diameter of all sampled cold pool objects that cover a wide range of event types and test whether the common assumption that cold pools are round (i. e., circularly shaped) is justified. Here, we restrict the analysis to the FESSTVaL data set.

### 4.2.1 *Size*

When the analysis method is applied to all 42 cold pool events of FESSTVaL at 1-min intervals, we obtain a total number of 4955 cold pool objects during 39 events that exhibit the minimum required size of 10 $km^2$. The median equivalent diameter $d_{equi}$ (i. e., the diameter of a circle with same area) of the objects is 17.4 km. However, the significance of this number is strongly affected by the fact that many cold pool objects are only partially sampled and reach beyond the boundaries of the experiment domain as illustrated in Figure 4.1. We decided to address this issue by neglecting objects that do not allow a reliable estimation of their morphological properties instead of making assumptions on their extent outside of the station network. For an objective separation, we define the boundary contact parameter $f_b$ that indicates the fraction of cold pool perimeter that touches the boundary of the measurement network. As a trade-off between sample size and integrity of the results, we keep all objects with $f_b \leq 0.25$. The applied filtering reduces the sample size by about 75 % and leaves us with 1278 cold pool objects. The remaining sample exhibits a median $d_{equi}$ of 8.4 km with values varying between the detection threshold of 3.6 km (equivalent to 10 $km^2$) and above 20 km (Figure 4.2a). The corresponding median object-mean temperature perturbation $\overline{\Delta T}$ is -2.3 K (Figure 4.2b). When further splitting the sample into a weaker and a stronger half based on $\overline{\Delta T}$, we find that the size of cold pools correlates with their strength, meaning that strong cold pools are larger than weak ones. Also the reverse statement, that large cold pools are stronger than small ones, is true.

These results match well with our intuitive notion of the morphology of cold pools, and the numbers are within the range of cold pool sizes derived from observations (Feng et al., 2015; Terai and Wood, 2013) and numerical simulations (Tompkins, 2001). However, the finite extent of the station network and the rigorous filtering of the objects limit a general assessment of the cold pool size, whereas the absolute numbers strongly depend on the chosen threshold for $f_b$ and tend to be biased to small sizes. Moreover, the sample is not statistically independent as it includes identical objects of the same event but at a different stage of their life cycle.

### 4.2.2 *Shape*

The data set also allows us to challenge the common conceptual model that cold pools are circularly shaped objects (e. g., Haerter et al., 2019; Meyer and Haerter, 2020; Romps and Jeevanjee, 2016). We test this assumption by determining the aspect ratio of the sampled cold pool objects given by the fraction between the length of major axis and minor axis of an ellipse fitted to the individual objects. Therefore, the aspect ratio is is 1 for circularly shaped and greater than 1 for elongated objects. For the filtered cold pools sample, the values vary between about 1.1 and 2.6 and exhibit a median of 1.55, indicating that the objects are generally not circularly shaped (Figure 4.2c). The data for the four sub-samples of small, large, weak, and strong cold pools show that this is true independent of size and

strength and also of the choice of the filtering threshold for $f_b$ (not shown). These findings suggest that the concept of perfectly round cold pools generally does not match with reality although we do not further specify their actual shape. A possible explanation is the merging of initially isolated cold pools into larger, irregularly shaped clusters (Torri and Kuang, 2019), which that are not identified as individual objects by the analysis method. Indications from single events also suggests that the objects tend to be stretched along the propagation path of the parent convective cell with the background flow.

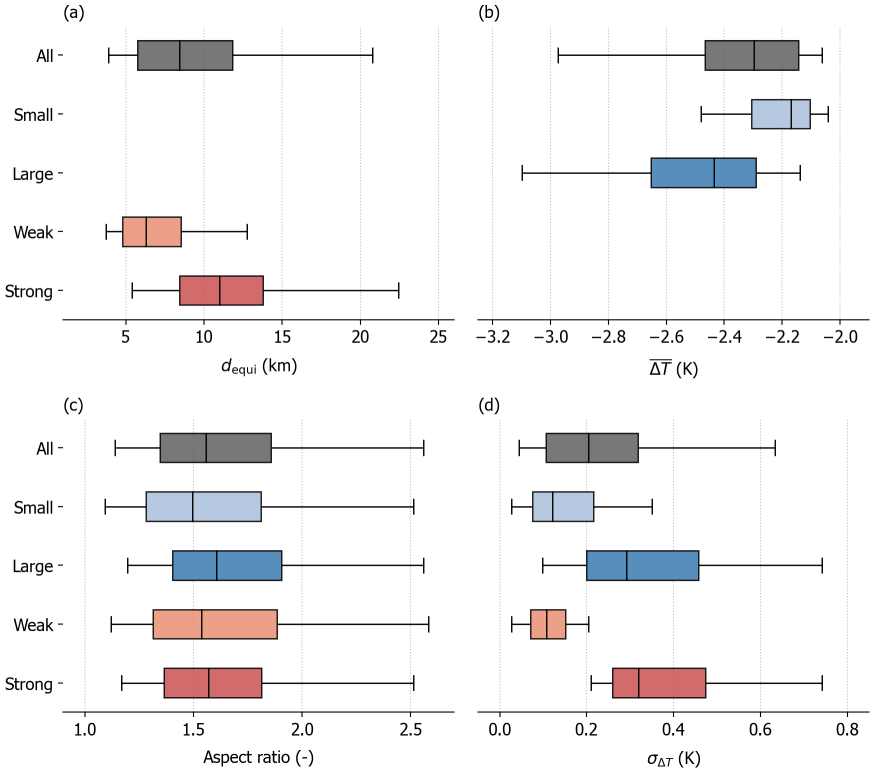


Figure 4.2: Distribution of (a) equivalent diameter $d_{equi}$, (b) object-mean temperature perturbation $\overline{\Delta T}$, (c) aspect ratio, and (d) standard deviation of $\Delta T$ of cold pool objects with a maximum network boundary contact of 25 %. Shown are the respective data for all 1278 objects (gray), for objects smaller (light blue) and larger (dark blue) than the median of $d_{equi}$, and objects weaker (light red) and stronger (dark red) than the median of object-mean $\overline{\Delta T}$. Distributions of sub-samples defined by the respective variables on the $x$-axis are not shown. The aspect ratio represents the ratio between major axis and minor axis of an ellipse fitted to the cold pool object. Vertical lines, boxes, and whiskers mark the median value, 25th/75th percentiles, and 5th/95th percentiles, respectively.

## 4.3 GROWTH MECHANISMS

The observations of FESSTVaL are not only suited to determine properties of static cold pool objects but also to track their life cycle over a certain period. The previous results show that the limited spatial extent qualifies the station network to describe especially small cold pools, which tend to be young, i. e., in an early stage in their growth phase. To capture these cold pools and understand the associated growth processes, we manually select suitable events that are initiated and grow inside the experiment area rather than

move into it with the parent cell. Four cold pool events fulfil these criteria, namely *Elphi* (10 August 2020), *Felix* (26 June 2021), *Jogi* (29 June 2021), and *Jürg* (25 July 2021), whereas *Elphi* was sampled during FESST@HH. Study C analyzes the growth phases of the four cold pools up to the times when they reach their maximum sizes or become too large for the network (here defined by $f_b \geq 2/3$). All four cold pools grow at a nearly constant rate for between 55 and 75 min and reach sizes of at least 1000 km$^2$, while *Felix* reaches only about 100 km$^2$ and is the only event whose entire life cycle is observed by the network. Also the development of $\overline{\Delta T}$ varies among the four events and reach maximum values between about -3 K and -7 K before the end of the analyzed growth phase.

The analysis of single-point observations in Study A shows that the local cooling signal of cold pools can be traced back to the footprint of evaporation of precipitation, although the correlation with the local rainfall amount is weak. The high-resolution measurements of the X-band rain radar (Burgemeister et al., 2022a,b) help to relate the impact of rainfall also to cold pools as entities. Figure 4.3a illustrates the relationship between the radar domain-integrated accumulated rainfall amount $\Sigma R_{\text{Radar}}$ and cold pool area $A_{\text{CP}}$ over the growth phase of the four selected events, whereas both quantities are normalized between 0 and 1 to facilitate comparison. For all four cases, $A_{\text{CP}}$ scales almost perfectly linearly with $\Sigma R_{\text{Radar}}$ according to correlation coefficients larger than 0.98, although the absolute rainfall amounts differ by more than one order of magnitude. This shows that the production of cold air, both directly by evaporative cooling and indirectly by import of potentially cooler air in convective downdrafts, is the main driver for the volume increase of cold pools. In addition, the relative scaling between $\Sigma R_{\text{Radar}}$ and $\overline{\Delta T}$ is very similar for the four events, showing a non-linear relationship with strongest cooling by the first half of the rainfall amount and a very weak impact on the temperature for the second half (Figure 4.3b). Therefore, evaporation of precipitation is the dominant cooling process as it is most efficient in the early stages of the cold pool life cycle when the boundary layer air is still most under-saturated. This is in line with the high explanatory power of the saturation deficit for the local cooling signal found in Study A.

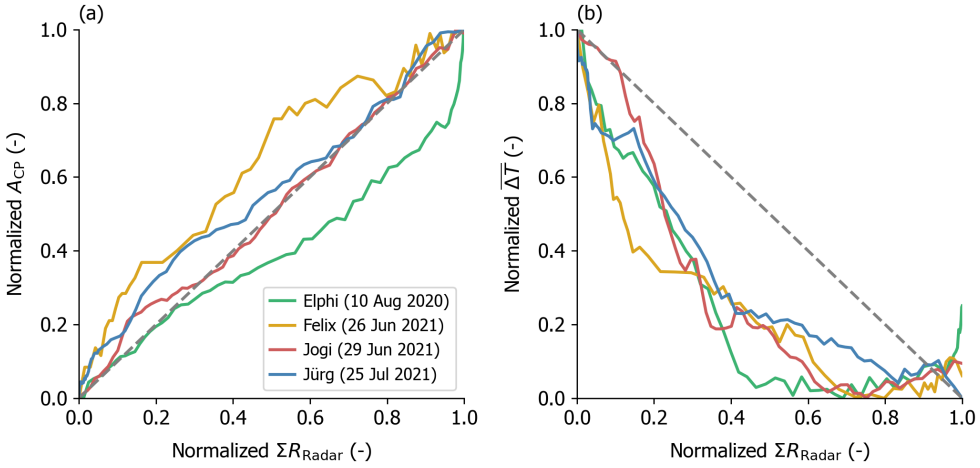


Figure 4.3: (a) Cold pool area $A_{\text{CP}}$ and (b) object-mean temperature perturbation $\overline{\Delta T}$ dependent on area-integrated accumulated rainfall amount $\Sigma R_{\text{Radar}}$ during the growth phase of cold pool events *Elphi*, *Felix*, *Jogi*, and *Jürg*. The minimum–maximum range of all quantities is normalized between 0 and 1. Gray dashed lines are the 1-to-1 lines whereas for (b) it is adapted to the negative values of $\Delta T$. Time runs from left to right in both (a) and (b).

The good agreement between the derived cold pool properties and the radar-observed rainfall amount is surprising, since the analysis does not include the vertical dimension. In reality, a cold pool is a three-dimensional body whose volume is controlled by the amount of produced cold air and, therefore, should be proportional to the total amount of involved precipitation. The linear scaling between cold pool *area* and rainfall amount means that the cold pool height stays approximately constant during the growth phase. The physical process behind the expansion of a cold pool is often described in literature as a density current that horizontally propagates due to its decreased buoyancy. Apart from the density difference between the density current and its environment, the propagation velocity is directly proportional to the height of the current (Benjamin, 1968; von Kármán, 1940). In Study C, we argue that a horizontally expanding cold pool would rapidly flatten and decelerate without constant volume increase by supply of cold air. Therefore, the approximate conservation of the cold pool height, which is also supported by radiosonde observations during FESSTVaL, indicates an approximate balance between the theoretical flattening under volume conservation and the volume increase by cold air import through rainfall evaporation and convective downdrafts. In conclusion, both mechanisms, the cold air production and the subsequent density current-like expansion, act hand in hand and are crucial to sustain the growth of a cold pool.

## 4.4 COLD POOL STRUCTURE

As its most intriguing capability, the FESSTVaL station network allows us to catch a glimpse into the horizontal temperature structure of cold pools, which helps to more thoroughly understand the previous findings of this dissertation. The evaluation of cold pool objects presented in Section 4.2 already statistically quantifies the variability of $\Delta T$ within the objects and finds a median standard deviation $\sigma_{\Delta T}$ of about 0.2 K (Figure 4.2d). Without interpreting this number in absolute terms, the analysis also shows that $\sigma_{\Delta T}$ is significantly larger for large and strong cold pool objects. Although rather anecdotally, detailed analyses of selected events give us more information about the shape of the spatial distribution of $\Delta T$. Representative for other cases, Figure 4.4 illustrates the spatio-temporal evolution of $\Delta T$ during cold pool *Jogi* relative to its analyzed center defined by the $\Delta T$-weighted centroid of the object. During the first 60 min of its life time, *Jogi* constantly grows and cools and still continues to grow after reaching its maximum strength near the center. The temperature perturbation maintains a concentric structure with a roughly constant radial gradient throughout the growth phase and only starts to homogenize after the time of peak intensity. Consistent with the findings presented in Section 4.3, the expansion of the cold pool area and the time of its end correlate well with the increase and decay of the average rainfall intensity over the experiment area. Also the cold pool area of individual events should be directly related to its maximum $\Delta T$ when considering a concentric temperature structure with strongest signal at the center and given the fact that larger and stronger cold pools are generally more heterogeneous. Under these circumstances, the rainfall amount does not only control the cold pool area but also the maximum strength at the center and the temperature perturbation anywhere else within the cold pool. However, in the context of single-point observations as in study A, the relationship between rainfall and local temperature perturbation is not dominant as these observations do not include information about the age of the cold pool and their distance to the cold pool center. Moreover, the local rainfall amount is not representative for the intensity of the parent convective cell generating the cold pool.

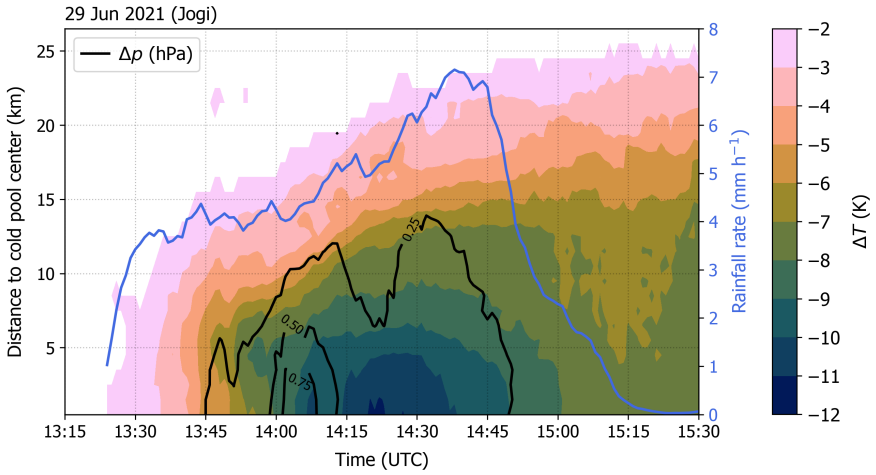


Figure 4.4: Time series of temperature perturbation $\Delta T$ (color-coded) and pressure perturbation $\Delta p$ (black isolines) dependent on distance to cold pool center for cold pool event *Jogi* on 29 June 2021 (color map by Crameri, 2018). $\Delta T$ and $\Delta p$ indicate averages of all spatially interpolated observations at grid points inside the analyzed cold pool object with same distance to its center, defined as the $\Delta T$-weighted centroid. $\Delta p$ at individual measurement stations is defined as the deviation from the linear pressure trend over the 4-h event period. Blue solid line indicates the domain-mean rainfall rate observed by the X-band rain radar.

The illustration of the structure of cold pool *Jogi* in Figure 4.4 also includes direct evidence for the presence of convective downdrafts that we attribute to the local strength of $\Delta T$ (Study A) and to the cold pool growth by cold air import (Study C). The spatio-temporal signal of the observed air pressure perturbation $\Delta p$ shows a distinct peak at the cold pool center about 15 min before $\Delta T$ reaches its maximum. The time lag indicates that this signal in $\Delta p$ is not hydrostatically generated by cooling of the atmospheric column but of non-hydrostatic nature. Non-hydrostatic pressure perturbations are long known (e. g., Markowski and Richardson, 2010; Mueller and Carbone, 1987; Wakimoto, 1982) and can be related to dynamical effects due to the collision of convective downdrafts with the surface. As already suggested in Study B, these short-term pressure signals underline that our thermal perspective on cold pools needs to be complemented by a dynamical one, which helps to gain a comprehensive understanding of cold pool characteristics.

We emphasize that the interpretation in this subsection is preliminary and has to be confirmed by further in-depth analyses. However, the available findings draw a plausible and consistent picture and give a first substantial indication for the actual temperature structure of cold pools, which is inconsistently represented in numerical simulation studies (Drager et al., 2020; Meyer and Haerter, 2020). The cold pool structure even proves to be a key element to unify the results presented throughout this dissertation. In this sense, the overarching benefit of the dense station networks of FESST@HH and FESSTVaL is to provide context to the variability of cold pool characteristics derived from single-point observations and to deepen our understanding of the controlling mechanisms.

# 5 CONCLUSIONS

## 5.1 BENEFIT AND PRACTICALITY OF DENSE STATIONS NETWORKS

In this dissertation, I describe the realization of dense networks of custom-designed, low-cost meteorological measurement stations to shed light on the spatial dimension of convective cold pools for the first time with in situ observations. The work brings together the results of three studies that define the overall story line: firstly, the analysis of long-term tower observations providing a robust characterization of cold pools in traditional point measurements; secondly, the development of novel APOLLO and WXT measurement stations and the realization of the FESST@HH and FESSTVaL experiments; and lastly, the evaluation of the unique data sets and the interpretation of the derived cold pool properties and underlying processes. The starting point of the dissertation was the observational blind spot at the sub-mesoscale, i. e., spatial scales between $\mathcal{O}(100)$ m and $\mathcal{O}(10)$ km, left by conventional measurement setups. This motivated the hypothesis that high-resolution observations help us to sharpen and challenge our perception of cold pools that is mainly shaped by numerical simulations and single-point observations. In summary of the findings discussed in the three studies, the overall result of the dissertation is:

*Yes, a dense observational station network at sub-mesoscale resolution is suitable to enhance our understanding of cold pools.*

In more detail, the answers to the research questions posed in Chapter 1 are the following:

- *What new information on cold pool characteristics does a dense station network provide compared to single-point observations?*

  Observations at the 280-m high WMH robustly characterize the local properties of 489 cold pool passages during 14 extended summer seasons, representing the classical single-point perspective. The sampled cold pools preferably occur in July and the mid-afternoon hours. The temperature perturbation $\Delta T$ near the surface ranges between the detection threshold of -2 K and an extreme value of -10.8 K, exhibits a median of -3.3 K, and generally weakens with height. The vertical measurement component also proves the existence of a lifting-induced overturning circulation at the leading edge of cold pools and allows to derive a median cold pool height of 746 m based on the vertical extrapolation of the pressure signal. The 3-month FESST@HH and FESSTVaL experiments open a new perspective on cold pools using a dense network of about 100 measurement stations that allow us to also quantify the size, shape, and spatial structure of the surface footprint of cold pools. The statistical evaluation of 1278 sampled cold pool objects during 39 events reveals a median equivalent diameter of 8.4 km and maximum sizes up to three times larger, although the absolute numbers are negatively biased by the extent of the station network. Large cold pools tend to be strong and vice versa. The aspect ratio of the objects ranges from 1.5 to 1.6 independent of their size and strength, meaning that cold pools are generally not circularly shaped, contrarily to common assumption. The spatial variability of the temperature within the objects increases for larger and stronger cold pools and a detailed view on single events suggests a concentric

structure with strongest perturbations near the center, which provides guidance for the verification of existing numerical simulation studies. These findings could not have been achieved with previously available observational data sets and enhance our ability to correctly describe cold pools. A comprehensive understanding also requires the reliable characterization of the vertical structure of cold pools. Although WMH observations and singular radiosonde profiles during FESSTVaL provide estimates of the cold pool height, its spatial variability, which is critical to interpret the density-driven expansion of cold pools, is still poorly observed.

- *Which factors control the strength and size of cold pools?*

  The long-term WMH observations show that the strength of $\Delta T$ during cold pool passages exhibits a higher correlation with the evaporation potential of the air mass prior to the event ($r = -0.71$) than with the event-accumulated rainfall amount ($r = -0.35$). Cooling by rainfall evaporation explains even 64 % of the variability of $\Delta T$ if the observed moistening of the air is considered. The process becomes occasionally superposed by the downward transport of potentially cooler upper-level air into the sub-cloud layer through precipitation-driven downdrafts as indicated by perturbations in equivalent potential temperature. However, the dense network observations reveal the spatially integrated rainfall amount to be the dominant controlling factor for cold pool growth, according to an almost perfectly linear relationship with the area expansion of four selected events. Consistently for these cases, the rainfall cools most efficiently in the early growth phase, which also points to the impact of evaporative cooling. Therefore, precipitation acts on the volume increase and cooling of cold pools, both by cold air production through evaporation and by import of upper air masses in convective downdrafts. This process runs in parallel to the density current-like expansion of a cold pool, which would theoretically lead to its flattening and deceleration, but this is not observed. Considering the roughly concentric structure of cold pools with coolest temperature at the center as found for single cases, the rainfall amount does not only control the cold pool expansion but also the strength of the local temperature signal. However, the WMH single-point observations are not able to verify this relationship as they do not include information of the age of the cold pool and the position relative to its center.

- *What challenges are related to the operation of a dense station network and evaluation of its observations?*

  Given the lack of comparable precedent experiments, FESST@HH and FESSTVaL prove that the realization of a measurement network at sub-mesoscale resolution for spatial cold pool observations is possible. The exceptionally good performance of the novel APOLLO and WXT stations demonstrate that the design and operation of about 100 custom-built instruments is a feasible measurement strategy. Apart from the technical requirements, the greatest challenges are the acquisition of suitable and secure measurement sites that form a network at the desired resolution and a well-coordinated maintenance procedure. Although this dissertation provides a good example of how the organization of such a complex enterprise can be additionally impeded by external circumstances (in this case a pandemic), the rapid transformation of FESSTVaL into its home office-conform version FESST@HH demonstrates the benefit of including a supportive citizens community to ease the site acquisition and station maintenance. Future efforts might aim to repeat a larger

version of the experiment or to establish operational measurement networks at sub-mesoscale resolution. However, with respect to the huge workload required to regularly replace batteries and collect measurement data, the operation of about 100 APOLLO and WXT stations in their current version is only feasible during a limited campaign period or after a technical update to achieve longer battery life times and reliable remote data transfer.

Beyond the technical and organizational requirements, the meaningful evaluation of observation data from a dense station network is challenging and lacks guidance from previous studies. The derivation of morphological cold pool properties from spatially distributed temperature observations involves several processing steps, including the identification of cold pool events, the definition of a robust temperature reference state in space and time, the spatial interpolation of irregularly spaced data, and the definition of individual cold pool objects that are produced by convective outflow air rather than other meteorological processes causing local temperature depressions. The presented analysis of cold pool objects also reveals the issue of cold pools being too large or only partially sampled by the station network, which seriously limits the generality of the derived size or shape. While the latter problem will remain inherent to all station networks, the described analysis procedure does not claim to be definitive and might be improved or extended in future attempts of evaluating the data set of FESSTVaL or similar subsequent measurement experiments.

## 5.2 PERSPECTIVES

The FESST@HH and FESSTVaL experiments have produced unique and extraordinary data sets. This dissertation presents only one possible way to evaluate the data, which is far from exploiting their potential to the full extent. In the following, I illustrate some of the possible ideas that should or could be implemented to continue the described investigation or to explore new pathways of research in the future.

The presented work of Study C is still unpublished but intended to be further developed for publication in a scientific journal. The statistical characterization of cold pool objects will benefit from additional analyses that help to further interpret the factors controlling the spatial properties of cold pools. This includes the question if not only the strength but also the size of cold pools is determined by the *atmospheric saturation deficit* (Study A), which can be derived from regular radiosondes profiles available for FESSTVaL. It has also not yet been considered that the size of analyzed cold pool objects should strongly depend on the *morphology of the parent precipitation field* and, more precisely, on the clustering of multiple convective cells. Moreover, the *concentric temperature structure* found for selected cold pool events needs to be statistically confirmed for all sampled cases.

More challenging problems that are beyond the scope of Study C concern the mechanisms controlling the cold pool growth. To disentangle the relative importance of the density-driven expansion compared to cold air production by precipitation, we need to observe *how far cold pools propagate after the rainfall has stopped*. Since cold pools at the end of their life cycle are usually larger than the size of the station networks used here, this issue requires the inclusion of *additional surface and radar observations* outside of the experiment area or simply a larger network in a potential follow-up campaign. In this context, more extensive vertical observations by distributed radiosonde profiles are desirable for the future to test if the *assumption of a constant cold pool height* is reasonable. This would also help to *quantify the importance of convective downdrafts for cold pool growth*, since the

vertical distribution of the temperature perturbation allows to calculate the hydrostatic and non-hydrostatic (i. e., dynamical) portion of the surface pressure perturbation. The discussed cold pool events *Elphi* and *Jogi* exhibit a directional rather than a symmetric horizontal expansion of the outflow air, which might be related to the wind field that could *favor or impede the expansion in certain directions*. This phenomenon can be further investigated with the help of direct quantification of the propagation velocity of cold pool fronts within the station network and spatial information on the vertical wind profile available from Doppler lidar measurements during FESSTVaL.

Apart from process understanding, the introduced data sets give us the opportunity to assess requirements for the design of future observational setups. The presented results already suggest that a network of about 30 km in diameter is too small to observe the entire range of cold pool sizes. However, this issue will probably remain for all networks smaller than approximately 100 km. This relates also to the question *which spatial resolution is actually needed to reliably resolve cold pool properties*, which can be answered based on the sensitivity of the presented findings to the measurement stations included into the analysis.

The dense station networks of FESST@HH and FESSTVaL provide us with brief glimpses on characteristics of cold pools that are usually invisible in conventional measurements. Although the experiments add only small pieces to the big puzzle left us by nature, they represent significant achievements for our understanding of cold pools and related convective-scale processes. Ultimately, this contribution might pave the way towards the implementation of operational sub-mesoscale measurement networks in the near and intermediate future. These will help us to collect extensive data for a comprehensive validation of hectometer-scale simulations, to improve forecasts of potentially hazardous convective events, and to reduce the uncertainty of cloud feedbacks in climate projections.

Part II

# APPENDICES

# A

# CONVECTIVE COLD POOLS IN LONG-TERM BOUNDARY LAYER MAST OBSERVATIONS

The work in this appendix has been published with minor modifications as

**Kirsch, Bastian**, Felix Ament, and Cathy Hohenegger (2021). "Convective cold pools in long-term boundary layer mast observations." In: *Mon. Weather Rev.* 149.3, pp. 811–820. DOI: 10.1175/MWR-D-20-0197.1. 

## AUTHOR CONTRIBUTIONS

**BK** conceptualized the idea, developed the methodology, performed the formal analysis, and wrote, revised, and edited the original draft. FA and CH helped to conceptualize the idea and supervised the study.

# Convective cold pools in long-term boundary layer mast observations

BASTIAN KIRSCH[1], FELIX AMENT[1,2], and CATHY HOHENEGGER[2]

[1]*Meteorological Institute, University of Hamburg, Hamburg, Germany*
[2]*Max Planck Institute for Meteorology, Hamburg, Germany*

(Manuscript received 16 June 2020, in final form 15 December 2020)

ABSTRACT

Cold pools are mesoscale features, that are key for understanding the organization of convection, but are insufficiently captured in conventional observations. This study conducts a statistical characterization of cold pool passages observed at a 280 m high boundary layer mast in Hamburg (Germany) and discusses factors controlling their signal strength. During 14 summer seasons 489 cold pool events are identified from rapid temperature drops below -2 K associated with rainfall. The cold pool activity exhibits distinct annual and diurnal cycles peaking in July and mid afternoon, respectively. The median temperature perturbation is -3.3 K at 2-m height and weakens above. Also the increase in hydrostatic air pressure and specific humidity is largest near the surface. Extrapolation of the vertically weakening pressure signal suggests a characteristic cold pool depth of about 750 m. Disturbances in the horizontal and vertical wind speed components document a lifting-induced circulation of air masses prior to the approaching cold pool front. According to a correlation analysis, the near-surface temperature perturbation is more strongly controlled by the pre-event saturation deficit ($r$=-0.71) than by the event-accumulated rainfall amount ($r$=-0.35). Simulating the observed temperature drops as idealized wet-bulb processes suggests that evaporative cooling alone explains 64 % of the variability in cold pool strength. This number increases to 92 % for cases that are not affected by advection of mid-tropospheric low-$\Theta_e$ air masses under convective downdrafts.

SIGNIFICANCE STATEMENT

Cold pools are areas of cool and dense air underneath precipitating clouds, that often trigger new convection as they spread outwards. Although cold pools are key for correctly representing convection in numerical simulations, their observational characterization is insufficient, focusing on few cases and surface measurements. We analyze meteorological observations of nearly 500 cold pool passages sampled during 14 years at a 280-m high mast in Hamburg (Germany). The robust data basis shows that the typical temperature perturbation associated with cold pools is only -3.3 K and weakens with height. The surface temperature signal is mainly driven by evaporative cooling of below-cloud air by rainfall, whereby the saturation deficit is a much better predictor than the often used precipitation amount.

## A.1 INTRODUCTION

Cold pools are mesoscale areas of cool downdraft air, that form through evaporation underneath precipitating clouds. The importance of cold pools for the variability of convective precipitation is a long-standing topic in the literature. Many studies have

described a variety of dynamical and thermodynamical processes, that relate cold pools to the formation and organization of convection. As the negatively buoyant air of a cold pool horizontally propagates on the Earth's surface as a density current, its leading edge represents a preferred region for the initiation of secondary convection. While one factor is the mechanical lifting of less dense air ahead of the cold pool front, the interplay between cold pools and vertical wind shear also has a strong impact on the organization and hence life cycle of convective squall lines (Grant et al., 2018; Rotunno et al., 1988). Furthermore, the modification of the near-surface moisture field by cold pools is thought to be important for the life cycle of convection. Studies on numerical simulations of oceanic cold pools identified their leading edge as a region of enhanced moisture in the lower troposphere, where secondary updrafts are preferably triggered (e. g., Feng et al., 2015; Tompkins, 2001; Torri et al., 2015). However, those cold pool moisture rings are rarely found in observational data (Chandra et al., 2018; de Szoeke et al., 2017) and their primary origin is still under debate (Langhans and Romps, 2015; Schlemmer and Hohenegger, 2016; Zuidema et al., 2017).

Khairoutdinov and Randall (2006) proposed that cold pools particularly favor the transition from shallow to deep convection, since they support the formation of large convective clusters, that are less affected by entrainment of drier environmental air. In this context, Schlemmer and Hohenegger (2014), Schlemmer and Hohenegger (2016) and Haerter and Schlemmer (2018) argued that the modification of surface fluxes and moisture fields by cold pools supports this positive feedback loop and the subsequent organization of convective clouds into larger clusters. As a consequence, the representation of cold pool characteristics and dynamics is a critical component for correctly simulating the diurnal cycle of precipitation (Boeing et al., 2012; Kurowski et al., 2018; Rio et al., 2009).

Cold pools are short-lived phenomena, that lead to rapid perturbations in various meteorological parameters. A large number of studies have investigated cold pool characteristics based on model simulations with a spatial resolution of $< 1\,\mathrm{km}$. Such simulations are able to explicitly resolve the scale of convective clouds. However, observational evidence is essential for validating simulated cold pool properties and related processes. Several observational studies have aimed to characterize the signal of cold pools in different climatological conditions. In the analysis of selected outflow passages in tower measurement data in Oklahoma, Goff (1976) found a sequence of typical disturbances in meteorological parameters for different thunderstorm life cycle stages. This includes a mean hydrostatic pressure rise of 2.5 hPa, followed by wind gusts of $12.8\,\mathrm{m\,s^{-1}}$ associated with a rapid shift in wind direction and a potential temperature drop of 4.3 K, occurring within 35 min prior to the onset of rainfall. Engerer et al. (2008) reported pressure increases between 3.2 hPa and 4.5 hPa, potential temperature deficits between 5.4 K and 11 K and wind gusts of at least $15\,\mathrm{m\,s^{-1}}$ associated with the passage of outflows from mesoscale convective system (MCS) storms as seen in Oklahoma Mesonet stations. Similar analyses for locations in Northern Africa can be found in Redl et al. (2015) and Provod et al. (2016). Furthermore, there exists strong observational evidence for generally much weaker signals of cold pools forming in tropical oceanic environments compared to continental mid-latitude conditions (Feng et al., 2015; Terai and Wood, 2013; Vogel, 2017; de Szoeke et al., 2017).

There have also been numerous efforts to identify factors controlling the thermodynamical properties of cold pools. In an early study, Fujita (1959) assigned the cold-air production to evaporation of precipitation in mesoscale thunderstorm systems based on surface and airborne observations over several locations in the United States. He found the total density increase by evaporation in the sub-cloud layer and the associated hydrostatic pressure rise to be proportional to the surface rainfall. Barnes and Garstang (1982) used radar

and in situ measurements over the tropical Atlantic to derive a precipitation threshold of $2\,\mathrm{mm\,h^{-1}}$ to distinguish between nonpenetrative downdrafts that are associated with light rainfall and mainly cool and moisten the sub-cloud layer, and penetrative downdrafts, that rain heavily and import lower moist static energy from above cloud base into the surface layer. By affecting evaporative cooling and the characteristics of downdraft air masses, the atmospheric profile critically affects the strength of a cold pool. Warm and dry boundary layers support strong cooling rates by rain evaporation, which is usually more important for continental convection. The relationship between cold pool strength and mid-tropospheric conditions is less straightforward. Dry air supports the formation of downdrafts through entrainment and subsequent evaporation of mid-level air, which tends to strengthen updrafts and increase the condensate mass available for evaporation (Boeing et al., 2012; Feng et al., 2015; Markowski and Richardson, 2010). The actual evaporative cooling also depends on the type of hydrometeors, e. g., rain versus ice particles, which in turn strongly depends on the present thermodynamical conditions (Engerer et al., 2008; Li et al., 2015). Turbulent mixing of environmental air into the cold pool and erosion by surface heat fluxes finally contribute to its dissipation (Gentine et al., 2016; Grant and van den Heever, 2016, 2018; Ross et al., 2004).

Considering the variety and complexity of parameters acting on the thermodynamics of cold pools, the identification of dominant processes determining their observed properties is a challenging task, that has not been satisfactorily addressed yet. In the present study we use a multiyear observational data set to provide a robust characterization of continental cold pools. Unlike existing studies, we do not restrict our analysis to pre-selected events from specific types of convection, which tend to be biased towards strong and less frequent events, but include cold pools from a wide range of meteorological conditions. Furthermore, we aim to quantitatively estimate the relevance of the prevailing atmospheric conditions for explaining the observed variability in the near-surface temperature signal and disentangle the impact of evaporative cooling and convective import of upper-level air masses. The presented results could serve as a reference data set for modeled cold pool properties in state-of-the-art Large-Eddy simulations (LES) and provide guidance for the identification of potential model biases. The study is structured as follows: after introducing the used data set and applied method for cold pool identification in section A.2, we discuss the signal characteristics of the observed events in section A.3. In section A.4 we focus on the factors controlling the cold pool strength, followed by a summary of the overall findings in section A.5.

## A.2 DATA AND METHODOLOGY

### A.2.1 *Observational data set*

This study analyzes meteorological observation data from the Weather Mast Hamburg (WMH) boundary layer tower in Hamburg (Germany). The measurement facility is installed at a television broadcasting tower located in the eastern outskirts of the city (53.5192°N, 10.1029°E). The 305-m high main mast is equipped with instrumentation at platforms in six different heights, while near-surface measurements are conducted at a 12-m mast located in 170 m distance on a nearby meadow. The instrumentation of the main mast relevant for the present study consists of platinum resistance thermometers (Pt-100), HMP 45 humidity sensors and 3D ultrasonic anemometers, while the near-surface observations are accomplished by PTB 200 A pressure sensors and a tipping bucket rain gauge. All

measurements are available at 1 min temporal resolution. A more detailed description of the measurement site and instrumentation can be found in Bruemmer et al. (2012).

For the present analysis we use observational data from 14 summer seasons (1 April to 30 September) between 2006 and 2019 from five height levels (2 m, 50 m, 110 m, 175 m and 280 m), while the lowest wind speed measurements refer to 10 m height. For years before 2011 the topmost available measurement height is 250 m. Since air pressure is only recorded at the surface, we calculate its values at the four upper levels from the respective temperature data by applying the hydrostatic equation between the observed heights. These pressure values also go into the calculation of the equivalent potential temperature after Bolton (1980), which we mainly use to interpret controls on cold pool properties.

### A.2.2 *Detection and definition of cold pool events*

The investigation of observed cold pool characteristics first requires the identification of their footprints in local meteorological parameters. Since a subjective identification of single cold pool events in multiyear data is unfeasible, we apply an objective detection method based on simple threshold criteria (Kirsch, 2020). To minimize the influence of prescribed constraints on our results, the algorithm only takes 2-m air temperature $T_2$ and rainfall rate $R$ as input parameters. For the identification of cold pool-related signals in the measurement records, the algorithm scans the input temperature time series for a difference of $\Delta T_2 \leq -2\,\mathrm{K}$ within 20 min after the current time step. The first of the subsequent time steps satisfying a temperature decrease of at least 0.5 K then defines the begin of the cold pool event, denoted by $t_0$. Subsequent decreases in temperature within the following 60 min are considered to be part of the same event. To attribute the detected temperature drops to the passage of a convectively-driven cold pool rather than local meteorological effects, identified events without rainfall within one hour after $t_0$ are excluded. The same is true for very rare events that include missing values either in the temperature or rainfall record from 30 min before to 60 min after $t_0$.

The detection method identifies an overall number of 489 temperature drops satisfying the applied criteria. We consider the discussed results as statistically representative, since the temperature data availability per summer season is always larger than 95.3 % and above 99 % in 11 out of 14 years. As the applied cold pool-detection algorithm is only based on the local temperature and rainfall record and does not use any information about the origin of the identified temperature drops, the results are potentially affected by the misinterpretation of synoptic-scale cold-frontal passages as local-scale cold pool events. The manual inspection of 6-hourly surface analysis charts (Deutscher Wetterdienst, 2019) for 2017 and 2018, representing years with a very high and very low number of identified events, shows that 20.5 % and 11.5 % of the detected events occurred within a time range of 2 hours before or after a cold-front passage, respectively. Still these events might not have been directly caused by the cold front itself, but rather by pre-frontal convection or convective cells embedded into the front.

For a coherent description of short-term meteorological signals during a cold pool-front passage, we consider a unified analysis scheme for the different variables. To calculate the signal strength in each variable, we first define its unperturbed state as the median value of the 30-min period prior to the detected begin of the event $t_0$, which is more robust against the imprecise timing of $t_0$ than taking the arithmetic mean. The signal strength is then given by the difference between this unperturbed state and the extreme value within 60 min after $t_0$. According to the sign of the respective signal, we define the extreme value as the minimum value for temperature $T$ and equivalent potential temperature $\Theta_e$ and

the maximum value for air pressure $p$, specific humidity $q$, horizontal wind speed $U$ and vertical wind speed $w$. In the case of $w$, the maximum values refers to the entire 90 min period to include also signals prior to the cold pool-front passage. For each event, the same $t_0$ is used for all measurement heights and variables. Missing observations of $p$, $q$ or $U$ slightly reduce the number of cases considered in the analysis to at least 448 of the 489 detected cases. The data for $w$ only includes between 216 and 245 cases, as the variable was not measured before 2013.

## A.3 OBSERVED COLD POOL CHARACTERISTICS

### A.3.1 *Frequency of events*

As the first step to analyze the observed cold pools, we determine the frequency and occurrence of events. The annual number of events exhibits a large variability with a mean of 34.9±6.8 events (Figure A.1a), however, the cold pool activity follows a distinct annual cycle peaking in July (7.6 events per month) and a sharp weakening towards the end of the summer season in September (3.2 events per month; Figure A.1b). Furthermore, cold pools mainly occur during the second half of the day with a pronounced frequency peak at 1500 local time (Figure A.1c). These statistics confirm, that the detected temperature drops are tightly connected to convective activity, as expected. The observed diurnal cycle in cold pool frequency with a distinct minimum in the early morning hours also proves a lack of contamination of the presented results by synoptic-scale cold fronts.

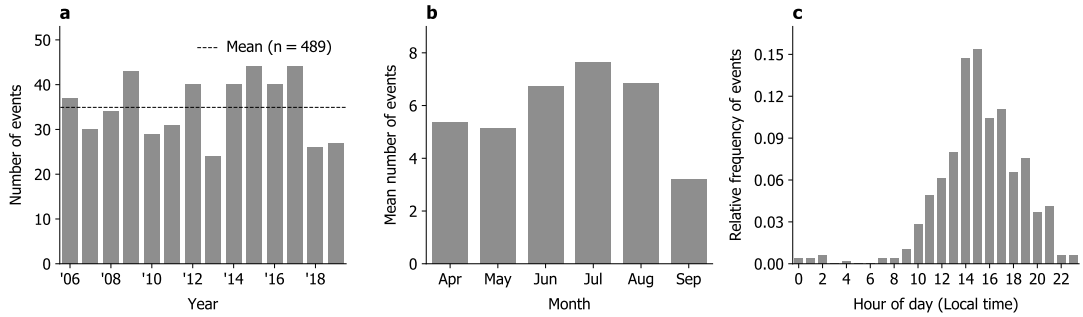


Figure A.1: Occurrence of cold pool events detected at WMH between 2006 and 2019: (a) number of events per summer season (1 Apr–30 Sep), (b) mean annual cycle, and (c) mean diurnal cycle.

### A.3.2 *Strength and temporal evolution of signal*

We further characterize the observed properties of cold pools by studying the frequency distributions of the detected signals (Figure A.2) and the mean time series during the events (Figure A.3). Figure A.2a indicates that the 2-m temperature perturbation $\Delta T_2$ exhibits a median of -3.3 K and a minimum value of -10.8 K. As expected, the magnitude of the values is by several kelvins smaller than the ones reported by Engerer et al. (2008), who only included cases from MCS storms into their analysis. Width and skewness of the distribution is similar between the different measurement heights, however, the median signal strength constantly weakens with height to -2.4 K at 280 m. From the weakening temperature signal we can conclude that the temperature inside the cold pool air generally

decreases less strongly with height than outside of it. Therefore, we find evidence for an increased atmospheric stability within a cold pool compared to its surrounding. According to Figure A.3a, $\Delta T$ generally exhibits its largest gradient to the surrounding within 15 min after $t_0$. The early onset of the temperature drop a few minutes before $t_0$ results from the chosen thresholds to define a cold pool event. After the strongest perturbation is reached 20 to 25 min after $t_0$, the temperature only recovers marginally, since a large fraction of the recorded events occurred after the diurnal maximum of solar heating. Moreover, this slow recovery could also indicate that the cold pool is still passing over the measurement site, even one hour after its arrival. With a typical advection velocity of $10\,\mathrm{m\,s^{-1}}$, this would imply a cold pool size of 30 km to 40 km, which could also be potentially observed in operational station networks.

The pressure signal $\Delta p_2$ is mostly confined to $\leq$2 hPa, while extreme cases of up to 5.9 hPa are observed (Figure A.2b). These values are by more than a factor of 2 smaller than for MCS-type cold pools as found by Engerer et al. (2008). Similar to the temperature signal, also $\Delta p$ constantly decreases with height from a median of 0.7 hPa near the surface to 0.5 hPa at the upper-most height, as a direct result of the hydrostatic relationship employed to infer $p$ at higher levels. The onset of $\Delta p$ starts approximately 15 min earlier than that of $\Delta T$ (Figure A.3b), which is in line with the findings of other authors (Engerer et al., 2008; Goff, 1976). The slight decline in pressure excess about 15 min after $t_0$ may be a sign of the partially nonhydrostatic nature of the initial perturbation due to dynamical effects at the propagating cold-air boundary (Houze, 1993; Markowski and Richardson, 2010). The importance of nonhydrostatic effects for the observed pressure signal during cold pool events would require further investigation, which is beyond the scope of this study.

The majority of observed cold pool passages leads to an moistening of the air, as shown in Figures A.2c and A.3c. Based on a median of $1\,\mathrm{g\,kg^{-1}}$ near the surface and approximately $0.6\,\mathrm{g\,kg^{-1}}$ at 280 m above ground, $\Delta q$ indicates a slight weakening of the moistening with height, however, magnitude and even sign of the signal are highly variable throughout all observation heights. For the present definition of $\Delta q$, i. e., using the difference between the unperturbed state and the maximum post-passage value, about 10 % of the cases even show a decrease in humidity. This number increases to about 25 %, if the median value of $q$ within 60 min after the passage would be considered to calculate $\Delta q$. The large variability in $\Delta q$ most likely reflects the interplay of different cold pool-formation processes, namely evaporation, that would moisten the cold pool, and convective import of upper-layer air masses, that would dry it. This interplay is discussed in section A.4. However, a clear moisture ring along the cold pool edge, as reported from numerical simulations, is not visible. The difficulty in observing a moisture ring is consistent with past observational studies, which have revealed inconsistencies in magnitude and sign of the cold pool moisture signal in different climatic regimes (Feng et al., 2015; Provod et al., 2016; Redl et al., 2015; Vogel, 2017; de Szoeke et al., 2017). The weak temporary dip in $\Delta q$ just after $t_0$ in Figure A.3c is not of physical nature, but an instrumental artifact of the humidity sensor used before 2018 and relates to a longer response time compared to the temperature sensor. Most likely this issue also explains the longer equilibration time of the $\Delta q$ signal compared to $\Delta T$ and $\Delta p$.

Combining the effects of temperature and humidity, also the perturbation in equivalent potential temperature $\Delta\Theta_e$ gives insights into properties of the observed cold pools (Figures A.2d and A.3d). Similar to $\Delta T$, the near-surface perturbation in $\Theta_e$ exhibits a median of -3.2 K and much larger extreme values of up to -15 K. However, $\Delta\Theta_e$ does not significantly vary with height. Since the pre-event $\Theta_e$ is also generally uniform with height

(not shown), this suggests that $\Theta_e$ inside the cold pool does not significantly vary with height either. From this we conclude that the horizontal mixing between cold pool and environmental air throughout the lowest 280 m of the atmosphere is generally very limited. The steeper time derivative in $\Delta\Theta_e$ just after the detected cold pool passage compared to $\Delta T$ also results from the same instrumental artifact in the measurement of $q$, as already discussed.

Finally, the passage of a cold pool front goes along with a significant disturbance of the local wind field. The mean temporal evolution of $\Delta U$ indicates a distinct peak in horizontal wind speed just after $t_0$ throughout all heights (Figure A.3e). $\Delta U$ exhibits a median of $3.6\,\mathrm{m\,s^{-1}}$ at 10 m, while this value increases to $5.4\,\mathrm{m\,s^{-1}}$ at 50 m, but stays almost constant above (Figure A.2e). Only for extreme cases $\Delta U$ continuously increases with height from $11.0\,\mathrm{m\,s^{-1}}$ near the surface to $23.5\,\mathrm{m\,s^{-1}}$ at the top of the mast. The profile of $\Delta U$ as well as the constantly increasing width of the peak with height result from the deceleration of wind gusts close to the surface by friction. The mean time series of the perturbation in vertical wind speed $\Delta w$ shows a distinct and short-lived peak shortly before the detected passage of the cold pool front (Figure A.3f). Since the amplitude of the peak clearly exceeds the turbulence-induced noise level, it is indicative for a laminar flow feature that is consistently present throughout a large number of events. In combination with the following period of negative perturbations, this signature clearly marks the lifting of air masses prior to the arriving cold pool air with compensating subsidence afterwards. In contrast to $\Delta U$, both the median of $\Delta w$ ($\Delta w_{10} = 0.6\,\mathrm{m\,s^{-1}}$, $\Delta w_{280} = 1.8\,\mathrm{m\,s^{-1}}$) and its maximum values constantly increase with height, which marks a stronger lifting of air masses aloft (Figure A.2f). In summary, the coherent signals of $\Delta U$ and $\Delta w$ suggest the presence of a lifting-induced overturning circulation ahead of the cold pool front.

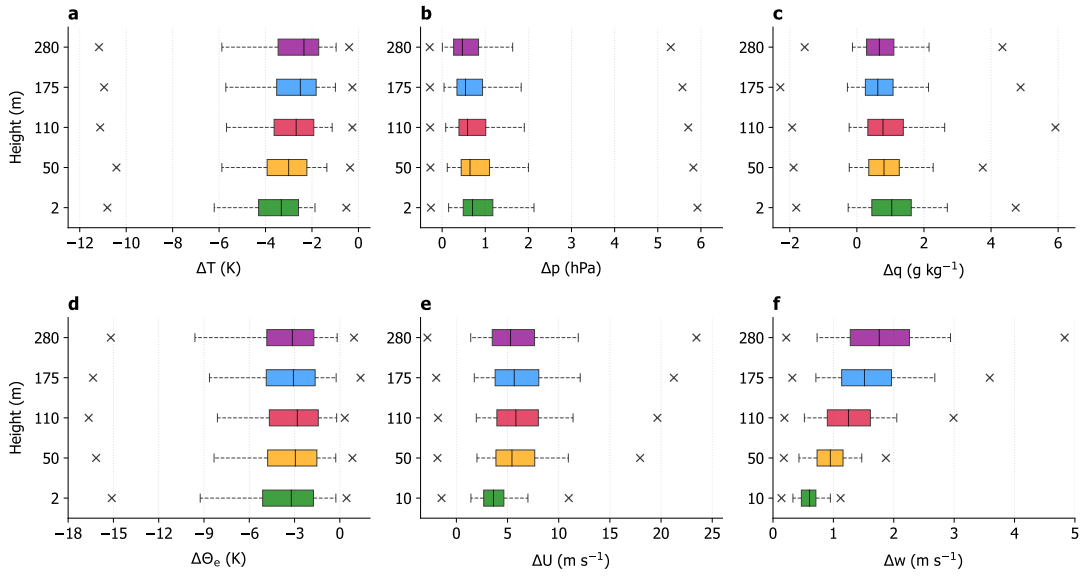


Figure A.2: Height-dependent distributions of perturbations in (a) air temperature $T$, (b) pressure $p$, (c) specific humidity $q$, (d) equivalent potential temperature $\Theta_e$, (e) horizontal wind speed $U$ and (f) vertical wind speed $w$ during cold pool passages at WMH between 2006 and 2019. Vertical lines, boxes and whiskers represent median, inter-quartile range and 5% and 95% quantiles, respectively, while crosses mark the extreme values.

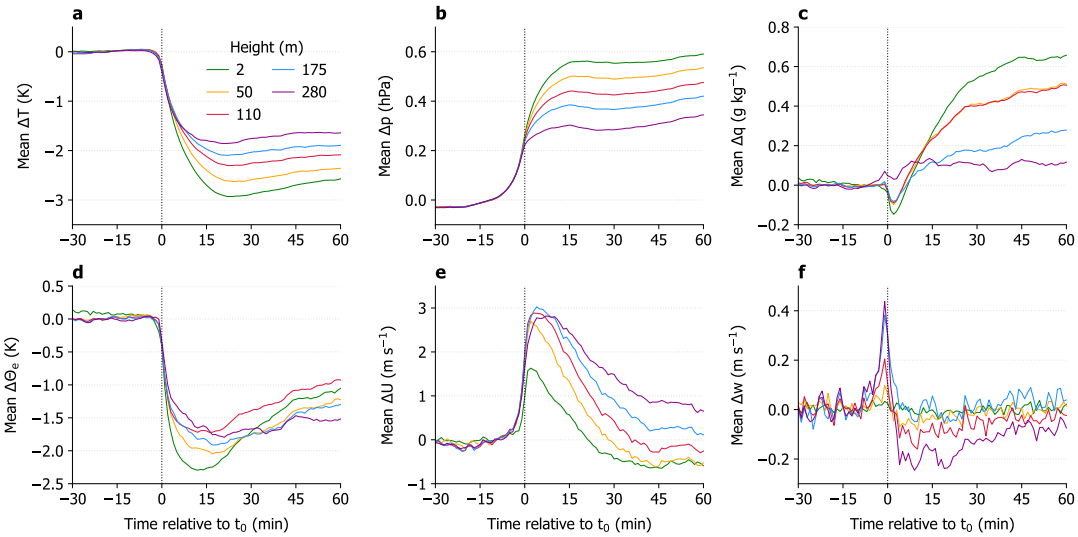


Figure A.3: As in Figure A.2, but for the mean temporal evolution of the quantities relative to the detected cold pool-front passage $t_0$.

### A.3.3 *Cold pool depth*

Consistent with early studies on the vertical structure of convective cold air outflows (e. g., Barnes and Garstang, 1982; Fujita, 1959), our results in section A.3A.3.2 confirm the strongest thermodynamical signal of a cold pool to be near the surface and to constantly weaken with height. We use the information of vertical gradients to infer the depth of individual cold pools. According to the hydrostatic relationship, the perturbation in air pressure $\Delta p$ induced by the additional weight of the dense cold pool air decreases approximately linearly with height. Therefore, the linear extrapolation of this gradient to the height where $\Delta p$ vanishes provides an estimate of the cold pool depth (Figure A.4a). We apply this method to cold pool events that exhibit positive pressure perturbations for all measurement heights and satisfy the linear relationship between $\Delta p$ and height according to an overall correlation coefficient of at least 0.95 for the entire profile. Furthermore, we neglect three cases for which the method yields unrealistically large ($> 4$ km) values. A potential source of uncertainty might be the fact that the pressure signal is measured only at surface level and hydrostatically calculated from the respective temperature profile for the levels above. Figure A.4b illustrates the resulting frequency distribution of cold pool depths for 419 valid cases, showing an estimated depth of between a few 100 m and almost 2000 m for most events and a median of 746 m. This result is in good agreement with Markowski and Richardson (2010), who reported a typical depth of 1 km for continental convective outflows. In contrast, corresponding values for tropical oceanic outflows are substantially smaller ($< 500$ m), consistent with the lower cloud base height (Terai and Wood, 2013; de Szoeke et al., 2017).

## A.4 FACTORS CONTROLLING THE COLD POOL STRENGTH

The results discussed in section A.3 illustrate the distinct footprint of observed cold pool passages in various meteorological parameters. However, the cold pool characteristics also largely vary case-to-case from the average, e. g., reflected by the temperature perturbation

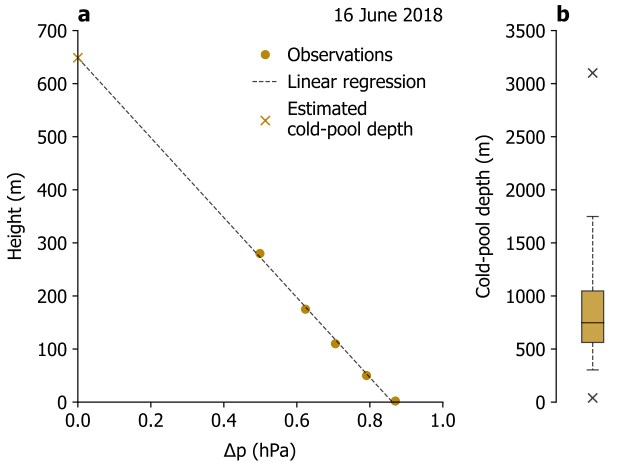


Figure A.4: (a) Height-dependent pressure perturbation $\Delta p$ for a cold pool event on 16 Jun 2018 and linear extrapolation for estimation of cold pool depth and (b) distribution of estimated cold pool depth for all cases between 2006 and 2019 that satisfy the linear model and yield depths $>$ 4 km. Horizontal line, box and whiskers represent the median, interquartile range and the 5% and 95% quantiles, respectively, while crosses mark the extreme values.

$\Delta T$ ranging between -2 K and almost -11 K. Since the surface temperature signal of a convective outflow is indicative of its mass excess and, therefore, its potential to propagate and induce secondary convection, the explanation of its variability is an important step towards an improved understanding of convective organization. Based on the present observational data set we aim to identify the main factors controlling the observed cold pool strength. In our analyses we consider the strength of cold pools solely in terms of temperature perturbation $\Delta T$.

### A.4.1 *Observational evidence*

In order to investigate the variability in cold pool strength, we first quantify its observed degree of relation with potential controlling factors. As a first approximation we assume cold pools to be mainly formed by evaporation underneath precipitating clouds and expect $\Delta T$ to be determined by the amount of rainwater in the sub-cloud layer available for evaporation. Figure A.5a shows the distribution of $\Delta T$ as a function of the accumulated rainfall amount measured during the 90-min reference period of the cold pool event. Although the median strength constantly increases from -2.7 K for weak-precipitation events to -4.0 K for strong-precipitation events, the linear correlation is weak (correlation coefficient $r = -0.35$). One reason for this weak relationship might be the poor representativeness of a surface rainfall point measurement. However, the inclusion of radar-based spatially distributed rainfall information does not significantly change the result (not shown).

The second relevant factor in controlling the degree of cooling by rainfall is the evaporation potential of the sub-cloud layer air. We quantify the potential for evaporative cooling via the absolute saturation deficit,that is given by the difference between saturation specific humidity $q_{\text{sat}}$ and specific humidity $q$ and mainly depends on the temperature and humidity of the given air mass. This quantity can be considered as independent from the rainfall amount, since both factors are practically uncorrelated ($r = 0.05$). As Figure A.5b

shows, $\Delta T$ has a stronger dependence on the pre-event saturation deficit than on the accumulated rainfall ($r = -0.71$). The amplification of cold pool strength with increasing saturation deficit is especially striking for the 20 % most under-saturated cases, that exhibit a median temperature deficit of -4.9 K. These results provide observational evidence that both the amount of rainfall and the evaporation potential of the pre-event air actually control the strength of the cold pool temperature signal, with the latter being the more important one.

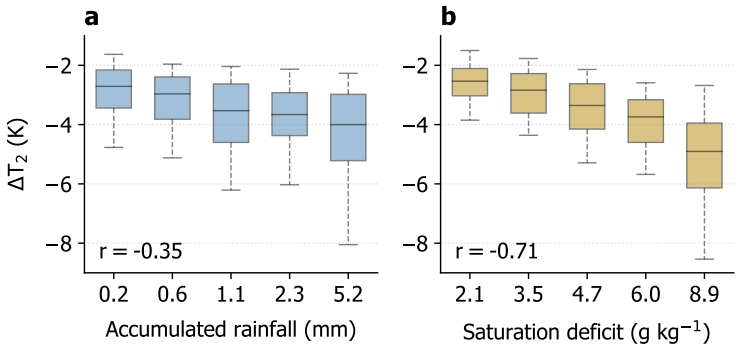


Figure A.5: Distribution of cold pool 2-m air temperature perturbation $\Delta T_2$ dependent on (a) event-accumulated rainfall and (b) pre-event median saturation deficit $q_{\text{sat}} - q$. Box plots use 20-% quantile interval bins labeled with the median values of each bin. Vertical lines, boxes and whiskers mark the median, interquartile range and the 5% and 95% quantiles, respectively. The linear correlation coefficient $r$ indicated in (a) is calculated between the logarithmic rainfall amount and $\Delta T_2$.

### A.4.2 *Role of evaporation*

We further explore the importance of evaporative cooling for the observed cold pool strength by simulating it in a simple thermodynamical model. In this model we assume that evaporation of rainfall cools and moistens an air parcel in the sub-cloud layer according to the wet-bulb process. When liquid water of mass $\Delta m_{\text{w}}$ adiabatically and isobarically evaporates at the expense of the thermal energy of the air parcel, then its temperature approximately changes by

$$\Delta T \approx -\frac{L_{\text{v}}}{c_{\text{p}}} \Delta r_{\text{v}}. \tag{A.1}$$

Accordingly, the water vapor mixing ratio $r_{\text{v}}$ increases by $\Delta r_{\text{v}} = \Delta m_{\text{w}} / m_{\text{a}}$, where $m_{\text{a}}$ denotes the mass of dry air. $L_{\text{v}}$ and $c_{\text{p}}$ are the latent heat of evaporation of water and the specific heat capacity of dry air, respectively, whereas we neglect the change in specific heat capacity due to the increase in humidity.

For each cold pool event we initialize the model with the observed pre-event temperature and relative humidity and let rain water evaporate until the air mass reaches an equilibrium state. We define two equilibrium states of the model: firstly, the maximum wet-bulb temperature depression $\Delta T_{\text{mod,sat}}$, where the considered air parcel cools and moistens until saturation is reached; secondly, the temperature depression $\Delta T_{\text{mod,obs}}$, that denotes the state when the simulated relative humidity reaches the maximum value that was actually observed after the respective cold pool passage, allowing for a more realistic

under-saturated state. Since the cooling of the air parcel during the wet-bulb process also reduces its saturation vapor pressure and again impacts the moistening required to reach the respective equilibrium states, we cannot solve Equation A.1 directly. To realistically simulate this process we iteratively increase $r_v$ by sufficiently small increments $\Delta r_{v,i} \approx 10^{-6}\,\mathrm{kg\,kg^{-1}}$ and adjust temperature and humidity of the air parcel accordingly.

The statistical analysis in Figure A.6a shows a reasonable agreement between the observed $\Delta T$ and its modeled values of maximum evaporative cooling $\Delta T_{\mathrm{mod,sat}}$ with a correlation coefficient of $r = 0.67$ and a root mean square error (RMSE) of 1.7 K. In this configuration the simple model tends to overestimate the cold pool strength, especially for strong events. This indicates that in most cases the pre-cold pool air is not moistened to saturation and, therefore, the full evaporation potential is not exploited. To test this hypothesis, we repeat the same analysis using the second model configuration $\Delta T_{\mathrm{mod,obs}}$, that takes into account the actually observed moistening of the air (Figure A.6b). As a consequence, the agreement between observed and modeled cold pool strength considerably improves ($r = 0.80$, RMSE = 1.3 K). This leads to the conclusion that 64 % of the variability in cold pool strength may be explained by local evaporative cooling in the sub-cloud layer.

In the previous considerations we have approximated the process of cold pool formation by moist-adiabatic cooling of the sub-cloud air mass. However, under these conditions $\Theta_e$ would be same inside and outside of the cold pool, which on average is not the case (Figure A.3d). In fact, a negative perturbation in $\Theta_e$ indicates the convective import of cooler and drier mid-tropospheric air into the atmospheric surface layer, that superposes with local evaporative cooling. Since the strength and thermodynamical properties of local downdrafts are highly case-dependent, we can treat $\Delta\Theta_e$ as an indicator for the strength of the vertical import of low-$\Theta_e$ air into the surface layer. Figure A.6c shows the skillfulness of the evaporation model, as quantified by its RMSE, bias and correlation coefficient with respect to the observed cold pool strength, as in Figs. A.6a and b, stratified by observed $\Delta\Theta_e$. For the case of evaporative cooling according to observed moistening, the model RMSE is smallest for small $\Delta\Theta_e$ (0.6 K) and constantly increases for increasingly negative $\Delta\Theta_e$ (2.2 K). In cases of large absolute $\Delta\Theta_e$ the model bias is positive indicating an underestimation in cold pool strength in agreement with the strong vertical advection of low-$\Theta_e$ air in such cases. In contrast, for the case of maximum evaporative cooling the model error shows an opposite dependence on $\Delta\Theta_e$, which mainly reflects the previously described overestimation in cold pool strength, that is compensated by increasingly larger $\Delta\Theta_e$. In a sense, the estimated too large evaporative cooling masks the effect of the missing vertical advection of low-$\Theta_e$ air, the more so, the stronger the advection.

Despite the simple concepts of the used analysis methods, the presented results provide observational evidence for the generation process of cold pools. Without the convective import of cool and dry upper-level air (i. e., for the 20 % of cases with smallest perturbations in $\Theta_e$ corresponding to $\Delta\Theta_e > -1.5$ K), local evaporative cooling of the present sub-cloud layer air by rainfall even explains 92 % of the variability in observed near-surface temperature perturbation of a cold pool ($r = 0.96$). Figure A.7a shows such a cold pool event, whose temperature signal is mainly driven by evaporation. In those cases $\Theta_e$ is approximately conserved and the observed temperature perturbation agrees well with $\Delta T_{\mathrm{mod,obs}}$. In contrast, for the 20 % of cases with largest $\Delta\Theta_e$ ($< -5.6$ K), the evaporation model fails to reproduce the observed $\Delta T$. For such mainly downdraft-driven cold pool events the model lacks information about the thermodynamical properties of the advected air mass and underestimates the strength of the observed temperature signal, that may even overcompensate the error produced by $\Delta T_{\mathrm{mod,sat}}$ (Figure A.7b). This also becomes

manifest in the weak relationship between $\Delta T$ and $\Delta\Theta_e$ ($r = 0.37$). Even though evaporative cooling explains the largest part of variability in the temperature signal, only 13 % of the observed cold pool passages are unaffected by convective downdrafts (i. e., $\Delta\Theta_e > -1\,\mathrm{K}$) and, therefore, entirely evaporation-driven. Barnes and Garstang (1982) named a parent rainfall rate of $2\,\mathrm{mm\,h^{-1}}$ as the main criterion for downdrafts to transport upper-level air into the surface layer, still the present data does not show a significant relationship between the maximum observed rainfall rate and $\Delta\Theta_e$ ($r = -0.38$). Another aspect in the interpretation of the results is the cold pool life cycle stage. Since our analysis does not include the horizontal dimension of the observed cold pools, we miss information on the position of the measurement site relative to the parent convection as well as the cold pool age. Engerer et al. (2008) and others showed that the local outflow properties considerably vary with the convective life cycle. Therefore, our 13 % of entirely evaporation-driven cold pools may also be interpreted as young cold pools, although this needs to be confirmed by further research.

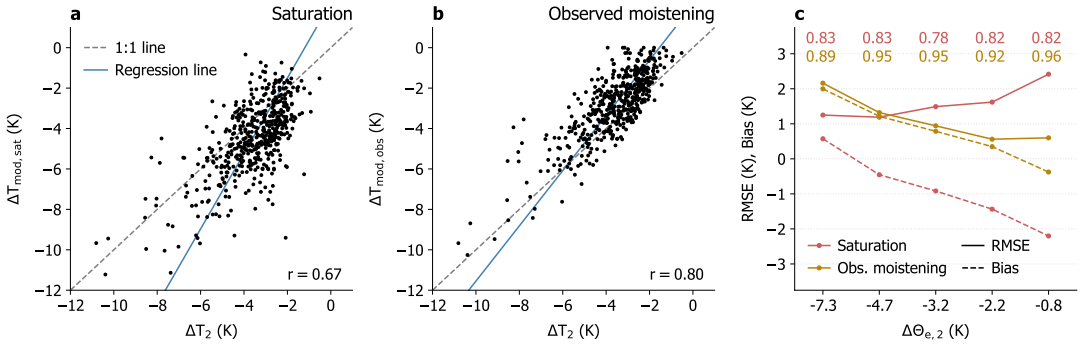


Figure A.6: Relationship between observed 2-m air temperature perturbation $\Delta T_2$ and modeled temperature perturbations (a) $\Delta T_{\mathrm{mod,sat}}$ and (b) $\Delta T_{\mathrm{mod,obs}}$, corresponding to evaporative cooling until saturation and maximum relative humidity observed after the cold pool passage is reached, respectively. Panel (c) illustrates root mean square error, bias and linear correlation coefficient $r$ (indicated as numbers) for both cases as a function of observed 2-m equivalent potential temperature perturbation $\Delta\Theta_{e,2}$, binned in 20-% quantile intervals and labeled with the median values of each bin.

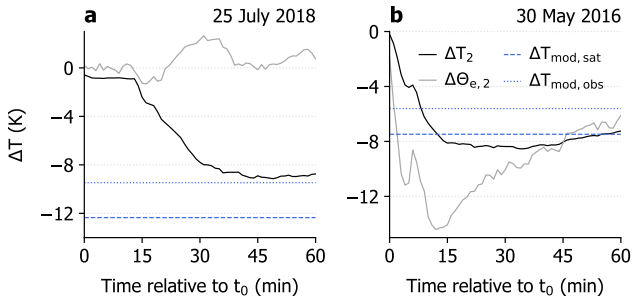


Figure A.7: Time series of observed 2-m temperature perturbation $\Delta T_2$ and equivalent potential temperature perturbation $\Delta\Theta_{e,2}$ during cold pool events on (a) at 1642 LT on 25 July 2018 and (b) at 1612 LT on 30 May 2016. Also indicated are the modeled temperature perturbations $\Delta T_{\mathrm{mod,sat}}$ and $\Delta T_{\mathrm{mod,obs}}$.

## A.5 SUMMARY AND CONCLUSIONS

In this paper we use multiyear boundary layer mast observations in Hamburg (Germany) to derive an observational reference data set of the characteristics of convective cold pools. We define a cold pool event as a 90-min time period that includes a drop in 2-m air temperature of at least 2 K within 20 min in association with local rainfall. For the analyzed 14-year period between 2006 and 2019 the annual number of observed cold pools varies between 24 and 44 events per summer season, while the monthly number follows an annual cycle with its maximum in July. Furthermore, the average cold pool activity exhibits a distinct diurnal cycle peaking in the afternoon hours.

Based on the meteorological record we find that the majority of events is associated with a median 2-m temperature perturbation of -3.3 K, while extreme cases reach up to -10.8 K. The constant weakening of the observed temperature signal with height suggests an increased atmospheric stability inside a cold pool compared to its surrounding. For the analyzed events we find an average hydrostatic air pressure rise of 0.7 hPa near the surface with the tendency for a weaker signal above. Consistent with the findings of other studies, the onset of the pressure rise generally precedes the temperature signal by approximately 15 min. By extrapolating the vertical gradient in hydrostatic pressure perturbation for individual cases we estimate a median cold pool depth of 746 m. According to the perturbation in specific humidity, a cold pool passage leads to an average moistening of the air by about $1\,\mathrm{g\,kg^{-1}}$, however, strength and even sign of the signal are highly variable throughout all measurement heights. Also, a clear moisture ring around the cold pool, as generally found in numerical simulations, was not easily recognizable in our observations. Finally, we find significant disturbances of the local wind field, that are increasingly intense away from the surface, expressed by a median horizontal wind speed perturbation of $3.6\,\mathrm{m\,s^{-1}}$ ($5.3\,\mathrm{m\,s^{-1}}$) at 10 m (280 m) height. A distinct and short-lived peak in the vertical wind component minutes prior to the approaching gust front also marks the presence of a lifting-induced circulation ahead of the cold pool.

In the second part of the study we discuss controlling factors of the variability in cold pool strength to better understand the cold-air production in convective outflows. Observational evidence suggests that contrarily to usual thinking the near-surface temperature perturbation only weakly correlates with the amount of surface rainfall ($r = -0.35$), whereas its statistical relationship with the pre-event saturation deficit is much stronger ($r = -0.71$). To further explore the importance of evaporation for the cold pool formation, we use a simple thermodynamical model, that simulates the wet-bulb cooling process for air of given temperature and humidity. Under the assumption of maximum evaporative cooling, i. e., when saturation is reached, the model is able to reproduce the observed temperature perturbations reasonably well ($r = 0.67$, RMSE $= 1.7$ K), although it tends to overestimate especially the strength of strong cold pools. The model error considerably decreases, when the evaporative cooling is confined to moistening that corresponds to the maximum observed relative humidity for the respective event ($r = 0.80$, RMSE $= 1.3$ K). Therefore, we find that local evaporative cooling of sub-cloud layer air by rainfall explains 64 % of the overall variability in cold pool strength. For cases without considerable import of cooler and drier mid-tropospheric air by convective downdrafts, indicated by small perturbations of $\Theta_e$, this number even increases to 92 %. In contrast, $\Delta\Theta_e$ itself only explains 14 % of the observed variance ($r = 0.37$), meaning that the vertical transport of upper-level air masses is a secondary driver for the local temperature signal of a cold pool, that more or less strongly superposes the evaporation process.

Our current understanding of the dynamical and thermodynamical characteristics of cold pools as well as how they interact with their environment is very limited and needs to rely on state-of-the-art convection-resolving simulations. Due to the importance of cold pools for understanding and correctly simulating the organization of convection, the validation of these models requires robust reference data of cold pools. Our work sheds light on the observed properties of continental cold pools over a wider range of meteorological conditions than previous studies have described and identifies processes controlling their signal strength. Nevertheless, current operational networks lack spatial density and sufficient temporal resolution, that is vital to observe morphological properties like size, shape and propagation velocity of cold pools and the sub-mesoscale variability of thermodynamical fields. Our results suggest that future research efforts should focus on the design of observational networks at sub-mesoscale resolution, that allow insights into the moisture distributions within cold pools, the interaction with turbulent surface fluxes and the importance of nonhydrostatic pressure effects as an indication of convective downdrafts. This could be achieved using low-budget weather stations and citizen-science approaches. These are essential steps towards a comprehensive understanding of moist convection and its more realistic representation in convection-resolving simulations.

## ACKNOWLEDGMENTS

This research was carried out in the Hans Ertel Center for Weather Research (HErZ). This German research network of universities, research institutions, and the German Weather Service (DWD) is funded by the BMVI (Federal Ministry of Transport and Digital Infrastructure). The Center for Earth System Research and Sustainability (CEN) and the Max-Planck-Institute for Meteorology support long-term observations at Hamburg Weather Mast. This research contributes to the Cluster of Excellence *CLICCS - Climate, Climatic Change, and Society* (CLICCS) Topic A3 and A2.

We thank Adrian Tompkins and two anonymous reviewers for providing us with helpful comments that improved the quality of the manuscript. Furthermore, we thank Bjorn Stevens for pointing to the importance of $\Theta_e$ for this study.

## DATA AVAILABILITY STATEMENT

All observational data and analysis software used during this study are openly available from the long-term archive of the German Climate Computing Center (DKRZ) at http://cera-www.dkrz.de/WDCC/ui/Compact.jsp?acronym=DKRZ_LTA_203_ds00002.

# B

# SUB-MESOSCALE OBSERVATIONS OF CONVECTIVE COLD POOLS WITH A DENSE STATION NETWORK IN HAMBURG, GERMANY

The work in this appendix has been published with minor modifications as

**Kirsch, Bastian**, Cathy Hohenegger, Daniel Klocke, Rainer Senke, Michael Offermann, and Felix Ament (2022). "Sub-mesoscale observations of convective cold pools with a dense station network in Hamburg, Germany." In: *Earth Syst. Sci. Data* 14.8, pp. 3531–3548. DOI: 10.5194/ESSD-14-3531-2022.

## AUTHOR CONTRIBUTIONS

**BK** helped to design, assemble, test, install, and operate the instruments, compiled the meta data, processed the measurement data, performed the formal analysis (except for Section B.6.2 and Section B.6.3), and wrote (except for Section B.6.2 and Section B.6.3), revised, and edited the original draft. CH and DK conceptualized the idea for the experiment, supervised the project, and did the project administration. RS designed, assembled, and tested the hardware and software for the APOLLO. MO designed and tested the WXT weather stations and helped to assemble, install, and operate the instruments. FA conceptualized the idea for the experiment, supervised the project, helped to design, install, and operate the instruments, performed the formal analysis for Section B.6.2 and Section B.6.3, and wrote the original draft of Section B.6.2 and Section B.6.3.

# Sub-mesoscale observations of convective cold pools with a dense station network in Hamburg, Germany

Bastian Kirsch[1,4], Cathy Hohenegger[2,4], Daniel Klocke[3,2,4], Rainer Senke[1], Michael Offermann[1], and Felix Ament[1,2,4]

[1]*Meteorological Institute, University of Hamburg, Hamburg, Germany*
[2]*Max Planck Institute for Meteorology, Hamburg, Germany*
[3]*Deutscher Wetterdienst, Offenbach am Main, Germany*
[4]*Hans Ertel Centre for Weather Research, Branch Model Development - Convection, Hamburg, Germany*

Received: 29 November 2021 — Discussion started: 3 March 2022 —
Revised: 4 July 2022 — Accepted: 16 July 2022 — Published: 4 August 2022

## ABSTRACT

From June to August 2020, an observational network of 103 meteorological ground-based stations covered the greater area (50 km × 35 km) of Hamburg (Germany) as part of the Field Experiment on Sub-mesoscale Spatio Temporal variability at Hanseatic city of Hamburg (FESST@HH). The purpose of the experiment was to shed light on the sub-mesoscale ($\mathcal{O}(100)$ m – $\mathcal{O}(10)$ km) structure of convective cold pools that typically remain under-resolved in operational networks. During the experiment, 82 custom-built, low-cost Autonomous cold POoL LOgger (APOLLO) stations sampled air temperature and pressure with fast-response sensors at 1 s resolution to adequately capture the strong and rapid perturbations associated with propagating cold pool fronts. A secondary network of 21 weather stations with commercial sensors provided additional information on relative humidity, wind speed, and precipitation at 10 s resolution. The realization of the experiment during the COVID-19 pandemic was facilitated by a large number of volunteers who provided measurement sites on their premises and supported station maintenance. This article introduces the novel type of autonomously operating instruments, their measurement characteristics, and the FESST@HH data set (https://doi.org/10.25592/UHHFDM.10172; Kirsch et al., 2021). A case study demonstrates that the network is capable of mapping the horizontal structure of the temperature signal inside a cold pool, and quantifying a cold pool's size and propagation velocity throughout its life cycle. Beyond its primary purpose, the data set offers new insights into the spatial and temporal characteristics of the nocturnal urban heat island and variations of turbulent temperature fluctuations associated with different urban and natural environments.

## SHORT SUMMARY

Conventional observation networks are too coarse to resolve the horizontal structure of km-scale atmospheric processes. We present the FESST@HH field experiment that took place in Hamburg (Germany) during summer 2020 and featured a dense network of 103 custom-built, low-cost weather stations. The data set is capable of providing new insights into the structure of convective cold pools and the nocturnal urban heat island, and variations of local temperature fluctuations.

## B.1 INTRODUCTION

We present the instrumentation and data set of the Field Experiment on Sub-mesoscale Spatio Temporal variability at Hanseatic city of Hamburg (FESST@HH) that illuminates the spatial and temporal structure of convective cold pools. Conventional mesoscale meteorological station networks have a typical resolution of $\sim 25\,\mathrm{km}$ in space and 10 min in time, and are essential in order to obtain a reliable picture of the atmospheric background state. Remote sensing techniques can help us to retrieve more finely resolved information for a few atmospheric variables like precipitation and wind speed. However, the spatial variability of basic meteorological parameters like air temperature or pressure on the sub-mesoscale (i.e., length scales between $\mathcal{O}(100)\,\mathrm{m}$ and $\mathcal{O}(10)\,\mathrm{km}$) remains under-resolved. Information on sub-mesoscale variability is especially important for the investigation and simulation of convective clouds and precipitation (Stevens et al., 2020). Convective cold pools are an important source of this variability and represent a blind spot for conventional observation networks. Therefore, cold pools are the main motivation for the FESST@HH experiment.

Cold pools play a prominent role in understanding the formation and life cycle of atmospheric convection. They are defined as areas of relatively cool and dense air that form through melting and evaporation of hydrometeors underneath precipitating clouds. Their horizontal size ranges from a few km to hundreds of km (Feng et al., 2015; Terai and Wood, 2013; Zuidema et al., 2017) and temperature decreases can exceed 10 K (Engerer et al., 2008, Study A). As the body of cold air grows and propagates horizontally away from the precipitation, it often causes a rapid decrease in local air temperature and the formation of a gust front. Secondary updrafts are preferentially triggered in the region ahead of the cold pool air due to the combination of mechanical lifting and accumulation of moisture in the lower troposphere (Drager et al., 2020; Feng et al., 2015; Tompkins, 2001; Torri et al., 2015). Cold pools are also found to support the organization of convective clouds and the transition from shallow to deep convection (e. g., Khairoutdinov and Randall, 2006; Kurowski et al., 2018; Rotunno et al., 1988; Schlemmer and Hohenegger, 2014). Since models with hectometer-scale resolution are required to realistically represent processes related to convection (Bryan et al., 2003; Grant and van den Heever, 2016; Hirt et al., 2020), large eddy simulations (LESs) have become an established tool to study cold pools. However, LES models critically depend on parametrizations of subgrid-scale phenomena such as turbulence and microphysics (Dawson et al., 2010; Li et al., 2015; Smagorinsky, 1963). This fact supports the need for observational data with a similar resolution to LES models that facilitate validation of simulations and enhance our understanding of sub-mesoscale processes.

Observational studies on cold pools draw upon a wide range of data collection methods. These include measurements from boundary layer towers (Goff, 1976, Study A), aircraft (Terai and Wood, 2013), ships (de Szoeke et al., 2017), precipitation radars (Borque et al., 2020), and combinations thereof (Feng et al., 2015; Mueller and Carbone, 1987). Nevertheless, capturing the horizontal structure of cold pools with the help of in situ observations is a challenging task given the small number of studies using, e. g., mesoscale station networks (Engerer et al., 2008; Markowski et al., 2002). In a recent study, van den Heever et al. (2021) described the use of uncrewed aerial systems, radiosondes and three closely-spaced surface stations during the $C^3$LOUD-Ex campaign to characterize the structure of convective updrafts and cold pools. The observations revealed that cold pool temperatures can exhibit variability on spatial scales between $\mathcal{O}(100)\,\mathrm{m}$ and $\mathcal{O}(1)\,\mathrm{km}$. However, given the small geographical extent of the in situ network, the experiment was unable to characterize

the complete surface temperature structure of any individual cold pool. There are also examples of more extensive observation networks at km-scale resolution like the Oklahoma City Micronet (Basara et al., 2011) and the WegenerNet (Kirchengast et al., 2014). However, with respect to areal coverage and instrument characteristics, these networks were mainly designed for climate monitoring rather than investigating short-lived convective-scale phenomena like cold pools.

The FESST@HH field experiment took place in Hamburg (Germany) from June to August 2020. The aim of the experiment was to perform meteorological observations that are suited to capturing the spatial structure of cold pools at the sub-mesoscale. This goal required the design of a ground-based station network that is large enough to cover the typical size of a cold pool ($\mathcal{O}(10)$ km) and dense enough to satisfy the desired resolution ($\mathcal{O}(100)$ m). Additionally, the measurement instruments had to be equipped with appropriate sensors for capturing cold pool fronts but still inexpensive enough to be deployed in large numbers. The relatively long measurement period was chosen to catch a reasonable number of cold pools during the convective season in Hamburg where around seven events per month are expected (Study A). In this article, we introduce the novel instruments and data set of FESST@HH, and demonstrate its potential for investigating the spatial structure and life cycle of cold pools based on a case study. Moreover, the experimental setup allows for the assessment of the spatial dimension of the nocturnal urban heat island and the variability of turbulent temperature fluctuations in different environments. A special feature of FESST@HH was the participation of a large number of volunteers that became necessary due to the COVID-19 pandemic.

## B.2 DESIGN OF INSTRUMENTS

The instrument design for the FESST@HH experiment was guided by the technical demands required to observe the sub-mesoscale structure of cold pools in space and time. Most importantly, the instruments had to be equipped with fast-response air temperature sensors that precisely capture relative changes in temperature. The sampling interval required was $\Delta t \leq 10$ s in order to track the propagation of cold pool fronts with a velocity of about $10\,\mathrm{m\,s^{-1}}$ (Borque et al., 2020) on scales of $\mathcal{O}(100)$ m. Moreover, the instruments had to be able to operate independently of external power for about two weeks given site location constraints. Based on these requirements, we designed and manufactured the Autonomous cold POoL LOgger (APOLLO) for operation during the FESST@HH experiment (section B.2.1). We complemented the network with Weather Transmitter (WXT) stations (section B.2.2) based on commercial sensors.

### B.2.1 *APOLLO stations*

The APOLLO is a simple and low-cost data logger that records air temperature and pressure. Inspired by the pyranometer network stations used during the HD(CP)$^2$ Observational Prototype Experiment (HOPE) campaign (Madhavan et al., 2016), it operates autonomously without an external power source, and its sensor and control units are mounted on a short mast (Figure B.1). The APOLLO is equipped with a fast-response and moisture-resistant thermometer consisting of a small ($7\,\mathrm{mm} \times 1.2\,\mathrm{mm}$) negative temperature coefficient (NTC) thermistor probe (type: TE Connectivity GA10K3MRBD1; Figure B.2a) placed inside a passively ventilated radiation shield (see sensor specifications in Table B.1). The control unit is based on a micro controller board (type: HIMALAYA Matrix-Core ESP32) located

inside a small (26 cm × 17 cm × 10 cm) logger box (Figure B.2b). A digital air pressure sensor (type: Bosch BME280 Environmental sensor) is installed on the logger main board, and a counterbalance valve ensures rapid adjustment of barometric pressure inside the logger box.

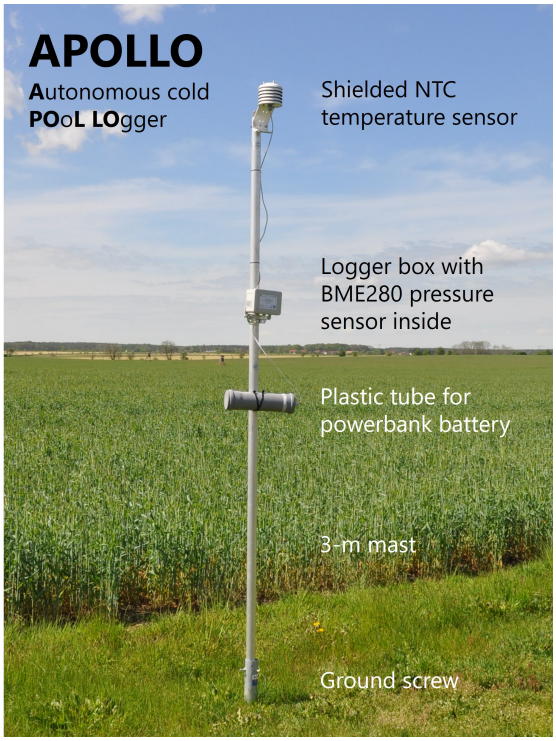


Figure B.1: Components of APOLLO station.

| PARAMETER | SENSOR | MEASUREMENT RANGE | ACCURACY |
|---|---|---|---|
| Temperature | NTC thermistor | -40. . . 100 °C | ±0.2 K at 0. . . 70 °C |
| Pressure | BME280 digital sensor | 300. . . 1100 hPa | ±1 hPa at 0. . . 30 °C (abs.)<br>±0.12 hPa at 25. . . 40 °C (rel.) |

Table B.1: Sensor specifications of APOLLO station (Bosch, 2020; TE Connectivity, 2015).

The readings of the temperature and pressure sensors are sampled with a resolution of 1 s and recorded onto a micro-SD memory card. An on-board GPS receiver is used to initially synchronize the internal real-time clock on start of the logger. To minimize power consumption during operation, the GPS module is activated to log the current time only once per hour for about 10 s which allows correction of the logger time stamp for drift in a post-processing step. The logger can establish a local WiFi hotspot for on-site control, data inspection and fast data access via download, and is able to send status messages via the LoRa (long-range) wireless communication protocol for live monitoring.

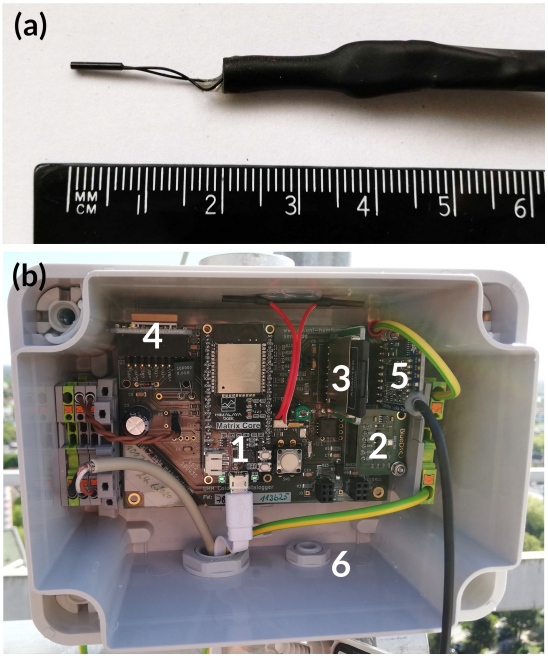


Figure B.2: (a) NTC thermometer with scale for reference and (b) logger main board of APOLLO station. Marked are the micro controller board (1), digital air pressure sensor BME280 (2), micro-SD memory card (3), GPS receiver module (4), long-range (LoRa) module (5) and pressure counterbalance valve (6).

The APOLLO is powered by a standard USB power bank battery (20 Ah capacity) that corresponds to an autonomous operation time of 10 to 14 d. For easy access during maintenance, the power bank is placed inside a separate plastic tube. All logger units are mounted on a 3 m mast that is anchored in the soil with a ground screw. In the standard configuration, the temperature sensor at the top of the mast and the pressure sensor inside the logger box are situated about 2.9 and 1.7 m above ground, respectively. The material costs for all required parts sum up to around EUR 300 per station.

The APOLLO station proves to be especially suited for accurately recording sharp thermal boundaries associated with cold pool front passages. In wind tunnel laboratory tests, the shielded NTC temperature sensor exhibits a response time (i.e., $e$-folding time constant) of $\tau = \{93, 14, 10\}\,\mathrm{s} \pm 10\,\%$ at $\{1, 3, 5\}\,\mathrm{m\,s^{-1}}$ wind speed when being artificially heated and released to room temperature. Since cold pools are usually associated with wind speed increases of $3\,\mathrm{m\,s^{-1}}$ and more (Study A), the lack of active sensor ventilation is unlikely to impact the accuracy of temperature measurements of cold pool passages. The comparison with an ultrasonic sensor confirms that the NTC thermometer captures well the rapid cooling signature of a cold pool event (Figure B.3). Although the response time of the APOLLO sensor is too large to respond to sub-second temperature fluctuations in the same way as the inertia-free ultrasonic sensor, it does not show any apparent lag in the minute-scale shape of the signal and even captures second-scale fluctuations. Moreover, trial field measurements of two cold pool events show that external site conditions, such as surrounding obstacles or different surface properties, do not systematically impact the strength and shape of a cold pool temperature signal (not shown) and, therefore, do not restrict the choice of measurement sites for APOLLO stations. Since this is not true for observations of wind speed and wind direction, these are only performed by the WXT

weather stations at appropriate locations. Similarly, humidity measurements are limited to the WXT stations to avoid the technical and financial effort needed to equip the APOLLO stations with precise sensors.

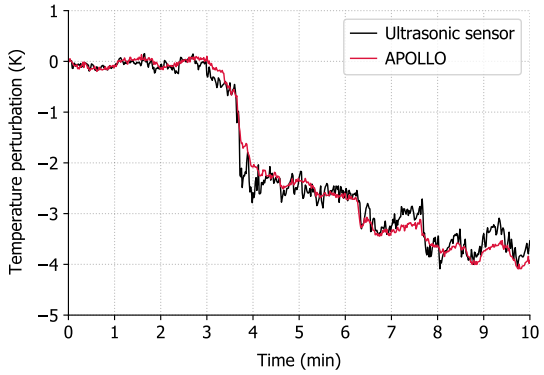


Figure B.3: Air temperature perturbation observed by a co-located ultrasonic sensor and APOLLO station during a cold pool event at the Meteorological Observatory Lindenberg – Richard Aßmann Observatory (eastern Germany) on 26 August 2019. The readings of the ultrasonic sensor are 1 s averages of 20-Hz acoustic temperature measurements by an ultrasonic anemometer (type: METEK uSonic-3 Scientific).

### B.2.2 *WXT weather stations*

WXT weather stations are employed to complement the APOLLO stations by providing information on other common meteorological parameters at selected locations. The main component of the station is a commercial compact multi-parameter sensor (type: Vaisala Weather Transmitter WXT536) that measures air pressure, temperature, relative humidity, wind speed, wind direction, and precipitation (see sensor specifications in Table B.2). Pressure, temperature, and relative humidity measurements are performed by a pressure–temperature–humidity (PTU) module inside a radiation shield that combines a capacitive silicon BAROCAP sensor (pressure), a capacitive ceramic THERMOCAP sensor (temperature) and a capacitive thin film polymer HUMICAP180 sensor (relative humidity). Wind speed and wind direction are detected by an WINDCAP ultrasonic anemometer on top of the radiation shield that consists of three equally-spaced ultrasonic transducers on a horizontal plane. The wind measurements are determined from the transit times of the ultrasound along the three paths with a sampling rate of 4 Hz and are internally averaged. Wind gusts are defined as the highest average wind speed of a 3 s interval which is internally updated every second. The precipitation measurement principle of the WXT536 sensor is based on a RAINCAP piezoelectrical sensor underneath a steel cover that detects the impacts of individual rain drops within a collecting area of 60 $cm^2$. Since the individual signals are proportional to the size of the rain drops, the sensor is able to derive the accumulated rainfall amount within the measurement interval. The sensor also distinguishes between impacts of rain drops and hail stones (Vaisala, 2017). Additionally, the WXT station is equipped with an external Pt1000 thermometer (type: TMH cable sensor Pt1000 1/3 DIN Klasse B; size: 40 mm × 3 mm) inside a separate radiation shield that allows for smaller response times of the measured temperature signal ($\tau = \{173, 55, 39\}$ s ± 10 % at $\{1, 3, 5\}$ $m\,s^{-1}$ wind speed) than the internal PTU module ($\tau = \{334, 213, 155\}$ s ± 10 % at $\{1, 3, 5\}$ $m\,s^{-1}$ wind speed).

The WXT data are sampled at 10 s resolution and written onto an SD memory card by a data logger (type: Avisaro M22766) that is synchronized with an integrated GPS module. Each station is powered by a 12 V lead battery. The battery is recharged by a solar panel (67 cm × 41 cm) so that the station can operate autonomously for several months depending on the available sunlight. Similar to the APOLLO design, the station components are mounted on a 3 m mast that is anchored in the soil with a ground screw (Figure B.4).

| PARAMETER | SENSOR | MEASUREMENT RANGE | ACCURACY |
|---|---|---|---|
| Temperature | PTU module | -52. . . 60 °C | ±0.3 K at 20 °C |
| | Pt1000 thermometer | -50. . . 85 °C | ±1.3 K at 20 °C |
| Pressure | PTU module | 500. . . 1100 hPa | ±0.5 hPa at 0. . . 30 °C |
| | | | ±1.0 hPa at -52. . . 60 °C |
| Rel. humidity | PTU module | 0. . . 100 %RH | ±3 %RH at 0. . . 90 %RH |
| | | | ±5 %RH at 90. . . 100 %RH |
| Wind speed | Ultrasonic anemometer | 0. . . 60 m s$^{-1}$ | ±3 % at 10 m s$^{-1}$ |
| Wind direction | Ultrasonic | 0. . . 360° | ±3° at 10 m s$^{-1}$ |
| | anemometer | 0. . . 360° | ±3° at 10 m s$^{-1}$ |
| Rainfall | Piezoelectrical sensor | - | better than 5 %, weather dependent |

Table B.2: Sensor specifications of WXT weather station (Vaisala, 2017).

Similar to the APOLLO stations, site conditions like surrounding obstacles and surface properties are not expected to have a systematic impact on cold pool signals in temperature, pressure, and humidity that are specific to the WXT sensors. However, wind speed and wind direction are heavily affected by nearby obstacles like buildings or vegetation due to the low installation height of 3 m above ground. Therefore, the individual site properties have to be taken into account when choosing a measurement location and interpreting the wind data of the WXT stations.

## B.3 DESCRIPTION OF EXPERIMENT

The FESST@HH measurement campaign took place under extraordinary circumstances. Its name is a modification of the acronym FESSTVaL (Field Experiment on Sub-mesoscale Spatio Temporal Variability in Lindenberg), a field campaign that was originally planned to take place at the Meteorological Observatory Lindenberg – Richard Aßmann Observatory (MOL-RAO) (eastern Germany) during summer 2020. Due to travel restrictions associated with the COVID-19 pandemic, the decision was made to postpone the FESSTVaL campaign to 2021 and to replicate the cold pool part of FESSTVaL in Hamburg under the name FESST@HH to make it compatible with pandemic-related regulations.

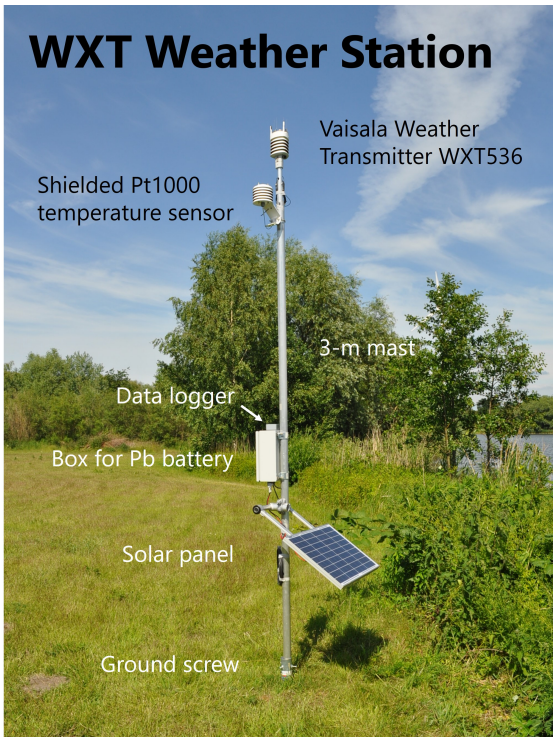


Figure B.4: Components of WXT weather station.

### B.3.1 *Experiment area*

Hamburg is the second largest city in Germany (population: 1.9 million; 2019) and is located in northern Germany (53.5°N, 10.0°E) about 80 km from the North Sea and the Baltic Sea. The FESST@HH measurement sites cover an area of 50 km × 35 km that includes the urban center of Hamburg and its rural surroundings (Figure B.5). The station network consists of 82 APOLLO sites (Table B.3) and 21 WXT sites (Table B.4) that are non-uniformly scattered over the domain with a generally higher station density closer to the city center. The arrangement of stations results from the location of private gardens and of public facilities like schoolyards that could be used as measurement sites (see section B.3.2). Moreover, the sites for WXT stations were chosen based on a small impact of surrounding obstacles on the local wind field and a roughly uniform distribution over the network. The average nearest-neighbor distance between all 103 measurement sites is 1.85 km with a standard deviation of 1.42 km, whereas it is 1.93±1.41 km and 5.49±1.98 km for APOLLO and WXT, respectively. The measurement area is crossed by the Elbe river in southeast–northwest direction and is characterized by relatively flat terrain. While the Elbe valley is situated around sea level, the elevation north and south of it does not exceed about 80 and 110 m, respectively. The altitudes of all measurement sites lie between 1 and 82 m above sea level with an average of 17 m.

To characterize the environmental properties of the measurement sites, we apply the local climate zone (LCZ) framework introduced by Stewart and Oke (2012). This framework classifies the impacts of surface structure, surface cover, and human activity on the local thermal climate with the help of 17 standardized LCZ classes. All 103 FESST@HH sites fall into 15 different LCZ classes, which also includes combinations of classes to describe the heterogeneity within about 500 m around the station (Bechtel et al., 2015). The majority of

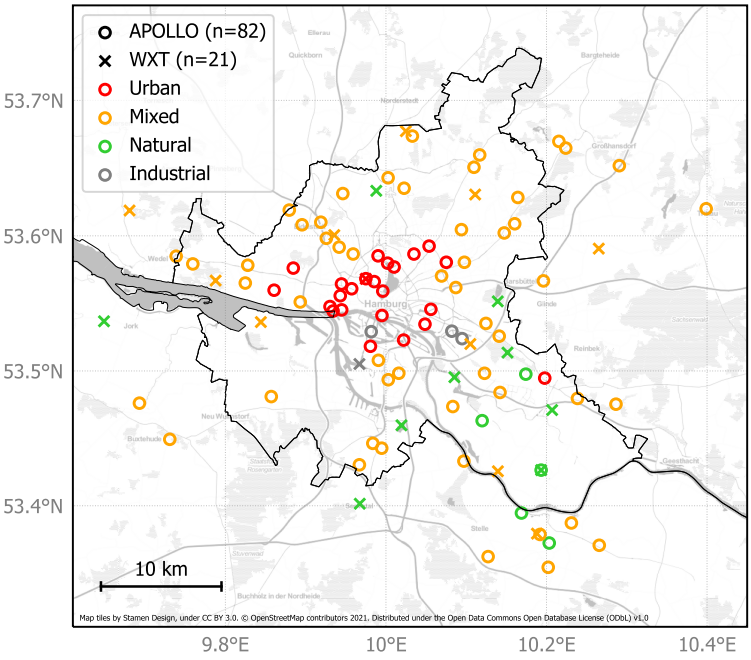


Figure B.5: Map of measurement locations of APOLLO and WXT weather stations during the FESST@HH 2020 experiment. Colors indicate environmental conditions of measurement sites grouped into urban (local climate zone (LCZ) 2, 4, or 5), mixed (LCZ 6), natural (LCZ 9, B, or D), and industrial (LCZ 8 or 10) following the framework of Stewart and Oke (2012). For stations falling into two LCZs, only the predominant sub-class is depicted. Black lines mark the city limits of Hamburg.

sites (61) are situated in an open arrangement of low-rise buildings and scattered trees (LCZ 6; *mixed* in Figure B.5), while 24 sites mostly near the city center are located in the proximity of mid-rise and high-rise buildings either in a compact or open arrangement (LCZ 2, 4, and 5; *urban*). Each of the other occurring classes contain less than 10 sites, which include natural environments (LCZ 9, A, B, and D) and industrial areas with mostly paved surfaces (LCZ 8 and 10). Ten sites are situated less than 50 m away from water bodies like the Elbe river, the Alster Lake, or channels (LCZ G).

### B.3.2 *Implementation*

The measurement period started on 1 June 2020 and ended on 31 August 2020, whereas the installation of all stations was completed in mid-June. The realization of the experiment was enabled by the support of many institutions and private landowners who provided permission at short notice to use their premises as measurement sites. The different groups of landowners are indicated by two-letter acronyms as part of a unique site identifier code that also contains the site number and the installed instrument type (a=APOLLO, w=WXT). The majority of measurement stations were installed in private gardens and backyards (PG; Figure B.6a) and on the grounds of various institutions and clubs (OG). Further groups of sites include existing weather stations and sites of the Meteorological Institute (WS and MI), air quality observation sites of the Free and Hanseatic City of Hamburg (LM), grounds of the University of Hamburg (UH), and schoolyards (KB). A special characteristic of the latter group is that most of the respective APOLLO logger components

| ID | NAME | LAT. (°N) | LON. (°E) | ALT. (M) | SENS. HEIGHT (M) | LCZ |
|---|---|---|---|---|---|---|
| 007WSa | Wetterstation Stellingen Wohngebiet | 53.59817 | 9.92575 | 21 | 3 | 6 |
| ... | ... | ... | ... | ... | ... | ... |
| 113PGa | Steinbeker Straße, Hamm | 53.54563 | 10.05597 | 6 | 7 | 5G |

Table B.3: Information about APOLLO measurement sites. Altitude denotes the height of ground above sea level, and the sensor height is the height of temperature sensor above ground. See Section B.3.1 for explanation of local climate zones (LCZs) after Stewart and Oke (2012). To maintain readability, 80 more rows are omitted. See original publication for full details.

| ID | NAME | LAT. (°N) | LON. (°E) | ALT. (M) | SENS. HEIGHT (M) | LCZ |
|---|---|---|---|---|---|---|
| 002MIw | Wettermast, Billwerder | 53.51996 | 10.10515 | 1 | 3 | 6D |
| ... | ... | ... | ... | ... | ... | ... |
| 114UHw | Geomatikum, Dachterasse 18. Stock | 53.56819 | 9.97483 | 16 | 72 | 4 |

Table B.4: As Table B.3, but for WXT measurement sites. To maintain readability, 19 more rows are omitted. See original publication for full details.

are mounted at existing weather stations used for educational purposes and, therefore, exhibit lower temperature sensor heights ($\sim$ 1.8 m) than the standard stations (Figure B.6b). Further deviations from the standard APOLLO installation include four loggers mounted on balconies (040UHa, 092PGa, 111OGa, and 113PGa; Figure B.6e) and two WXT stations installed on top of a container (017LMw; Figure B.6g) and on a roof-deck of the building of the Meteorological Institute (114UHw; Figure B.6h). Due to technical issues, minor changes to the instrumental setup had to be implemented during the measurement period with the replacement of one APOLLO (068OGa) and two WXT stations (048OGw and 114UHw) as well as the replacement of one APOLLO by a WXT station (083PGa).

Ensuring the implementation of FESST@HH was compatible with pandemic-related restrictions affected not only the selection of measurement sites but also the maintenance strategy. Instead of a small team servicing the entire network, the maintenance work was shared between nearly 40 people. Private landowners who provided measurement sites in their backyard could also volunteer to regularly change the battery, check the data, and upload it to an FTP server. Other stations located on public grounds, schoolyards, or industrial premises were serviced by colleagues living nearby. The main benefit of this maintenance strategy was that the collective effort kept the individual workload very low and promoted the continuous operation of the instruments, which eventually eased the execution of the experiment under challenging circumstances.

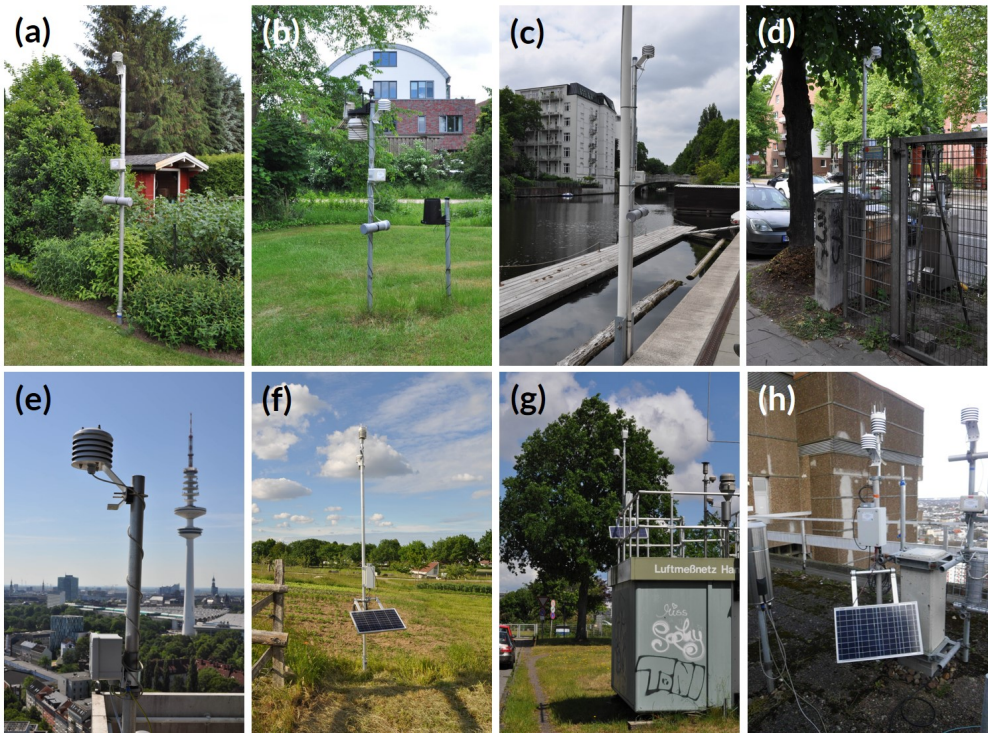


Figure B.6: Examples of instrument installations during FESST@HH: APOLLO station (a) as the standard installation in a private garden, (b) attached to an existing weather station on a schoolyard, (c) on a boat landing stage at a channel, (d) on an air quality observation site at a public road, (e) on the balcony of the building of the Meteorological Institute, and WXT weather station (f) as the standard installation on an agricultural field, (g) on top of a container, and (h) on the roof-deck of the building of the Meteorological Institute.

## B.4 DATA PROCESSING

The processing of the APOLLO and WXT station measurement data is a two-stage procedure. This study describes the published level 2 data format that contains quality-controlled data in a standardized format. In contrast, level 0 data are the raw data as directly produced by the instruments, and level 1 data are homogenized data for preliminary analyses but have not passed any quality checks.

### B.4.1 *Level 0 data*

The raw measurement data are stored in ASCII files. The APOLLO data logger creates a new file at the start time, which contains the internal logger time, the GPS-synchronized time, the resistance readings of the NTC thermometer, the pressure readings of the BME280 module, and status information at 1 Hz frequency. By contrast, new level 0 WXT data files are created at midnight (UTC) on a daily basis. Each line in the files consists of a GPS-synchronized time stamp and the measurement data of a specific sensor module, whereas each module sends data at 10 s intervals.

### B.4.2 *Level 1 data*

Measurement data which have passed the first processing step are called level 1 data. At this stage, basic standardization procedures are performed to allow for easy access to the data for preliminary analyses but not quality checks. Most importantly, this includes the correction and homogenization of the data time stamps. For the APOLLO data, the internal logger time is corrected with its deviation from the most recent valid GPS time stamp that is logged once per hour. Data for missing time steps are filled with placeholder values (NaN). Furthermore, daily files are created by splitting multi-day files and merging sub-daily files. In case of the WXT data, all time stamps are moved to a regular 10 s time grid. The measurement data itself are not manipulated, except for the APOLLO thermometer readings that are converted from resistance to temperature. For both station types, level 1 data are stored in a standard ASCII format.

### B.4.3 *Level 2 data*

The purpose of the second processing level is to generate a standardized and quality-controlled data product that is ready to use for scientific analyses. Since the raw APOLLO measurements contain different kinds of erroneous data which originate from technical issues of the logger or characteristics of the measurement site, we apply several quality checks and corrections to clean up the data. This processing step is not required for WXT data due to internal quality checks implemented by the manufacturer of the sensor. In total, less than 1 % of the level 1 data fail the quality criteria and need to be removed. The correction procedure contains the following steps:

- removing erroneous temperature and pressure data outside plausible limits defined by $0 \leq T \leq 40\,^{\circ}\mathrm{C}$ and $950 \leq p \leq 1050\,\mathrm{hPa}$, respectively;
- removing spikes in temperature (pressure) larger than $\Delta T = 0.5\,\mathrm{K}$ ($\Delta p = 1\,\mathrm{hPa}$), where $\Delta T$ ($\Delta p$) denotes the absolute difference from the 30 s (60 s) running median value. For the temperature data, spikes are only removed for phases of active WiFi connection which produces the spikes;
- removing temperature data showing implausibly large differences from the current network mean value defined as $|T - \overline{T}| > 15\,\mathrm{K}$. For three stations (037UHa, 040UHa, 068OGa) with erroneous NTC temperature sensors producing unphysical spikes, a criterion of $|T - \overline{T}| > 2$ K is applied, and all data within a time window of 15 min before and after erroneous data are also removed;
- manually removing single periods of erroneous temperature and pressure measurements that are not filtered by the previous criteria. In case of station 039UHa, temperature measurements on more than 40 d are affected by the warm air outlet of a nearby air-conditioning facility and are manually removed;
- applying a 10 s running mean smoothing procedure on the temperature measurements of station 113PGa to account for an anomalously high noise level of the NTC sensor; and
- correcting the individual biases of NTC temperature sensors. The biases are determined from one-week-long calibrations with respect to a reference WXT sensor (114UHw) between January and June 2020. The pressure readings of the BME280

sensors are not calibrated since test measurements of the absolute values showed an oscillating drift pattern with an amplitude and period of about 0.5 hPa and 10 d, respectively. The WXT536 and Pt1000 sensors are calibrated by the manufacturer.

The level 2 data (Kirsch et al., 2021) are stored in the NetCDF4 data format (Eaton et al., 2017) while the naming of files, variables, and attributes complies with the SAMD (Standardized Atmospheric Measurement Data) product standard (Lammert et al., 2018). Accordingly, all measurement data of the same variable and from the same type of instrument are merged and stored in daily files. Note that the time variable expressed as seconds since 1 January 1970, 00:00:00 UTC ignores leap seconds (i.e., occasional adjustments of UTC time to variations in Earth's rotation velocity). Also note that the time drift correction and quality control procedures cause irregular and isolated data gaps that may affect only single seconds which has to be taken into account when using the data set at its full time resolution. The file header contains all relevant metadata describing the individual measurement sites, namely, the station identifier, the station name, the geographic coordinates, the altitude above sea level, the sensor height above ground, and the LCZ. Attached to the data set are also images of all measurement stations and panoramic views of the surroundings of all WXT stations to support the interpretation of the corresponding observation data.

## B.5 DESCRIPTION OF DATA SET

### B.5.1 *Data availability*

The level 2 data set of FESST@HH covers the period from 1 June to 31 August 2020 (Figure B.7a). The average availability of valid temperature observations is 83.2 % and 87.6 % for all APOLLO and WXT stations, respectively. Since the three-month period also includes the installation phase of the instruments during the first half of June, these numbers increase to 90.0 % and 94.3 % if only the period after 15 June is considered. During this period, the daily availability of APOLLO and WXT measurements is always larger than 82.6 % and 90.0 %, respectively. Apart from the removed measurements affected by erroneous sensors and local site conditions, most of the data gaps in the APOLLO data are due to missing power supply of the loggers, either caused by technical issues related to the power bank batteries or insufficient maintenance. In only one case was a battery stolen. The greater stability of the WXT power supply is also the reason for the generally greater availability of WXT data compared to APOLLO data.

### B.5.2 *Weather conditions*

The weather conditions during the FESST@HH period covered the full range of a typical mid-latitude summer. The air temperature measured by the station network ranges between a minimum of 5.3 °C on 13 July and a maximum of 35.6 °C on 8 August (Figure B.7b; days defined in UTC). During the entire 92 d period, the maximum temperature exceeded 25 °C on 41 d and 30 °C on 16 d, including an exceptionally long period of 12 consecutive days with maximum daily temperature exceeding 30 °C between 6 August and 17 August. In contrast, July was characterized by relatively cold temperatures with a maximum of above 25 °C on only 6 d. Measurable rainfall, defined as a daily rainfall accumulation of more than 1 mm at at least one WXT station of the network, was observed on approximately half of the days from 1 June to 31 August (Figure B.7c). On 11 d, mostly between 27 June and

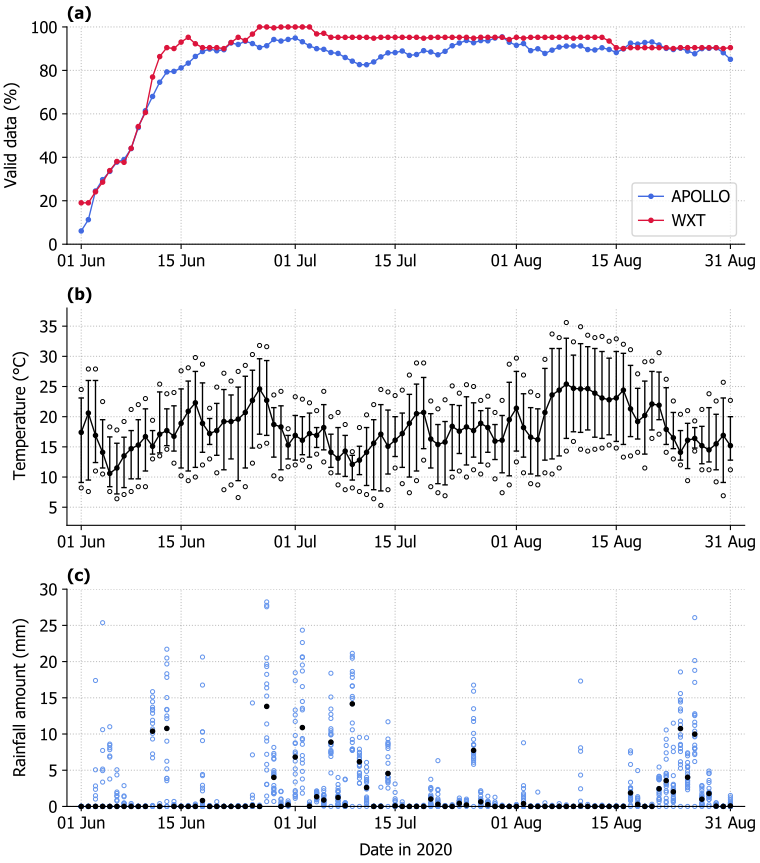


Figure B.7: FESST@HH level 2 data from 1 June to 31 August 2020: (a) daily mean fraction of valid temperature observations over all APOLLO and WXT stations; (b) daily median (filled dots), 5th percentile and 95th percentile (whiskers), and minimum and maximum (open circles) of all WXT air temperature observations; and (c) individual accumulated rainfall amount at all WXT stations (open circles). Filled dots mark the daily median. Days are defined in UTC.

10 July, the median rainfall amount exceeded 5 mm. A maximum daily accumulation of 28.2 mm was observed on 27 June in association with a strong convective event.

## B.6 OBSERVATIONS OF SUB-MESOSCALE PHENOMENA

The goal of the FESST@HH experiment was to design and operate an observation network that is dense enough to investigate the structure of convective cold pools. However, the data set also contains information and potential scientific implications for additional sub-mesoscale phenomena that we present here.

### B.6.1 *Cold pools*

During the three-month measurement period, the station network recorded 37 cold pool events. We define events as periods with at least five stations per hour satisfying the cold pool detection criterion described in Study A, i.e., a local temperature drop of at least 2 K within 20 min. This rather conservative threshold was chosen to robustly

discriminate the cold pool signals from other potential sources of spatial temperature variability. The plausibility of cold pool detections is checked based on the visual inspection of corresponding rain radar imagery by an X-band radar of the University of Hamburg (Burgemeister et al., 2022a) and the operational C-band radar network of the German Weather Service. The number of approximately 12 events per month is larger than the long-term average at the Weather Mast Hamburg (WMH) site (Bruemmer et al., 2012) of about seven events per month (Study A) as expected from the larger areal coverage compared to a point measurement. Figure B.8 shows an overview of all 37 identified cold pool events and illustrates the spatial variability of maximum temperature perturbations detected within the station network. Most of the events (28) exhibit a median temperature signal of -4 K or weaker, however, the variability in signal strength and number of affected stations largely vary for different events. To demonstrate the ability of the station network 7 to capture the characteristics of an individual cold pool and to shed light on its internal structure, we present one case study.

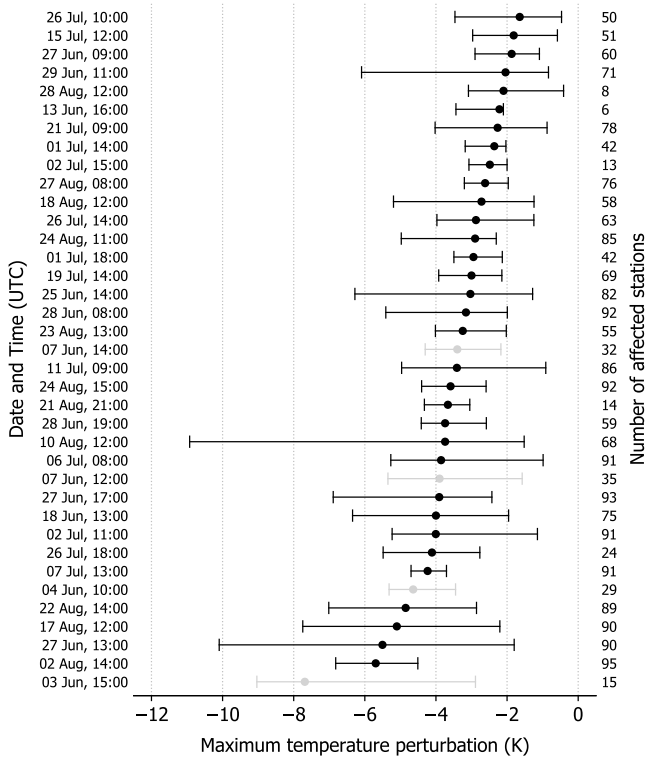


Figure B.8: Distribution of the maximum temperature perturbation detected at individual APOLLO and APOLLO stations for the 37 identified cold pool events during FESST@HH. Blacks dots and whiskers mark the median value and 5th/95th percentiles, respectively. The events are sorted according to the median values in maximum temperature perturbation. Events with an average data availability over all stations of less than 75 % are marked in gray. The times specify the defined begin of the respective events about 30 to 60 min prior to the onset of rainfall whereas the duration of an event is 4 h. Indicated is also the number of stations that have experienced a cold pool passage.

On 10 August 2020 around 12:45 UTC, a strong and nearly stationary convective precipitation cell developed southeast of the city center. About 10 min later, the formation of a cold pool became evident from a rapid cooling of the surface-layer air. Figure B.9

illustrates the evolution of the cold pool with snapshots of the temperature perturbations relative to the pre-event state observed by the station network. About 20 min after initiation of the convective cell, the cold pool exhibited a temperature perturbation of up to -8 K within an area of less than 10 km in diameter (Figure B.9a). After another 20 min, the temperature perturbation strengthened to about -11 K and the cold pool expanded to a size of roughly 10 km × 20 km (Figure B.9b). This process continued until around 14:00 UTC when the cold pool reached its maximum temperature perturbation of about -12 K and a diameter of nearly 30 km when assuming a roughly elliptical shape of the cold pool, whereas its northeastern parts were outside of the network (Figure B.9d). The associated near-surface wind field observed by the WXT weather stations indicated a strong divergent flow at the cold pool center especially during the early stages of the cold pool's life cycle (Figure B.9a and b). Consistent with expected characteristics of a cold pool, the radial expansion of the cold-air region during the later stages was also present in the wind observations predominantly southwest of the cold pool center (Figure B.9c and d).

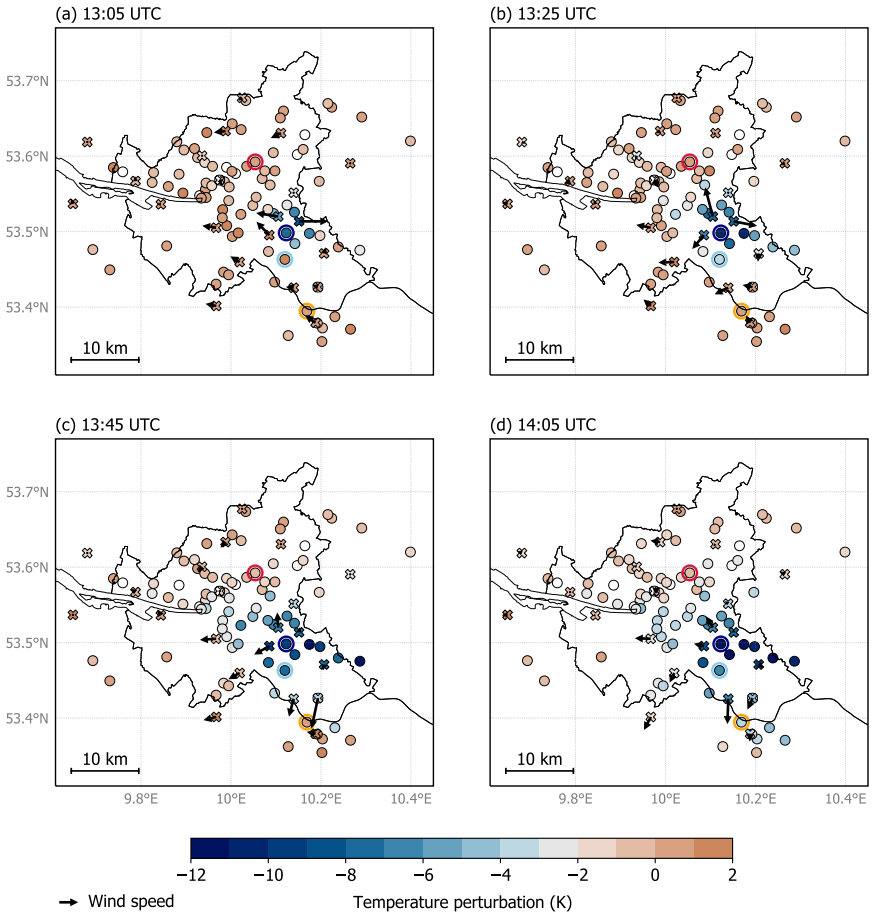


Figure B.9: Perturbation in air temperature since 12:30 UTC from (a) 13:05 UTC to (d) 14:05 UTC observed by APOLLO (circles) and WXT stations (crosses) during a cold pool event on 10 August 2020. Bluish colors mark stations inside the cold pool defined by a temperature perturbation stronger than -2 K (color map by Crameri (2018) and Crameri et al. (2020)). Black arrows indicate instantaneous wind speed and direction observed by WXT stations. The length of the reference arrow corresponds to 5 m s$^{-1}$ wind speed. The four highlighted stations refer to the respective data illustrated in Figure B.10.

The time series of temperature measurements at selected stations of the network provide further insights into the spatial structure and life cycle of the cold pool (Figure B.10a). APOLLO station *Luxweg* (104PGa) near the cold pool center experienced an initial temperature drop of approximately 8 K within 5 min, that continued at a slower rate afterwards and reached a maximum perturbation of -12 K after 1 h. This value is on the order of strongest temperature perturbations expected during cold pool passages in Hamburg (Study A). The readings of the stations *Ochsenwerder Norderdeich* (082PGa) and *Obsthof Lehmbeck* (054OGa), located 4 km and 12 km further south, respectively, reveal that the maximum amount of cooling decreases by about two-thirds away from the center, which suggests a highly heterogeneous temperature structure inside the cold pool. Since the site *Luftmessnetz Habichtstraße* (018LMa), situated northwest of the cold pool center, experienced no cooling at all, the cold pool produced a gradient in temperature perturbation of 12 K within a distance of 11 km. This result is in line with the findings of van den Heever et al. (2021), who reports a variation of near-surface cold pool temperature perturbations of order 1 to 2 K on scales between $\mathcal{O}(100)$ m and $\mathcal{O}(1)$ km. The time lags between the cooling signals observed on the southern side of the cold pool also allow us to estimate its propagation velocity. Based on time lags of about 15 min and 50 min for travel distances of 3.9 km (104PGa–082PGa) and 11.9 km (104PGa–054PGa), respectively, the velocity is about 4 m s$^{-1}$. This value is lower than the propagation velocity of 6.7 m s$^{-1}$ found for a cold pool event in north-central Oklahoma (Borque et al., 2020), but is plausible considering that the parent precipitation cell was almost stationary and, therefore, the observed propagation of the cold outflow air was not biased by the movement of the cell itself.

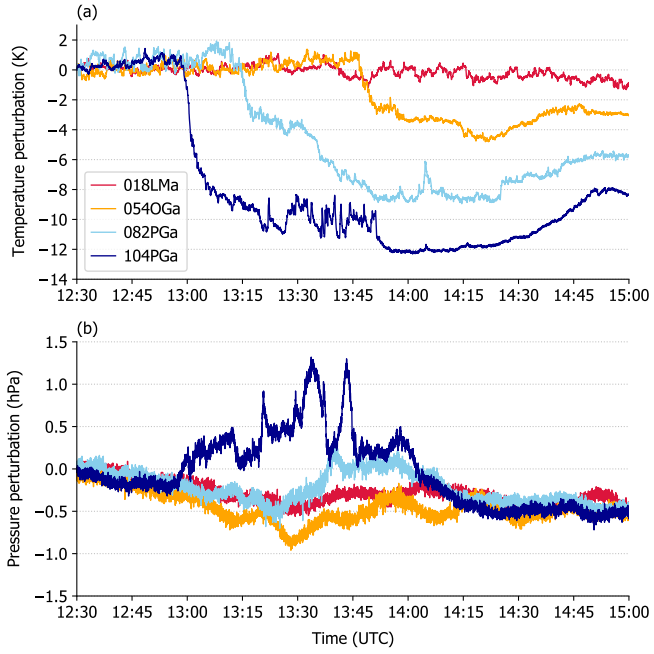


Figure B.10: Perturbation in (a) air temperature and (b) pressure since 12:30 UTC observed by the four selected APOLLO stations *Luftmessnetz Habichtstraße* (018LMa), *Obsthof Lehmbeck* (054OGa), *Ochsenwerder Norderdeich* (082PGa), and *Luxweg* (104PGa) during a cold pool event on 10 August 2020. Locations of the stations are highlighted in Figure B.9.

The accompanying air pressure measurements at the four selected sites confirm that the negative temperature perturbation of the cold pool is associated with a typical hy-

drostatic pressure rise (Figure B.10b). However, the positive pressure perturbation was well-pronounced only at station 104PGa, while the amplitudes were not proportional to the strength of the corresponding cooling signals. The pressure signal at station 104PGa also experienced rapid fluctuations of about 1 hPa that were not apparent at the three other sites. Although an in-depth investigation of such effects lies beyond the scope of this study, this may indicate that the spatial structure of a cold pool differs between temperature and pressure and that mechanisms other than hydrostatic cooling control the pressure signal near the center, like dynamic effects already described in early studies (i.e., Mueller and Carbone, 1987; Wakimoto, 1982).

### B.6.2 *Urban heat island*

The FESST@HH data set is well suited for studying urban climate effects as the station network covers both the city center and its rural surroundings. Stations near the city center record weather conditions with urban modifications whereas rural stations provide undisturbed references. Focusing on air temperature, we define the urban modification $\Delta T_{\text{city}}$ as the difference between the locally observed air temperature and the undisturbed, natural temperature $T_{\text{nat}}$ determined exclusively by large-scale weather conditions. On scales of $\mathcal{O}(10)$ km without orography, it is reasonable to assume that $T_{\text{nat}}$ varies only linearly in space. We estimate the mean and the slope of this linear temperature field with a regression using all stations in weakly sealed (i.e., mostly natural) environments defined by a maximum sealing up to *open low-rise* (LCZ 6). The mean diurnal cycle of $\Delta T_{\text{city}}$ features a step function at almost all stations (Figure B.11a). During daytime, the urban effects are small and $\Delta T_{\text{city}}$ is close to zero everywhere. In contrast, during nighttime, predominantly between 21 and 3 UTC, $\Delta T_{\text{city}}$ reaches a constant level at all stations, which largely reflects the well-known nocturnal urban heat island effect. For example, the most central station *Wetterstation HafenCity* (010WSa; orange in Figure B.11a) is almost 2.5 K warmer than estimated $T_{\text{nat}}$ and the most rural site *Obsthof Schuback* (055OGw) is even 1.5 K colder than the reference. The spatial pattern of the mean nocturnal urban heat excess is in agreement with the typical heat island structure featuring largest values close to the city center (Figure B.11b). Further analysis of individual days (not shown) provides indication that the advection of the heat island effect causes downwind heat plumes to form which affect specific outskirts depending on the prevailing wind direction.

### B.6.3 *Turbulent temperature fluctuations*

The NTC temperature sensor of the APOLLO station responds rapidly to air temperature fluctuations. The recorded time series with a sampling rate of 1 Hz partly resolves temperature eddies related to turbulent sensible heat fluxes. The high frequency temperature fluctuation expressed by the standard deviation of temperature readings within 1 min intervals, $\sigma_{\text{T}}$, features a well-pronounced diurnal cycle (Figure B.12a). During nighttime, $\sigma_{\text{T}}$ is close to 0.05 K at all stations, which most likely resembles the noise level of the instruments. However, at daytime, $\sigma_{\text{T}}$ is well above that noise level and follows the common diurnal cycle of net radiation or sensible heat flux at the surface. Turbulent fluxes are strongly determined by local surface conditions like albedo, sealing, or vegetation cover. Likewise, the differences in the diurnal cycle of $\sigma_{\text{T}}$ can be explained by local surface conditions: the station *Stadtteilschule Blankenese* (033KBa) at a schoolyard next to a sports ground (low albedo, no evapotranspiration) with free insolation exhibits the highest

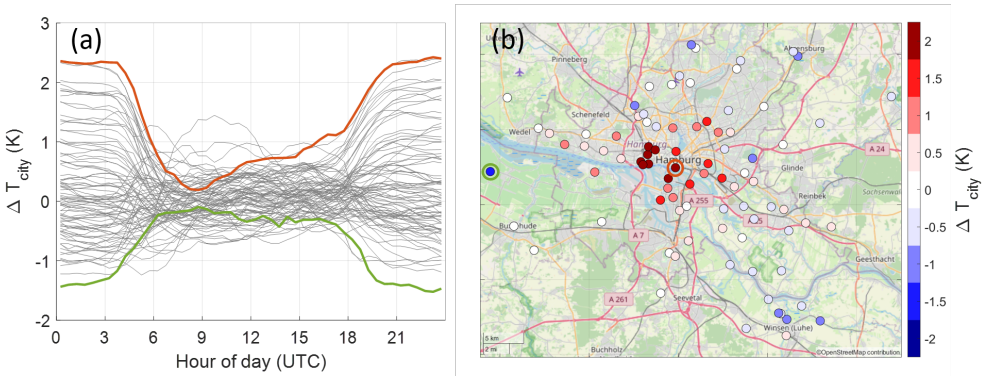


Figure B.11: (a) Mean diurnal cycle of urban temperature modification $\Delta T_{\text{city}}$ and (b) nighttime (21:00 UTC to 03:00 UTC) mean of $\Delta T_{\text{city}}$ at all APOLLO and WXT stations from 15 June to 31 August 2020. Highlighted in orange and green are the urban station *Wetterstation HafenCity* (010WSa) and the rural station *Obsthof Schuback* (055OGw), respectively. © OpenStreetMap contributors 2021. Distributed under the Open Data Commons Open Database License (ODbL) v1.0.

temperature variability. High values also occur at the schoolyard of station *Schule Redder* (036KBa) but are shifted and limited to morning hours due to a building west of the station casting a shadow and reflecting sunlight. Even more extreme, buildings shade the station *Luftmessnetz Rothenburgsort* (020LMa) almost the whole day except during the late afternoon. The lowest temperature variance is observed at station *Uni Sternwarte* (043UHa), the only station below tall trees. The heat exchange within the tree canopy effectively reduces the energy exchange at the ground.

The relation between surface heat exchange and temperature variability is also directly confirmed by correlating the net radiation observed at the WMH reference site with $\sigma_T$ at the neighboring APOLLO station *Wetterstation Zollamt* (011WSa) located about 750 m away (Figure B.12b). Values of $\sigma_T$ lower than 0.75 K are strongly correlated to situations where the net radiation is close to zero. Increasing variance beyond this threshold is mostly explained by increasing net radiation ($r^2 = 0.77$). Instead of the sensible heat flux, we use the net radiation for this analysis to minimize the influence of land surface differences between the two sites (pasture at *Wetterstation Zollamt* versus sealed area at WMH). Additional measurements on a test site show that $\sigma_T$ does not change if the sensor shield is protected from direct solar radiation (not shown). This finding supports our reasoning that the APOLLO stations capture turbulent temperature fluctuations caused by the surface heat exchange in the near environment of the observation site rather than artificially generated by the heating of the sensor shield. Direct measurements of turbulent heat fluxes and surface properties like temperature and moisture added in the FESSTVaL follow-up experiment will help to better understand the land–atmosphere interactions for different land classes.

### DATA AVAILABILITY

The data set is available for download at https://doi.org/10.25592/UHHFDM.10172 (Kirsch et al., 2021). The data are stored in netCDF files per station type, measurement variable, and day. The file size is about 25 MB and 1.5 MB for APOLLO and WXT data, respectively. For both station types, all daily files are merged into monthly *.zip files. The data set also

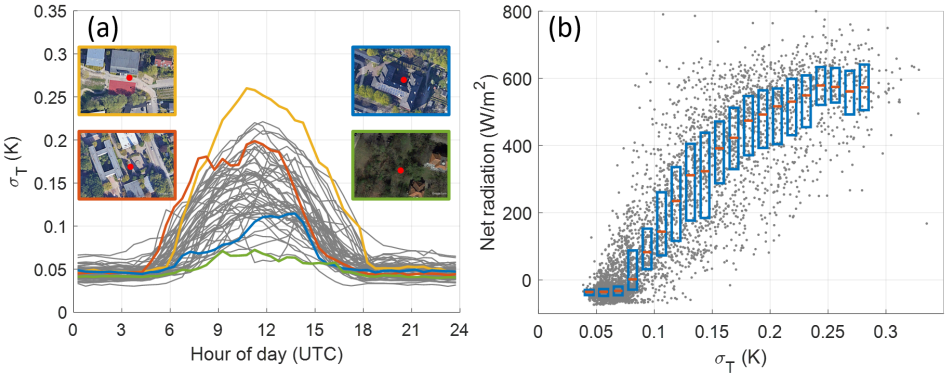


Figure B.12: (a) Mean diurnal cycle of standard deviation of 1 min temperature fluctuations $\sigma_T$ at all APOLLO stations (gray lines) and at the highlighted stations *Stadtteilschule Blankenese* (yellow; 033KBa), *Schule Redder* (orange; 036KBa), *Luftmessnetz Rothenburgsort* (blue; 020LMa) and *Uni Sternwarte* (green; 043UHa). Map data © Google Earth 2021. (b) Net radiation at the Weather Mast Hamburg (WMH) site dependent on $\sigma_T$ at station *Wetterstation Zollamt* both averaged over 10 min. Blue boxes and orange bars indicate the interquartile range and median for the respective $\sigma_T$ bin. The analyses in both (a) and (b) are valid for sunny days from 1 June to 31 August 2020, whereas sunny days are defined as days on which the daily averaged global radiation at WMH is larger than at least one-third of the daily averaged theoretical maximum of clear-sky insolation.

includes a file containing images of all measurement stations and panoramic views of the surroundings of all WXT stations.

## B.7 SUMMARY AND CONCLUSIONS

The FESST@HH field experiment took place in Hamburg (Germany) from June to August 2020 with the primary aim of illuminating the internal structure of convective cold pools that conventional observations miss. To this end, a dense network of 103 autonomously operating weather stations was installed over an area of 50 km × 35 km with an average distance between the stations of 1.85km. The measurements were mainly conducted by 82 low-cost, custom-built APOLLO stations that were designed to sample the strong and rapid changes in air temperature and pressure associated with cold pools at 1 s resolution. Additional measurements of relative humidity, wind speed, and precipitation at 10 s resolution were performed by 21 WXT weather stations based on commercial sensors.

The FESST@HH data set is unique not only with respect to its scientific potential for investigating sub-mesoscale atmospheric processes but also with respect to its implementation. The experiment was successfully conducted despite the exceptional circumstances caused by the COVID-19 pandemic, especially thanks to the short-notice support of local institutions and private landowners who provided their grounds as measurement sites and helped with the station maintenance. The low-cost and self-manufactured measurement instruments operated smoothly without any major technical problems although they had never been used in such a large number before. The good performance is reflected by an availability of quality-controlled data of more than 90 % during the main observation period. Most importantly, a case study demonstrates that the network is capable of mapping the sharp horizontal temperature gradients produced by a convective cold pool and capturing its spatial footprint. Throughout its life cycle, the cold pool diameter grows from

less than 10 km to nearly 30 km, while its leading edge propagates at a velocity of about $4\,\mathrm{m\,s^{-1}}$ away from the center of convection. There is also evidence that the spatial variance of the corresponding pressure signals differs from the cooling signature and may indicate the presence of non-hydrostatic effects acting within the cold pool center. Furthermore, the data set is relevant for studies in urban meteorology, as the dense temperature observations include information on the spatial structure of the nocturnal urban heat island and on the local surface heat exchange mirrored by high-frequency temperature fluctuations.

The FESST@HH field experiment proves that it is possible to conduct observations that close the information gap left by conventional measurement networks. In addition, it highlights the real need for dense station networks that act like a magnifying glass for revealing sub-mesoscale atmospheric processes. The use of a large number of low-cost instruments designed for a specific purpose is a feasible strategy to tailor a measurement network that is dense enough to shed light on previously unobserved scales. These data are scientifically valuable not only for a deeper understanding of cold pools and the convective life cycle but also for the validation of hectometer-scale numerical simulations. Moreover, the data set leaves space for unexpected results and applications not yet anticipated. FESST@HH also exemplifies how a major community effort can ease the execution of a major scientific enterprise or, as in this case, make it possible at all. In this sense, FESST@HH has the potential to be a prototype for future field campaigns. It already provides a proof of concept for an extended investigation of cold pools and further sub-mesoscale boundary layer structures during the FESSTVaL 2021 experiment.

## COMPETING INTERESTS

The authors declare that they have no conflicts of interests.

## DISCLAIMER

Publisher's note: Copernicus Publications remains neutral with regard to jurisdictional claims in published maps and institutional affiliations.

## ACKNOWLEDGMENTS

The authors are grateful to Marco Clemens and Ingo Lange for heavily supporting the manufacturing, installation and maintenance of measurement stations, and to Sarah Wiesner for planning and coordinating the field experiment. We thank Theresa Szyszka and Jan Moritz Witt for assembling the APOLLO logger main boards, manufacturing the components of the APOLLO and WXT stations, and supporting their maintenance. For either helping with the installation and maintenance of stations or providing ground for measurement sites we are thankful to Sigrid and Werner Bock, Agnes Bornholdt, Frank Böttcher, Burghardt Brümmer, Stefan Bühler, Finn Burgemeister, Guido Cioni, Martin Claussen, Traute Crüger, Henning Dorff, Tobias Finn, Veronika Gayler, David Grawe, Akio Hansen, Anja Hermans, Tatiana Ilyina, Olaf Jäke, Markus Kilian, Stefan Kinne, Marlene and Reinhard Kirsch, Brita Kliemt, Hartmut Kock, Heike Konow, Sascha Krueck, Heiner Meier, Ulrike Niemeier and Luis Kornblueh, Peter Peitzner, Jon Petersen, Thomas Raddatz, Jule Radtke, Berinike Rappat, Florian Römer, Nicole and Steffen Rüeß, Rita Schierholz, Imke Schirmacher, Hauke Schmidt, Amelie Schmitt, Hauke Schulz, Constanze Seibert, Milica Stankovic, Claudia Timmreck and Hannes Thiemann, Karla Tomhawe, Bodo Voigt, Stefan Walter, Ralf Wede-

mann, Tobias Weiß, Susanne and Heinz-Dieter Wenck, Benjamin Will, Holger Witt, and Florian Ziemen. We acknowledge the following institutions, schools, clubs and companies for allowing us to install measurement stations on their grounds: Hamburger Luftmessnetz, Universität Hamburg, Bundesanstalt für Wasserbau Hamburg, Deutscher Wetterdienst Niederlassung Hamburg, Drachenfreunde Winsen, Greenpeace Wilhelmsburg, Gut Karlshöhe, Gymnasium Rahlstedt, Halepaghen-Schule Buxtehude, Hamburger Aero-Club Boberg, Hamburger Bogenschützen Gilde, Hansa Sportverein Stöckte, Hochschule für Angewandte Wissenschaften Hamburg, Immanuel-Kant-Gymnasium Harburg, Obsthof Axel Schuback, Obsthof Lehmbeck, Overmeyer Landbaukultur, Restaurant Bobby Reich, Restaurant Fährhaus Tatenberg, Schule Redder Sasel, Segelclub Rhe Hamburg, Segelvereinigung Sinstorf, Stadtteilschule Blankenese, Stadtteilschule Eidelstedt, Stadtteilschule Meiendorf, Suntrace, Tennisclub Eichtalpark, and TSV Holm. We also thank all persons and institutions that supported the experiment in any way and were not explicitly mentioned here.

This research was carried out in the Hans Ertel Center for Weather Research (Hans-Ertel-Zentrum für Wetterforschung; HErZ). This German research network of universities, research institutions, and the German Weather Service (Deutscher Wetterdienst; DWD) is funded by the Federal Ministry of Transport and Digital Infrastructure (Bundesministerium für Verkehr und digitale Infrastruktur; BMVI).

The authors are thankful to Annika Jahnke-Bornemann and the Integrated Climate Data Center (ICDC) for the smooth data publication and curation.

Bastian Kirsch is thankful to Jochem Marotzke and Dallas Murphy for providing valuable tips on the writing style and structure of the manuscript, and to Arjun Kumar for proofreading.

The authors thank Aryeh Jacob Drager and one anonymous referee for carefully reviewing the manuscript and for their detailed and constructive comments.

## FINANCIAL SUPPORT

This research has been supported by the Bundesministerium für Verkehr und Digitale Infrastruktur (grant no. 4818DWDP1B).

## REVIEW STATEMENT

This paper was edited by David Carlson and reviewed by Aryeh Drager and one anonymous referee.

# C

# THE MORPHOLOGY AND GROWTH OF CONVECTIVE COLD POOLS IN A DENSE STATION NETWORK

The work in this appendix is a manuscript in preparation for publication as

**Kirsch, Bastian**, Cathy Hohenegger, and Felix Ament (2022). "The morphology and growth of convective cold pools in a dense station network." *in preparation*.

## AUTHOR CONTRIBUTIONS

**BK** helped to install and operate the instruments, compiled the meta data, processed the measurement data, developed the methodology, performed the formal analysis, and wrote the original draft. CH conceptualized the idea for the experiment, helped to develop the methodology, supervised the project, and did the project administration. FA conceptualized the idea for the experiment, helped to operate the instruments, helped to develop the methodology, and supervised the project.

# The morphology and growth of convective cold pools in a dense station network

BASTIAN KIRSCH[1,3], CATHY HOHENEGGER[2,3], and FELIX AMENT[1,2,3]

[1]*Meteorological Institute, University of Hamburg, Hamburg, Germany*
[2]*Max Planck Institute for Meteorology, Hamburg, Germany*
[3]*Hans Ertel Centre for Weather Research, Branch Model Development - Convection, Hamburg, Germany*

ABSTRACT

Direct observational evidence on the size, shape, and structure of convective cold pools is obscured by insufficient resolution of existing measurement systems. The Field Experiment on Sub-mesoscale Spatio Temporal Variability in Lindenberg (FESSTVaL) aimed to perform sub-mesoscale ($\mathcal{O}(100)$ m – $\mathcal{O}(10)$ km) observations that help to sharpen our notion of the morphology of cold pools, i. e., their size, shape, and structure, and the factors that control their growth. The experiment was held at the Meteorological Observatory Lindenberg – Richard Aßmann Observatory (MOL-RAO) south-east of Berlin (Germany) and featured a dense network of 99 custom-built, low-cost measurement stations covering a circular area of 30 km in diameter situated in a rural environment. During the experiment period from 17 May to 27 August 2021, the station network sampled 42 cold pool events. The morphological properties of cold pools are determined by spatially interpolating the temperature observations to a regular grid via kriging and defining individual objects of temperature perturbation stronger than -2 K. For the analysis, cold pool objects that touch the boundary of the network by more than 25 % are ignored. The remaining sample of 1278 objects analyzed at 1-min intervals has a median equivalent diameter of 8.4 km and median strength of -2.3 K. Large cold pools are significantly stronger than small ones and vice versa. The sampled cold pools are not circularly shaped independently of their size and strength, exhibiting aspect ratios between 1.5 and 1.6. Moreover, the temperature structure within cold pools is more heterogeneous if they are large or strong. The analysis of four selected events reveals that cold pools grow linearly with the accumulated rainfall amount observed by an X-band rain radar and cool most efficiently early in their life cycle. Theoretical considerations and observations from radiosonde profiles indicate that the height of cold pools outside of raining areas is approximately constant in time. These results suggests that the growth of cold pools is similar to the expansion of an idealized density current. This process is driven by precipitation, both directly by evaporation in under-saturated sub-cloud layer air and indirectly by import of upper-level air through downdrafts.

## C.1 INTRODUCTION

This study presents the first characterization of the morphology of convective cold pools, i. e., their size, shape, and structure, based on in situ observations of a dense station network and discusses factors that control their growth. Cold pools are mesoscale bodies of cool and negatively buoyant outflow air that form by evaporation of precipitation and horizontally propagate on the Earth's surface. The significance of cold pools for atmospheric convection is a long-standing topic in literature, be it for the strength and longevity of convective squall lines (Rotunno et al., 1988), the organization of tropical deep convection (Tompkins,

2001), or the transition from shallow to deep convection (Khairoutdinov and Randall, 2006). In the recent decade, the role of cold pools in organizing convection has attained increased interest due to evolving computational resources that allow large-domain convection-permitting simulations at hectometer-scale. The most relevant processes in this context are the initiation of secondary convection by thermodynamical and dynamical forcing (Feng et al., 2015; Haerter et al., 2019; Meyer and Haerter, 2020; Schlemmer and Hohenegger, 2014; Torri and Kuang, 2019; Torri et al., 2015) and the impact of cold pools on convective self-aggregation (Haerter, 2019; Jeevanjee and Romps, 2013; Nissen and Haerter, 2021).

Despite the crucial role of cold pools in organizing atmospheric convection, our perception of basic properties like their size, shape, and structure is mostly based on high-resolution numerical simulations, often applied on idealized setups. The reported sizes of simulated cold pools range from below 5 km (Drager et al., 2020) to several tens of km (e. g., Romps and Jeevanjee, 2016; Tompkins, 2001). This does not only reflect the highly dynamic character of cold pools but also the variety of parameters that can be used for the cold pool identification, e. g., temperature, buoyancy, or radial wind velocity (Drager and van den Heever, 2017). The shape of cold pools is often assumed to be circular (e. g., Haerter et al., 2019; Meyer and Haerter, 2020; Romps and Jeevanjee, 2016), but Torri and Kuang (2019) also found that they quickly lose their initially circular shape as they grow and merge into larger clusters. The most poorly determined spatial property of cold pools is their structure. While for theoretical considerations often a uniform temperature is assumed (e. g., Romps and Jeevanjee, 2016), other simulation-based studies find a ring-like structure, which is attributed to the gust front formation and moisture accumulation at the leading edge of cold pools (e. g., Langhans and Romps, 2015; Zuidema et al., 2017). However, the recent findings are still inconsistent regarding the fact if cold pools are coldest in their centers (Drager et al., 2020) or at their boundaries (Meyer and Haerter, 2020). A few studies also examine the growth of cold pools (e. g., Drager and van den Heever, 2017; Haerter et al., 2019; Romps and Jeevanjee, 2016; Tompkins, 2001), which is usually described as a process at constant velocity that is controlled by the density current-like expansion of a cold pool due to its density excess relative to the environment. Moreover, the deceleration of cold pool expansion at large radii is attributed to the impact of turbulent heat fluxes (Gentine et al., 2016; Grant and van den Heever, 2016, 2018; Romps and Jeevanjee, 2016).

Also a myriad of observational studies aim at describing the size, life cycle, and horizontal and vertical structure of cold pools based on stationary point measurements (e. g., Engerer et al., 2008; Goff, 1976; Kruse et al., 2022; Touzé-Peiffer et al., 2022; Vogel et al., 2021), aircraft observations (Terai and Wood, 2013), or ship observations (Feng et al., 2015). However, by definition these analyses need to rely on various assumptions on the cold pool morphology. In a recent study, van den Heever et al. (2021) introduced the $C^3$LOUD-Ex campaign that characterized the spatial variability of cold pool temperature on scales between $\mathcal{O}(100)$ m and $\mathcal{O}(1)$ km using uncrewed aerial systems, radiosondes, and three closely-spaced surface stations. Although these studies apply a large variety of approaches to describe the spatial characteristics of cold pools, this challenging task was not yet satisfactorily addressed. As a consequence, the morphology of cold pools as found in numerical simulations or being used as a starting point for theoretical considerations cannot be sufficiently validated, which considerably limits our understanding of cold pools and the factors controlling their characteristics.

In the present study we use observation data of the Field Experiment on Sub-mesoscale Spatio Temporal Variability in Lindenberg (FESSTVaL) that allow us for the first time to obtain a spatial view into cold pools over land based on in situ measurements on the

sub-mesoscale, i. e., on scales between $\mathcal{O}(100)$ m and $\mathcal{O}(10)$ km. More specifically, we focus on the following questions:

1. What are the morphological properties of observed cold pools?
   - How large are cold pools?
   - Are cold pools round (i. e., circularly shaped)?
   - How heterogeneous is the temperature structure inside cold pools?
2. Which factors control the size and strength of cold pools during their growth phase?

The basis of the novel measurement strategy of FESSTVaL is a surface-based network of 99 low-cost, custom-built measurement stations that were successfully tested during the precursor experiment the Field Experiment on Sub-mesoscale Spatio Temporal variability at Hanseatic city of Hamburg (FESST@HH) in summer 2020 as described in Study B. To quantify the impact of rainfall for controlling the morphology of cold pools, we use measurement data of an X-band rain radar. Moreover, we apply the density current theory to the derived properties of the sampled cold pools to describe their expansion and analyze temperature and humidity profiles measured by radiosondes.

## C.2 DATA

The presented observation data were collected during FESSTVaL from May to August 2021. FESSTVaL was a field campaign held in eastern Germany that aimed at characterizing the variability of structures and processes in the atmospheric boundary layer on the sub-mesoscale. The experiment explored novel measurement approaches and featured observations by dense station networks, unmanned aircraft systems, and different ground-based remote sensing instruments. In this study, we mostly focus on the data collected by the network of Autonomous cold POoL LOgger (APOLLO) and Weather Transmitter (WXT) stations (Study B) as well as the X-band rain radar. The analysis in Section C.5 also includes measurement data (Kirsch et al., 2021) collected during the preceding experiment FESST@HH that took place in Hamburg (northern Germany) from June to August 2020.

### C.2.1 *Station network*

The key component of the FESSTVaL measurement strategy is a dense network of custom-built weather stations that are optimized for the observation of cold pools. The station type APOLLO consists of a low-cost and power-efficient data logger, which is mounted on a 3-m mast. The station is equipped with fast-response air temperature and pressure sensors that sample at 1-s resolution to adequately capture rapid signals changes typically associated with cold pool fronts. The sensors are placed inside a radiation shield on top of the mast and inside the logger box, respectively. The data logger is powered by a power bank battery and able to operate independently of external power for about 10 to 14 d. The second station type used for the network is the WXT weather station. Its main component is a commercial compact multi-parameter sensor (type: Vaisala Weather Transmitter WXT536) that records air temperature, pressure, relative humidity, wind speed, wind direction, and precipitation at 10-s resolution. Additionally, an external fast-response thermometer inside a separate radiation shield allows for smaller response times of the temperature measurement than the compact sensor. Since the station is equipped with a lead battery and a solar panel, it can operate without external power for several months. All units are

also mounted on a 3-m mast. A detailed technical description of the APOLLO and WXT stations can be found in Study B.

The FESSTVaL station network covers an area of about 30 km in diameter in the surrounding of the Meteorological Observatory Lindenberg – Richard Aßmann Observatory (MOL-RAO), which is located about 60 km south-east of Berlin (Germany) and operated by the German Weather Service. The network consists of 80 APOLLO and 19 WXT stations that are roughly arranged along concentric rings centered at the Falkenberg boundary layer measurement site (52.1666°N, 14.1229°E) about 5 km south of the MOL-RAO (Figure C.1a). The majority of stations (88) was installed along public roads, while the remaining stations formed local clusters at the three supersites MOL-RAO (three stations), Falkenberg (five stations), and the fields of a farmer in Birkholz (three stations). The average nearest-neighbor distance between all 99 measurement sites is 1.98±1.26 km (± indicates the standard deviation) with the minimum near the network center (0.1 km) and the maximum towards the outer regions (4.8 km). The experiment area is located in a sparsely populated environment that is characterized by agriculture, forests, scattered lakes, and mostly flat terrain. The elevation of measurement sites ranges between 39 m and 116 m above mean sea level.

The data set of the FESSTVaL network covers the period from 17 May to 27 August 2021 (Kirsch et al., 2022). The overall availability of quality controlled data is 92.0 % and 98.1 % for the APOLLO and WXT stations, respectively. Since the APOLLO stations were successively activated during the first week of the experiment phase, their data availability is significantly reduced before 20 May. Details on processing of the measurement data and performed quality checks can be found in Study B.

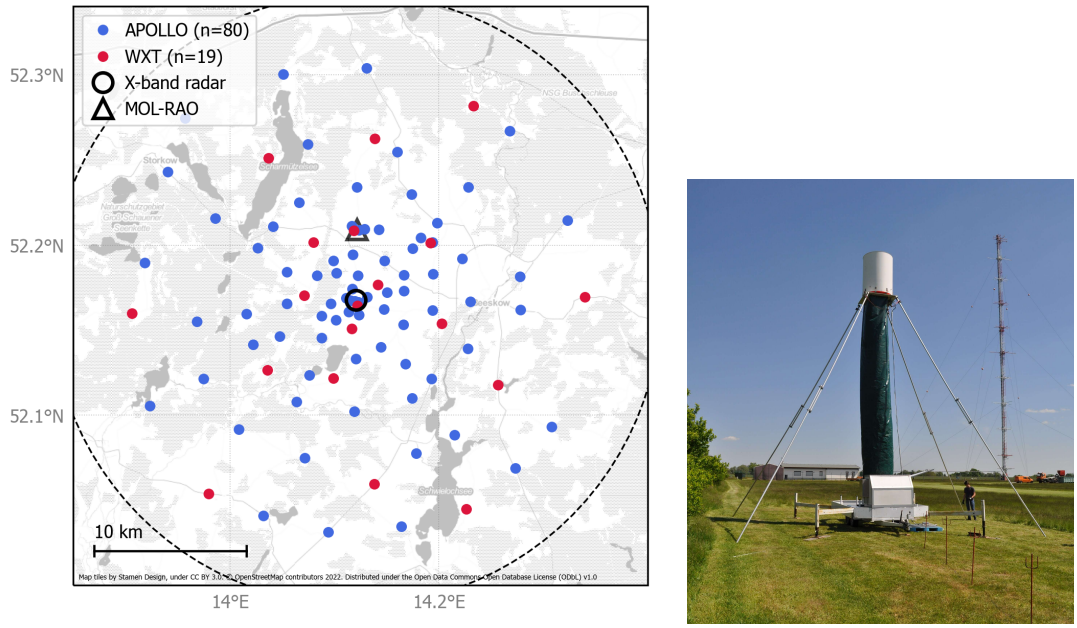


(a) (b)

Figure C.1: (a) Map of measurement locations of APOLLO and WXT weather stations during the FESSTVaL 2021 experiment. Indicated are also the location and the 20-km scanning range (dashed line) of the X-band rain radar and the MOL-RAO. (b) X-band rain radar installed on the platform of a trailer at the Falkenberg measurement site.

### C.2.2 *Rain radar*

For a continuous estimation of the current rainfall rate, the ground-based station network is complemented by an X-band rain radar. The instrument is based on a modified ship navigation radar that performs single-polarized backscatter measurements at 9.4-GHz frequency (Lengfeld et al., 2014). It scans the atmosphere at a fixed elevation angle of 2.3° at resolutions of 60 m in range, 1° in azimuth, and 30 s in time and a maximum range of 20 km. The radar is mounted on the platform of a trailer and hydraulically lifted to about 8 m above ground (Figure C.1b).

The X-band radar was located at the Falkenberg site in the center of the station network and operated between 3 June and 30 August 2021 (Figure C.1). The rainfall rate estimate is obtained by applying several error corrections on the raw reflectivity signal, which includes the correction for attenuation and noise, the removal of non-meteorological echoes, and the calibration against a micro rain radar at MOL-RAO. The availability of quality- controlled data throughout the measurement period is 98.2 % (Burgemeister et al., 2022b). Section C.5 also presents analyses based on X-band radar measurements performed in Hamburg in 2020 (Burgemeister et al., 2022a).

## C.3 CHARACTERIZATION OF COLD POOL EVENTS

In this study, we aim to characterize the morphology of cold pools observed during FESSTVaL. For this purpose, we identify the sampled cold pool events and describe how to derive their morphological properties from the introduced network measurements.

### C.3.1 *Identification*

Atmospheric convection over an area of size as the station network in consideration, i. e., several tens of km in diameter, typically lasts for a few hours and may produce one or more cold pools. This is what we refer to as a cold pool event in the following. When the experiment area is affected by a cold pool event, we expect multiple stations of the network to observe a rapid decrease in air temperature within a time period of 1 to 2 h (assuming a propagation velocity of 5 to 10 m $s^{-1}$). For the identification of these situations, we apply the cold pool detection algorithm as described in Study A to all network stations. The detection criterion for a local cold pool passage is a temperature drop of at least 2 K within 20 min. Potential cold pool events are defined as periods with at least five detections over the network per hour. Their plausibility is checked based on the visual inspection of corresponding rain radar imagery and a comparison with the list of cold pool events documented during the experiment. The start time of confirmed events is set to the next full or half hour before the onset of rainfall when the temperature field was presumable still unperturbed. Since the duration of individual event is not known a priori, we consider a standard duration of 4 h, which allows to capture long-lasting events but does not impact the evaluation of shorter events.

For the 103-d measurement period of FESSTVaL, we identify a total number of 42 cold pool events. Figure C.2 illustrates the distribution of maximum temperature perturbation $\Delta T_{max}$ detected at the individual network stations during all events. The majority of events (33) exhibits a median $\Delta T_{max}$ of -4 K or weaker, while it is stronger than -6 K for only two events. However, the range of signal strength within the network can be even larger, especially for strong events. Additionally, the affected portion of the network largely

varies between the events. Note that Figure C.2 shows signals weaker than the detection threshold of -2 K, since the maximum signal $\Delta T_{max}$ at a single station is calculated over a 90-min period, which can be smaller than the largest gradient during the event that is detected by the identification algorithm (see Study A for details).

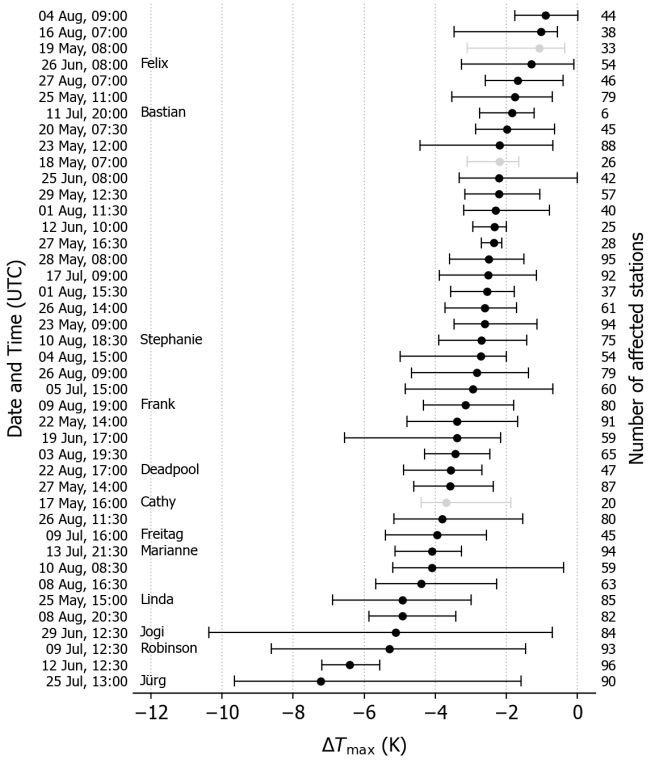


Figure C.2: Distribution of maximum temperature perturbation $\Delta T_{max}$ detected at individual APOLLO and WXT stations during the 42 cold pool events of FESSTVaL. Blacks dots and whiskers mark the median value and 5th/95th percentiles, respectively. The events are sorted according to their median value in $\Delta T_{max}$. Events with an average data availability over all stations of less than 75 % are marked in gray. Indicated are also the number of stations that have experienced a cold pool passage and the names given to selected events.

### C.3.2 *Spatio-temporal analysis*

For characterizing the morphology of cold pools, we need to reconstruct their three-dimensional ($x$,$y$,$t$) structure from the network observations. As the basic idea of this analysis, we define a cold pool as a spatially connected area with temperature perturbation $\Delta T$ relative to an estimated reference state without the presence of a cold pool. In a first step, we define the time-dependent reference temperature $T_{ref}(t)$ that is valid for all stations of the network. $T_{ref}(t)$ is given by the linear temperature trend fitted to the median signal of all network stations during the first 60 min of the event, in which the temperature field is largely undisturbed, and extrapolated over the entire event period. Secondly, we calculate the signal $\Delta T_i(t)$ at the individual measurement points $i$ as the difference from $T_{ref}(t)$. To reduce the impact of instrumental noise, we smooth the APOLLO station measurements with a 10-s running mean filter.

As the central step of the analysis, we apply kriging to interpolate the $\Delta T$ signal at the irregularly spaced network points to a regular 1-km×1-km grid. Kriging is a geostatistical method that uses information of the spatial auto-correlation of a variable described by variograms to estimate values at unsampled points (Wackernagel, 2003). Here, we apply an ordinary kriging algorithm (Murphy et al., 2021) and approximate its spatial auto-correlation with a power model variogram, which is suited to capture various shapes of heterogeneity in presence of a cold pool. We perform the kriging interpolation at 1-min intervals during the 4-h event period. Consistent with the identification criterion at the single stations, grid points inside a cold pool are defined by $\Delta T \leq -2\,\mathrm{K}$. Furthermore, all grid points more than 5 km away from a measurement station are considered as unreliable and excluded from the analysis. To determine morphological properties of the entities formed by identified cold pool grid points, we define a cold pool object as a four-connected cluster larger than $10\,\mathrm{km}^2$, whereas multiple clusters per time step are possible. Here, we focus on the size and shape of the analyzed clusters and their spatial distribution of $\Delta T$.

For further interpretation of the near-surface cold pool signal, we also include the radar-derived precipitation into the analysis. To match the interpolation of $\Delta T$ and preserve the high spatial resolution of the radar, we transfer the rainfall signal from its native polar grid to an aligned regular grid at 0.2-km resolution using a nearest-neighbour interpolation. Furthermore, we only consider grid points with rain rate $R \geq 1\,\mathrm{mm\,h^{-1}}$. Figure C.3 shows an exemplary analysis of $\Delta T$ and $R$ during cold pool event *Jogi* on 29 June 2021. The expected footprint of the convective precipitation cells is clearly visible in the overall structure of the interpolated temperature signal. Although finer structures of the precipitation field are smoothed out by the coarser resolution of the station network especially towards its boundary, the observational setup is suited to characterize morphological properties of cold pools.

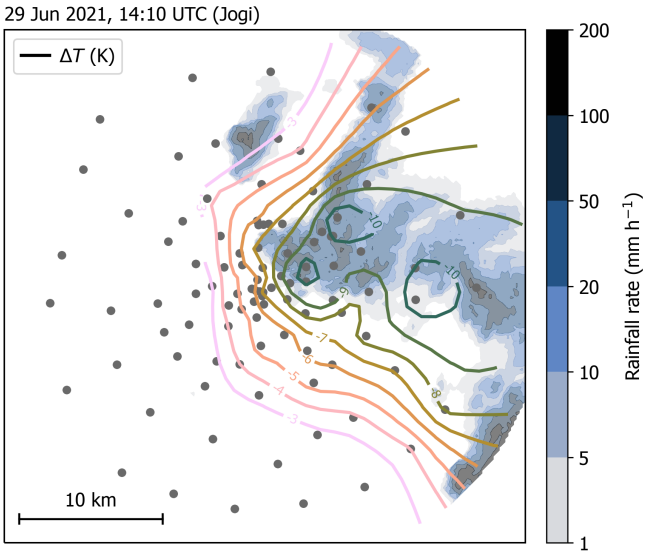


Figure C.3: Interpolated field of temperature perturbation $\Delta T$ (colored isolines) observed by the FESSTVaL station network (gray dots) and radar-measured rainfall rate (blue shading) during cold pool event *Jogi* on 29 June 2021 at 14:10 UTC (color maps by Crameri, 2018). Note that the -2-K isoline is not displayed due to numerical reasons.

## C.4 COLD POOL MORPHOLOGY

After describing how to identify cold pool objects in the observational data set of FESSTVaL, we apply the method to the sample of cold pool events to statistically characterize their morphological properties, i. e., their size, shape, and temperature structure.

### C.4.1 *Filtering of objects*

The basis for the statistical analysis of the morphological cold pool properties is formed by the objects found in the 1-min time steps of the 42 cold pool events. The introduced method identifies a total of 4955 objects during 39 events, while the remaining three events do not feature objects with the minimum required size of 10 $km^2$. Figure C.4a shows the frequency distribution of equivalent diameter $d_{equi}$ (i. e., diameter of a circle with same area) for all analyzed objects, which exhibits a bi-modal shape with local maxima at about 8 km and 40 km and a median of 17.4 km. However, this distribution does not allow a meaningful interpretation of the average cold pool size as the individual objects usually reach beyond the boundaries of the station network (Figure C.3) and we do not know the area fraction that is inside of it. 560 objects (11.3 %) even cover the entire domain of ($d_{equi} = 39.4\,km$) and, therefore, artificially accumulate as the second peak in the distribution.

To obtain a reliable estimation of the size and shape of the cold pool objects, we either have to make assumptions on the extent of the cold pools outside the network or only consider objects that are (mostly) inside the network. As the shape of cold pools may become highly irregular, e. g., due to merging of multiple cells, and the derivation of the observed shape is one goal of this study, we stick to the latter approach. To identify cold pool objects inside the station network, we define the boundary contact parameter $f_b$ that indicates the fraction of cold pool perimeter that touches the network boundary. According to a median value for $f_b$ of 0.51, a significant portion of objects is only partially captured by the station network. In fact, $f_b$ is zero for only 925 objects (18.6 %). As a trade-off between sample size and integrity of the results, we choose $f_b \leq 0.25$ as a filter criterion for the following analyses. The remaining 1278 objects exhibit a median $d_{equi}$ of 8.4 km, whereas the second peak at the large end of the spectrum disappears, confirming that mostly large objects are removed from the sample (Figure C.4a). Moreover, the filtering decreases the median cold pool strength in terms of object-mean temperature perturbation $\overline{\Delta T}$ from -2.6 K to -2.3 K, still maintaining a long-tailed distribution shape (Figure C.4b).

### C.4.2 *Statistical analysis*

We use the filtered sample of 1278 cold pool objects to statistically investigate their morphology. For a more thorough understanding of their properties, we additionally define sub-samples of small and large as well as weak and strong cold pools, whereas the groups are classified according to a size lower or higher than the median of $d_{equi}$ (8.4 km) and a strength higher or lower than the median of $\overline{\Delta T}$ (-2.3 K), respectively. Figure C.5 summarizes the respective frequency distributions of $d_{equi}$, $\overline{\Delta T}$, aspect ratio, and standard deviation $\sigma_{\Delta T}$ for all filtered objects and the four sub-samples. As already shown in Section C.4.1, $d_{equi}$ exhibits a slightly skewed distribution with a median of 8.4 km and extreme values $> 20\,km$ (Figure C.5a). This finding is in line with similar cold pool sizes found in observations (Feng et al., 2015; Terai and Wood, 2013) and numerical simulations (Tompkins, 2001). However, the extent of the station network limits a general assessment

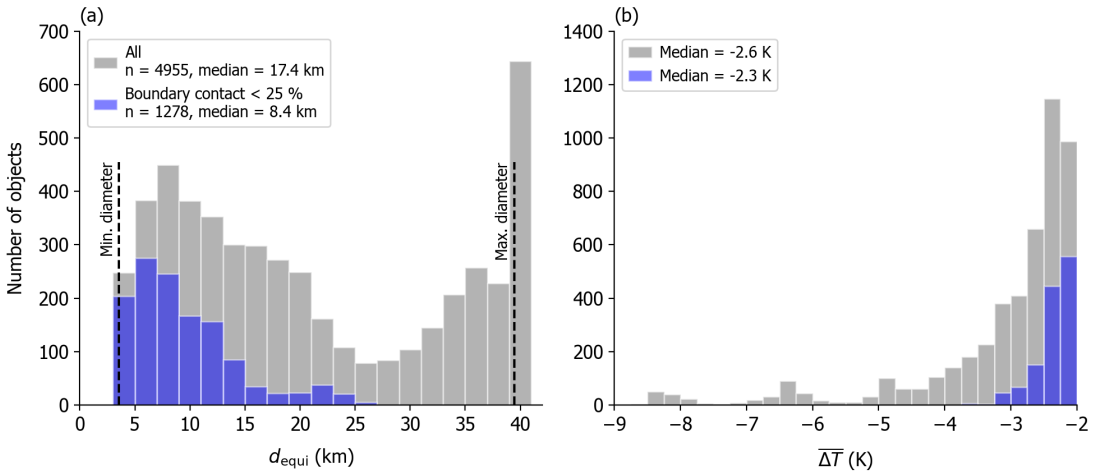


Figure C.4: Frequency distribution of (a) equivalent diameter $d_{equi}$ and (b) object-mean temperature perturbation $\overline{\Delta T}$ for cold pool objects observed by the FESSTVaL station network between 17 May and 27 August 2021. Gray bars represent data for all 4955 objects analyzed for 39 cold pool events at 1-min intervals, while blue bars are for 1278 objects whose boundary matches the boundary of the network by not more than 25 %. $d_{equi}$ is the diameter of a circle with same area as the analyzed object. Dashed black lines in (a) mark the minimum and maximum diameter set by the chosen area threshold for objects (10 $km^2$ $\equiv$ 3.6 km) and the domain size (1222 $km^2$ $\equiv$ 39.4 km; including the 5-km interpolation range around stations), respectively.

of the absolute cold pool size, since it strongly depends on the chosen threshold for $f_b$ and is biased towards small sizes. Additionally, the true cold pool size is underestimated by the applied detection threshold of $\Delta T \leq -2$ K, which does not include regions with weaker signals that still could be considered as part of the cold pool. The analysis also does not include information on the age of objects, i. e., growth by expansion or merging, as the parent rainfall cells rarely originate inside the network. Still, the distribution of equivalent diameter for the sub-samples of weak and strong cold pools is significantly different from each other according to a Mann–Whitney $U$ test ($p < 0.001$) that suggests that stronger cold pools are larger than weak ones. This result is insensitive to the choice of the threshold for $f_b$ (not shown). Also the reverse statement of larger cold pools being stronger than small ones is true ($p < 0.001$; Figure C.5b).

Idealized representations of cold pools generally picture circular objects (e. g., Romps and Jeevanjee, 2016). To test this assumption, we determine the approximate shape of the sampled objects based on their aspect ratio. The aspect ratio is defined as the fraction between the length of major axis and minor axis of an ellipse fitted to the object, attributing values of 1 to circularly shaped and greater than 1 to elongated objects. Figure C.5c shows that the aspect ratio for the entire sample exhibits a median of 1.55 and ranges between about 1.1 and 2.6. This result suggests that the cold pool objects sampled by the station network are generally not round, which contradicts the idealized conception of the cold pool shape. The same is true for the four sub-samples as their median aspect ratio lies between 1.54 and 1.60. While the differences between weak and strong cold pools are not significant ($p = 0.145$), small cold pools tend to be rounder than large ones ($p < 0.001$), although the absolute differences are small. One explanation for this finding might be the tendency of initially small cold pools to merge into larger and irregularly shaped clusters

as they grow (Torri and Kuang, 2019). Furthermore, the inspection of single cases suggests that the propagation of parent rainfall cells stretches the associated cold pools along the direction of the background flow.

Another characteristic of interest is the heterogeneity of the temperature field inside the cold pool objects that we quantify by the standard deviation $\sigma_{\Delta T}$ of temperature perturbation $\Delta T$ (Figure C.5d). For all objects, $\sigma_{\Delta T}$ varies between about 0.1 K and 0.65 K, which is in the same order of magnitude as the typical variability of the temperature field without the presence of a cold pool. Moreover, $\sigma_{\Delta T}$ is significantly ($p < 0.001$) larger for large and strong cold pools, which implies that the temperature inside a cold pool is far from being uniform but rather its gradient increases when the cold pool grows and intensifies. This effect may be supported by the previously mentioned merging of multiple objects. However, this analysis does not provide information on the spatial structure of the variability, i. e., if the temperature field typically varies randomly or follows a systematic shape.

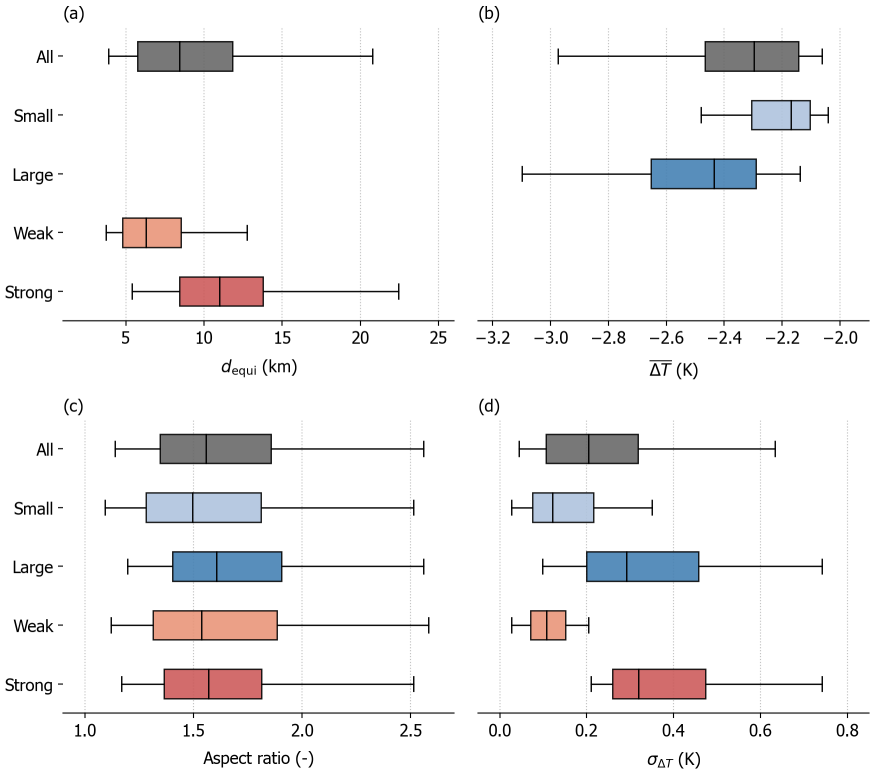


Figure C.5: Distribution of (a) equivalent diameter $d_{\text{equi}}$, (b) object-mean temperature perturbation $\overline{\Delta T}$, (c) aspect ratio, and (d) standard deviation $\sigma_{\Delta T}$ of $\Delta T$ of cold pool objects with a maximum network boundary contact of 25 %. Shown are the respective data for all 1278 objects (gray), for objects smaller (light blue) and larger (dark blue) than the median of $d_{\text{equi}}$, and objects weaker (light red) and stronger (dark red) than the median of $\overline{\Delta T}$. Distributions of sub-samples defined by the respective variables on the $x$-axis are not shown. The aspect ratio represents the ratio between major axis and minor axis of an ellipse fitted to the object. Vertical lines, boxes, and whiskers mark the median value, 25th/75th percentiles, and 5th/95th percentiles, respectively.

## C.5 COLD POOL GROWTH

As the statistical analysis of cold pool objects demonstrates, the FESSTVaL station network is especially suited to study the small end of the cold pool size spectrum. To better understand what determines the size of cold pools and how it develops at the early stages of the convective life cycle, we focus on the growth phase of selected events and relate their properties to the precipitation signal measured by the X-band radar.

### C.5.1 *Definition of growth phase*

Although the FESSTVaL data set contains a total number of 42 cold pool events, the majority of events was only partially sampled by the station network, as well in space as in time. Since we are especially interested in a complete view of the early stages of the cold pool life cycle, we manually select individual cases suited for analysis of their growth phase, i. e., they are initiated and continuously grow inside the network rather than moving into it with the parent convective cell. We define the begin of the growth phase as the time when the area of the cold pool object first exceeds the detection threshold of 10 $\mathrm{km}^2$. The growth phase ends when the object reaches the maximum size during its life cycle or becomes too large for a reasonably characterization, here defined by boundary contact $f_\mathrm{b} \geq 2/3$. Primitive tracking of cold pool properties throughout an event is performed by identifying the largest object of the current time step.

We identify four events that comply with the required criteria, namely cold pools *Elphi* (10 August 2020), *Felix* (26 June 2021), *Jogi* (29 June 2021), and *Jürg* (25 July 2021), whereas *Elphi* was observed during the FESST@HH experiment in Hamburg. The time series of cold pool area $A_\mathrm{CP}$ in Figure C.6a shows that all the selected cases grow at a nearly constant rate for between 55 and 75 min. While cold pools *Elphi*, *Jogi*, and *Jürg* grow to a size of more than 1000 $\mathrm{km}^2$ and beyond the applied threshold for $f_\mathrm{b}$, *Felix* only reaches a maximum area of around 100 $\mathrm{km}^2$ and is the only event whose entire life cycle, including its dissipation phase, is captured by the station network. This fact might explain the decelerated growth before reaching its maximum area. Note that the short-term negative tendencies in $A_\mathrm{CP}$ are associated with inaccuracies of the analysis method due to local temperature fluctuations rather than an unrealistic shrinkage in cold pool size.

The development of object-mean temperature perturbation $\overline{\Delta T}$ is much more variable among the four cases (Figure C.6b). Although all events start their growth phase at a $\overline{\Delta T}$ of between -2 K and -2.5 K, their terminal values vary between around -3 K (*Felix*), -4.5 K (*Elphi*), and -7 K (*Jogi* and *Jürg*). Except for *Jürg*, the relative decrease in $\overline{\Delta T}$ is strongest during the early phase of cold pool growth and levels later on. *Elphi* and *Jogi* appear to reach their maximum strength already after 35 and 55 min, respectively, and start to weaken afterwards when they still grow.

Figure C.6c shows the temporal evolution of area-integrated accumulated rainfall amount $\Sigma R_\mathrm{Radar}$ observed by the X-band rain radar during the growth phase of the respective cold pool events. $\Sigma R_\mathrm{Radar}$ indicates the absolute rainfall amount observed within the entire radar domain rather than inside the analyzed cold pool objects. This ensures to capture also rainfall not overlapping with the analyzed cold pool, which is especially relevant for *Felix* but does not impact the results of the other cases. The largest total rainfall amount of about $6 \times 10^9$ L is observed for *Jogi* and *Jürg*, whereas in the latter case the rainfall considerably intensifies after 25 min. In both cases the rainfall also does not diminish towards the end of the analyzed growth phase, suggesting the parent rainfall cells still being active. For *Elphi* and *Felix*, the rainfall accumulates to a much lower amount

of less than $1 \times 10^9$ L and stops before the growth phase ends. Note that for *Elphi* $\Sigma R_{\text{Radar}}$ is likely to be underestimated, since at the end of the growth phase approximately one third of the cold pool object lies outside of the range of the Hamburg radar.

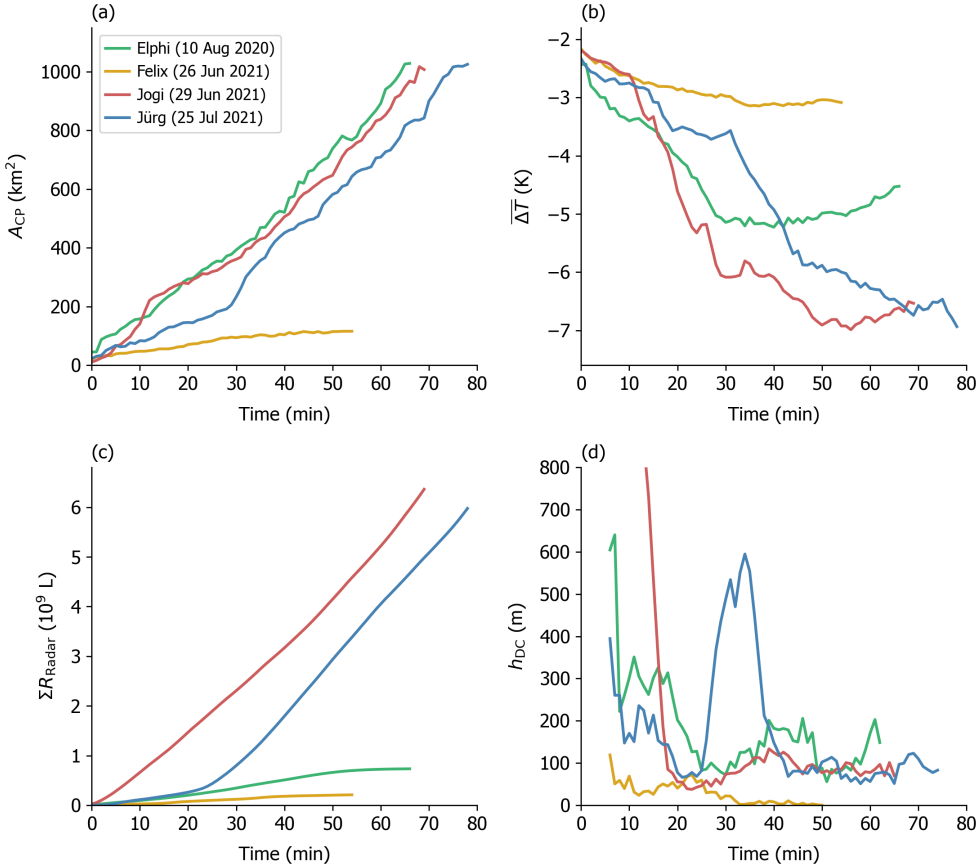


Figure C.6: Time series of (a) cold pool area $A_{CP}$, (b) object-mean temperature perturbation $\overline{\Delta T}$, (c) area-integrated accumulated rainfall amount $\Sigma R_{\text{Radar}}$, and (d) density current height $h_{DC}$ during the growth phase of cold pool events *Elphi* (initiated on 10 August 2020 at 13:07 UTC), *Felix* (26 June 2021, 09:12 UTC), *Jogi* (29 June 2021, 13:24 UTC), and *Jürg* (25 July 2021, 13:46 UTC). $\Sigma R_{\text{Radar}}$ refers to the absolute rainfall amount observed by the X-band radar over its entire range. $h_{DC}$ indicates the height of an idealized density current according to Equation C.1 with growth rate $\mathrm{d}r_{\text{equi}}/\mathrm{d}t$ and $\overline{\Delta T}$ as observed by the station network, whereas the first is smoothed with a 10-min running mean.

### C.5.2 *Drivers of growth*

#### C.5.2.1 *Precipitation*

We know that precipitation is a main factor for cold pool formation, both by evaporation of rainfall and melting of ice-phase hydrometeors within the cloud and in under-saturated sub-cloud layer air. Therefore, we would expect that the spatial properties of a cold pool are directly related to the amount of precipitation. Figure C.7a illustrates the relation between $\Sigma R_{\text{Radar}}$ and $A_{CP}$ for the growth phase of the four selected cold pool events, whereas both quantities are normalized between 0 and 1 to facilitate comparison. According

to correlation coefficients $r$ between 0.977 and 0.996, the observed rainfall amount and cold pool area exhibit a nearly perfect linear relationship for all four cases, although the absolute rainfall amounts differ by more than one order of magnitude. While the main underlying process should be the rainfall evaporation, also the vertical transport of upper-level air masses into the sub-cloud layer by precipitation-driven downdrafts might support this relationship. Also $\overline{\Delta T}$ provides evidence for the impact of evaporation. The relative dependence of $\overline{\Delta T}$ on $\Sigma R_{\text{Radar}}$ agrees very well between the different cases, showing a non-linear relationship with strongest cooling in the early phase of growth and weaker cooling later on (Figure C.7b). More specifically, the first half of the total rainfall amount observed during the growth phase already leads to about 80 % of the maximum $\overline{\Delta T}$ averaged over the cold pool area (neglecting the very early cooling phase of the cold pool that does not satisfy the definition of $\Delta T \leq -2\,\text{K}$). The high relative cooling efficiency for young cold pools is most likely related to the large potential for evaporative cooling of initially unsaturated air masses and, therefore, supports the hypothesis of rainfall evaporation being the main cause for increase in cold pool volume.

The good agreement between the spatial cold pool properties and the radar-observed rainfall amount is surprising, since the analysis does not include the vertical dimension. In reality, a cold pool is a three-dimensional body whose volume is controlled by the amount of produced cold air and, therefore, is proportional to the total amount of involved precipitation (Fujita, 1959). The linear scaling between cold pool *area* and rainfall amount means that the cold pool height stays approximately constant during the growth. Additionally, the analysis assumes that the near-surface cooling is directly related to instantaneous evaporation of rainfall observed by the X-band radar at heights up to 700 m. However, given the high correlation this assumption might actually be valid, also with respect to the weak relationship between cold pool strength and surface rainfall (Study A).

The role of rainfall in controlling the properties of cold pools is also linked to the atmospheric conditions in which the parent convection develops. The lower-tropospheric profiles of temperature and absolute saturation deficit observed by radiosondes outside the cold pools show that *Elphi*, *Jogi*, and *Jürg* grow in much more favorable conditions for effective cooling by rainfall evaporation than the smallest and weakest of the discussed events, *Felix* (Figure C.8a and b). This suggests that a warm and dry boundary layer does not only promote strong temperature perturbations (Study A) but also the horizontal expansion of a cold pool, probably related to the increased density difference between cold pool and environment. However, the small sample size does not allow to derive a systematic relationship between the prevailing atmospheric conditions of the boundary layer and the strength, size, and precipitation amount of a cold pool. A potential controlling mechanism could be that the atmospheric stability favors or impedes the development of precipitation-driven downdrafts that support the expansion of a convective outflow. Moreover, wind shear may lead to preferential or suppressed horizontal expansion of the cold pool air.

### C.5.2.2 *Density current*

The physical process behind the expansion of a cold pool is often described in literature as a density current. When rainfall evaporates, the air cools, sinks to the surface, and horizontally propagates due to its decreased buoyancy relative to its environment and a horizontal pressure gradient force that pushes the cold pool air outwards (e. g., Grandpeix and Lafore, 2010; Rochetin et al., 2021). Based on early work by von Kármán (1940) and Benjamin (1968), the steady-state propagation velocity $u_{\text{DC}}$ of an inviscid, irrotational, and

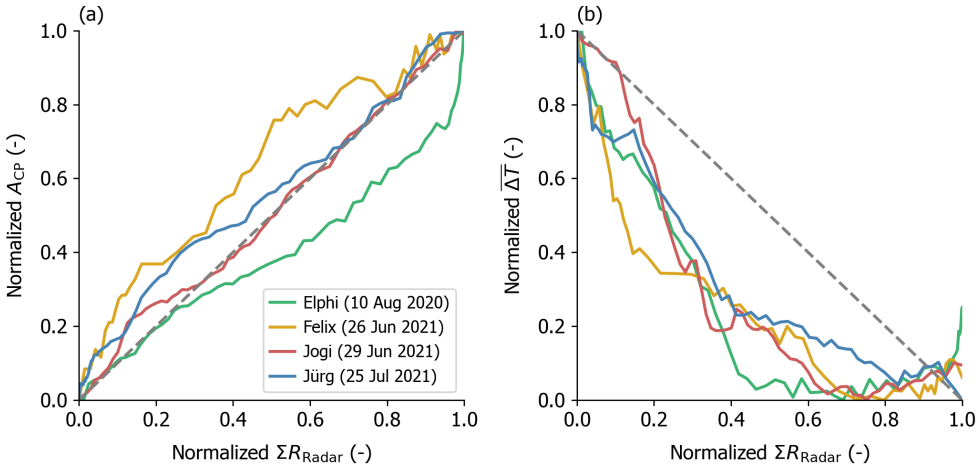


Figure C.7: (a) Cold pool area $A_{CP}$ and (b) object-mean temperature perturbation $\overline{\Delta T}$ dependent on area-integrated accumulated rainfall amount $\Sigma R_{Radar}$ during the growth phase of cold pool events *Elphi*, *Felix*, *Jogi*, and *Jürg*. The minimum–maximum range of all quantities is normalized between 0 and 1. Gray dashed lines are the 1-to-1 lines, whereas for (b) it is adapted to the negative values of $\Delta T$. Time runs from left to right in both (a) and (b).

incompressible density current with height $h_{DC}$ and temperature perturbation $\Delta T_{DC}$ can be described by

$$u_{DC} = k\sqrt{g\, h_{DC}\, \frac{\Delta T_{DC}}{T_0}}, \tag{C.1}$$

where $T_0$ is the environmental air temperature, $k$ the internal Froude number, and $g$ the gravitational acceleration. Here, we assume that the magnitude of the relative density gradient $\Delta\rho/\rho_0$ in the original version of Equation C.1 can be approximated with the relative temperature gradient $\Delta T/T_0$ (Kruse et al., 2022) and that $k$ is constant with a value of 0.7, which is found to be realistic in previous studies (e. g., Wakimoto, 1982). In a recent study, Kruse et al. (2022) showed that the wind gust strength of 189 cold pool passages observed in tower measurements increases with $\sqrt{\Delta T/T_0}$, providing evidence that the density current theory according to Equation C.1 is actually valid for real-nature cold pools. However, the applicability of the theory is still severely limited by our inability to reliably determine critical parameters like the cold pool height $h_{DC}$. A brief thought experiment helps to understand the role of $h_{DC}$ in Equation C.1: Let us consider an idealized body of cold pool air with constant temperature $\Delta T_{DC}$, which expands horizontally under volume conservation. Since $h_{DC}$ and $u_{DC}$ are proportional to $A_{DC}^{-1}$ and $A_{DC}^{-2}$, respectively, the density current would rapidly flatten, decelerate, and eventually stop.

We can test the validity of this theoretical scenario by estimating the actual cold pool height from observational data of the four described events. As the present data set allows to directly quantify the average propagation velocity of the thermal air mass boundary via the expansion of equivalent cold pool radius $r_{equi}$, the density current height $h_{DC}$ remains the only unknown quantity in Equation C.1. When solving for $h_{DC}$, this allows us to directly calculate the height of a density current with mean temperature perturbation and expansion rate as observed (Figure C.6d). During the growth phase of the selected cold pool events, $h_{DC}$ mostly varies between 50 m and 350 m, which is at the lower end of values found in previous studies (e. g., Study A; Kruse et al., 2022; Terai and Wood, 2013).

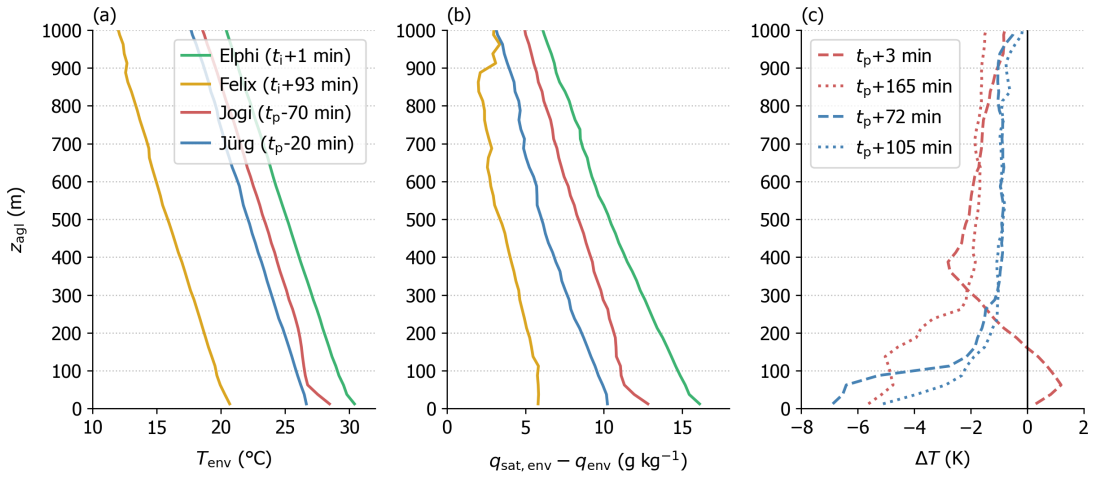


Figure C.8: Vertical profiles of (a) environmental temperature $T_{env}$, (b) environmental absolute saturation deficit $q_{sat,env} - q_{env}$, and (c) temperature perturbation $\Delta T$ observed by radiosondes ascents during the cold pool events *Elphi*, *Felix*, *Jogi*, and *Jürg*. The absolute saturation deficit is defined as the difference between saturation specific humidity $q_{sat,env}$ and specific humidity $q_{env}$. $z_{agl}$ indicates height above ground level and the variables are averaged in 25-m bins. Environmental profiles in (a) and (b) refer to conditions outside the cold pool, whereas $t_p$ indicates the time of cold pool passage at launch location and $t_i$ indicates the time of cold pool initiation, i. e., begin of growth phase, for cases without profiles inside the cold pool. Perturbation profiles in (c) refer to the differences of subsequent profiles inside the cold pool relative to the environmental profiles. All radiosondes were launched at the MOL-RAO, except for the first and second radiosondes during *Jogi* (launched at the Falkenberg site) and the radiosonde during *Elphi* (launched at the Hamburg Geomatikum building).

Consistent with $\overline{\Delta T}$ and $A_{CP}$, *Felix* is the most shallow of the four cold pools with a height of below 100 m, whereas the other three exhibit average heights between 100 m and 200 m. However, all cases share the common pattern that $h_{DC}$ is largest in the early growth phase and levels to a lower and roughly constant value after about 20 min. The latter finding is also confirmed by radiosonde observations for *Jogi* and *Jürg* showing approximately constant cold pool heights based on temperature perturbations in subsequent profiles (Figure C.8c). The initially larger heights of young cold pools and the peak after around 30 min in case of *Jürg* are most likely caused by the growth in rainfall area by newly developing convective cells rather than the expansion of the cold pool air itself. The constant heights later on reflect the dense air masses freely propagating away from the precipitating cell center. Therefore, these results provide evidence that the regions of a cold pool outside the rainfall areas can be well described as density currents.

When considering also the results of the previous section, then the constant cold pool height argues for a balance between the flattening of a density current expanding under volume conservation and the volume increase by cold air import through rainfall evaporation and convective downdrafts. In conclusion, both mechanisms, the cold air production and the subsequent density current-like expansion, act hand in hand and are crucial to sustain the growth of a cold pool.

## C.6 SUMMARY AND CONCLUSIONS

This study presents results of the FESSTVaL field experiment that explored new measurement approaches to quantify for the first time the morphology of convective cold pools based on in situ observations at sub-mesoscale resolution ($\mathcal{O}(100)$ m – $\mathcal{O}(10)$ km). The experiment took place at the MOL-RAO in eastern Germany between May and August 2021 and featured a dense ground-based network of 99 custom-built, low-cost measurement stations covering a circular area of about 30 km in diameter. High-resolution rainfall observations were performed by an X-band rain radar covering the entire network.

During the 103-d measurement period, the FESSTVaL network recorded a total number of 42 cold pool events. To determine the size, shape and structure of the sampled cold pools, we use a kriging algorithm to spatially interpolate the temperature observations of the station network to a regular grid and define four-connected clusters of grid points with temperature perturbation $\Delta T \leq -2$ K as cold pool objects. The analysis method applied to all cold pool events at 1-min intervals identifies 4955 cold pool objects, whereas most of them are only partially captured by the network. To filter cold pools suitable for a meaningful interpretation of their morphological properties, we restrict the analysis to objects that touch the network boundary by not more than a fraction $f_b = 0.25$ of their perimeter. The remaining 1278 cold pool objects exhibit a median equivalent diameter $d_{equi}$ of 8.4 km and a median object-mean $\overline{\Delta T}$ of -2.3 K. However, these values critically depend on $f_b$ and the limited size of the observational domain suggests that the sample is biased towards small and weak cold pools. Splitting the sample into halves in terms of size and strength reveals that large cold pools are significantly stronger than small cold pools and vice versa, insensitive to the choice of $f_b$. According to aspect ratios between 1.5 and 1.6, the analyzed objects are not round, independent of their size and strength. This finding contradicts the common conceptual model of cold pools and is most likely related to stretching of convective outflows along the mean flow and merging of multiple rain cells into irregularly shaped clusters. Moreover, the inner-cold pool temperature variability is significantly larger for large and strong objects, supporting the latter hypothesis.

The FESSTVaL observation network is particularly well suited to study small and young cold pools and to better understand the factors for growth in the early phase of their life cycle. The four cold pool events selected for detailed inspection originate inside the network and grow at almost constant rate for around 1 h, whereas for only one event reaches its maximum extent within the considered growth phase. For all four events, the cold pool area during growth scales linearly ($r \geq 0.977$) with the area-integrated accumulated rainfall amount observed by the X-band radar. Also the relative scaling between object-mean temperature perturbation and rainfall amount agrees very well among the different cases, consistently showing a higher cooling efficiency early in the life cycle than later on. More specifically, the first half of observed rainfall amount corresponds to approximately 80 % of the cooling beyond the detection threshold of -2 K. These findings clearly identify evaporation of rainfall in under-saturated sub-cloud layer air as the main source of cold air required to form a cold pool. Depending on precipitation intensity and atmospheric temperature structure, also the import of upper-level air masses by downdrafts supports the cold pool growth. Furthermore, the horizontal expansion of the cold pool air masses depends on the density excess relative to their environment. According to a theoretical relation for an idealized density current applied on the observed expansion rate and temperature perturbation as well as indications from radiosonde profiles, the height of a cold pool stays approximately constant throughout the later growth phase. Therefore, we conclude that the outer regions of the cold pool away from

its raining center propagate like a density current but are driven by the cold air import from precipitation that balances the decrease in vertical extent expected from expansion at constant volume.

The FESSTVaL experiment is a breakthrough in quantifying properties of cold pools that were previously obscured by insufficient resolution of existing observation systems. For the first time, in situ observations allow to determine the size and shape of cold pools, which are poorly described in previous studies. Although the generality of findings on cold pool size and shape is limited by the size of the station network and assumptions made for the analysis, the data set has the potential to serve as a benchmark for the morphology of cold pools over land. The good agreement in the scaling of size and strength with the rainfall amount among different cold pool events is remarkable given the diverse synoptical background conditions and gives confidence in the robustness of the results. The impact of precipitation, both directly by evaporative cooling and indirectly by downdrafts, clearly qualifies as the the main driver of cold pool growth that is needed to sustain its density current-like expansion. More detailed analyses in the future will provide a clearer picture of influence of rainfall duration, area, and intensity on the cold pool life cycle and their interplay with the environment set by atmosphere and soil conditions.

ACKNOWLEDGMENTS

The authors are thankful to Marco Clemens, Henning Dorff, Nele Gärtner, Daniel Klocke, Ingo Lange, Patrick Laufing, Pablo Sebastia Saez, Milica Stankovic, and Bernhard Stiehle for supporting the installation, maintenance, and dismantlement of measurement instruments during FESSTVaL. We thank Finn Burgemeister for operating the X-band rain radar and processing its data. We acknowledge the coordination of FESSTVaL before, during, and after the observation period by Sarah Wiesner and Kristina Lundgren. We are thankful to Frank Beyrich and the team of the German Weather Service at Lindenberg for heavily supporting the planning, execution, and logistics of the experiment. We thank the Landesbetrieb Straßenwesen Brandenburg, the Amt für Infrastruktur und Gebäudemanagement Landkreis Oder-Spree, and the Amt für Gebäude- und Immobilienmanagement Landkreis Dahme-Spreewald for issuing permission to install the measurement stations along public roads. We also thank Henrik Staar for supporting the experiment by providing technical assistance and ground for measurement sites.

The authors are thankful to Annika Jahnke-Bornemann and the Integrated Climate Data Center (ICDC) for the smooth data publication and curation.

This research was carried out in the Hans Ertel Center for Weather Research (Hans-Ertel-Zentrum für Wetterforschung; HErZ). This German research network of universities, research institutions, and the German Weather Service (Deutscher Wetterdienst; DWD) is funded by the Federal Ministry of Transport and Digital Infrastructure (Bundesministerium für Verkehr und digitale Infrastruktur; BMVI).

# BIBLIOGRAPHY


Barnes, Gary M. and Michael Garstang (1982). "Subcloud layer energetics of precipitating convection." In: *Mon. Weather Rev.* 110, pp. 102–117. DOI: 10.1175/1520-0493(1982)110<0102:SLEOPC>2.0.CO;2.

Basara, Jeffrey B., Bradley G. Illston, Christopher A. Fiebrich, Phillip D. Browder, Cynthia R. Morgan, Alexandria McCombs, Jared P. Bostic, Renee A. McPherson, Amanda J. Schroeder, and Kenneth C. Crawford (2011). "The Oklahoma City Micronet." In: *Meteorol. Appl.* 18.3, pp. 252–261. DOI: 10.1002/MET.189.

Bechtel, Benjamin, Paul J. Alexander, Jürgen Böhner, Jason Ching, Olaf Conrad, Johannes Feddema, Gerald Mills, Linda See, and Iain Stewart (2015). "Mapping local climate zones for a worldwide database of the form and function of cities." In: *ISPRS Int. J. Geo-Inf.* 4, pp. 199–219. DOI: 10.3390/IJGI4010199.

Benjamin, T. Brooke (1968). "Gravity currents and related phenomena." In: *J. Fluid Mech.* 31.2, pp. 209–248. DOI: 10.1017/S0022112068000133.

Boeing, Steven J., Harm J. J. Jonker, A. Pier Siebesma, and Wojciech W. Grabowski (2012). "Influence of the subcloud layer on the development of a deep convective ensemble." In: *J. Atmos. Sci.* 69, pp. 2682–2698. DOI: 10.1175/JAS-D-11-0317.1.

Bolton, David (1980). "The computation of equivalent potential temperature." In: *Mon. Weather Rev.* 108, pp. 1046–1053. DOI: 10.1175/1520-0493(1980)108<1046:TCOEPT>2.0.CO;2.

Bony, Sandrine et al. (2017). "EUREC4A: A field campaign to elucidate the couplings between clouds, convection and circulation." In: *Surv. Geophys.* 38.6, pp. 1529–1568. DOI: 10.1007/S10712-017-9428-0.

Borque, Paloma, Stephen W. Nesbitt, Robert J. Trapp, Sonia Lasher-Trapp, and Mariko Oue (2020). "Observational study of the thermodynamics and morphological characteristics of a midlatitude continental cold pool event." In: *Mon. Weather Rev.* 148.2, pp. 719–737. DOI: 10.1175/MWR-D-19-0068.1.

Bosch (2020). *BME280 data sheet, version 1.9*. Last access: 14 January 2021. URL: https://www.bosch-sensortec.com/media/boschsensortec/downloads/datasheets/bst-bme280-ds002.pdf.

Bruemmer, Burghard, Ingo Lange, and Heike Konow (2012). "Atmospheric boundary layer measurements at the 280 m high Hamburg weather mast 1995–2011: Mean annual and diurnal cycles." In: *Meteorol. Z.* 21, pp. 319–335. DOI: 10.1127/0941-2948/2012/0338.

Bryan, George H., John C. Wyngaard, and J. Michael Fritsch (2003). "Resolution requirements for the simulation of deep moist convection." In: *Mon. Weather Rev.* 131, pp. 2394–2416. DOI: 10.1175/1520-0493(2003)131<2394:RRFTSO>2.0.CO;2.

Burgemeister, Finn, Marco Clemens, and Felix Ament (2022a). *Multi-year X-band weather radar observations in Hamburg (LAWR HHG)*. World Data Center for Climate (WDCC) at DKRZ. DOI: 10.26050/WDCC/LAWR_UHH_HHG.

– (2022b). *Rainfall rates estimated from X-Band radar observations during FESSTVaL 2021, version 0*. Integrated Climate Data Center, Universität Hamburg. DOI: 10.25592/UHHFDM.10090.

Chandra, Arunchandra S., Paquita Zuidema, Steven Krueger, Adam Kochanski, Simon P. de Szoeke, and Jianhao Zhang (2018). "Moisture distributions in tropical cold pools from

equatorial Indian ocean observations and cloud-resolving simulations." In: *J. Geophys. Res.-Atmos.*. 123, pp. 11445–11465. DOI: 10.1029/2018JD028634.

Crameri, Fabio (2018). *Scientific colour maps, version 7.0.1*. Zenodo [code]. DOI: 10.5281/ZENODO.1243862.

Crameri, Fabio, Grace E. Shephard, and Philip J. Heron (2020). "The misuse of colour in science communication." In: *Nat. Commun.* 11, p. 5444. DOI: 10.1038/S41467-020-19160-7.

Dawson, Daniel T., Ming Xue, Jason A. Milbrandt, and M. K. Yau (2010). "Comparison of evaporation and cold pool development between single-moment and multimoment bulk microphysics schemes in idealized simulations of tornadic thunderstorms." In: *Mon. Weather Rev.* 138, pp. 1152–1171. DOI: 10.1175/2009MWR2956.1.

Deutscher Wetterdienst (2019). *DWD Bodenanalyse Archiv*. Last access: 8 July 2019. URL: http://www1.wetter3.de/archiv_dwd_dt.html.

Drager, Aryeh J., Leah D. Grant, and Susan C. van den Heever (2020). "Cold pool responses to changes in soil moisture." In: *J. Adv. Model. Earth Sy.* 12.e2019MS001922. DOI: 10.1029/2019MS001922.

Drager, Aryeh J. and Susan C. van den Heever (2017). "Characterizing convective cold pools." In: *J. Adv. Model. Earth Sy.* 9.2, pp. 1091–1115. DOI: 10.1002/2016MS000788.

Eaton, Brian et al. (2017). *NetCDF Climate and Forecast (CF) metadata conventions, version 1.7*. Last access: 14 January 2021. URL: https://cfconventions.org/Data/cf-conventions/cf-conventions-1.7/cf-conventions.pdf.

Emanuel, Kerry A. (1994). *Atmospheric convection*. Oxford University Press, p. 592. ISBN: 978-0-19-506630-2.

Engerer, Nicholas A., David J. Stensrud, and Michael C. Coniglio (2008). "Surface characteristics of observed cold pools." In: *Mon. Weather Rev.* 136, pp. 4839–4849. DOI: 10.1175/2008MWR2528.1.

Feng, Zhe, Samson Hagos, Angela K. Rowe, Casey D. Burleyson, Matus N. Martini, and Simon P. de Szoeke (2015). "Mechanisms of convective cloud organization by cold pools over tropical warm ocean during the AMIE/DYNAMO field campaign." In: *J. Adv. Model. Earth Sy.* 7, pp. 357–381. DOI: 10.1002/2014MS000384.

Fernando, H. J.S. (2003). "Convection — Laboratory models." In: *Encyclopedia of atmospheric sciences*. Academic Press, pp. 528–539. ISBN: 978-0-12-227090-1. DOI: 10.1016/B0-12-227090-8/00119-6.

Fujita, Tetsuya (1959). "Precipitation and cold air production in mesoscale thunderstorm systems." In: *J. Meteorol.* 16, pp. 454–466. DOI: 10.1175/1520-0469(1959)016<0454:PACAPI>2.0.CO;2.

Gentine, Pierre, Alix Garelli, Seung-Bu Park, Ji Nie, Giuseppe Torri, and Zhiming Kuang (2016). "Role of surface heat fluxes underneath cold pools." In: *Geophys. Res. Lett.* 43, pp. 874–883. DOI: 10.1002/2015GL067262.

Goff, R. Craig (1976). "Vertical structure of thunderstorm outflows." In: *Mon. Weather Rev.* 104, pp. 1429–1440. DOI: 10.1175/1520-0493(1976)104<1429:VSOTO>2.0.CO;2.

Grandpeix, Jean-Yves and Jean-Philippe Lafore (2010). "A density current parameterization coupled with Emanuel's convection scheme. Part I: The models." In: *J. Atmos. Sci.* 67, pp. 881–897. DOI: 10.1175/2009JAS3044.1.

Grant, Leah D. and Susan C. van den Heever (2015). "Cold Pool and precipitation responses to aerosol loading: Modulation by dry layers." In: *J. Atmos. Sci.* 72.4, pp. 1398–1408. DOI: 10.1175/JAS-D-14-0260.1.

Grant, Leah D., Todd P. Lane, and Susan C. van den Heever (2018). "The role of cold pools in tropical oceanic convective systems." In: *J. Atmos. Sci.* 75, pp. 2615–2634. DOI: 10.1175/JAS-D-17-0352.1.

Grant, Leah D. and Susan C. van den Heever (2016). "Cold pool dissipation." In: *J. Geophys. Res.-Atmos.* 121, pp. 1138–1155. DOI: 10.1002/2015JD023813.

– (2018). "Cold pool-land surface interactions in a dry continental environment." In: *J. Adv. Model. Earth Sy.* 10, pp. 1513–1526. DOI: 10.1029/2018MS001323.

Haerter, Jan O. (2019). "Convective self-aggregation as a cold pool-driven critical phenomenon." In: *Geophys. Res. Lett.* 46, pp. 4017–4028. DOI: 10.1029/2018GL081817.

Haerter, Jan O., Steven J. Böing, Olga Henneberg, and Silas Boye Nissen (2019). "Circling in on convective organization." In: *Geophys. Res. Lett.* 46.12, pp. 7024–7034. DOI: 10.1029/2019GL082092.

Haerter, Jan O. and Linda Schlemmer (2018). "Intensified cold pool dynamics under stronger surface heating." In: *Geophys. Res. Lett.* 45, pp. 6299–6310. DOI: 10.1029/2017GL076874.

Hirt, Mirjam, George C. Craig, Sophia A. K. Schäfer, Julien Savre, and Rieke Heinze (2020). "Cold-pool-driven convective initiation: using causal graph analysis to determine what convection-permitting models are missing." In: *Q. J. Roy. Meteor. Soc.* 146, pp. 2205–2227. DOI: 10.1002/QJ.3788.

Houze Jr., Robert A. (1993). *Cloud dynamics*. Academic Press, p. 573.

Jeevanjee, Nadir and David M. Romps (2013). "Convective self-aggregation, cold pools, and domain size." In: *Geophys. Res. Lett.* 40, pp. 994–998. DOI: 10.1002/GRL.50204.

Khairoutdinov, Marat and David Randall (2006). "High-resolution simulation of shallow-to-deep convection transition over land." In: *J. Atmos. Sci.* 63, pp. 3421–3436. DOI: 10.1175/JAS3810.1.

Kirchengast, Gottfried, Thomas Kabas, Armin Leuprecht, Christoph Bichler, and Heimo Truhetz (2014). "WegenerNet: A pioneering high-resolution network for monitoring weather and climate." In: *Bull. Am. Meteorol. Soc.* 95.2, pp. 227–242. DOI: 10.1175/BAMS-D-11-00161.1.

Kirsch, Bastian (2020). *cold_pool_detection Version 1.0*. DOI: 10.5281/ZENODO.4321260.

Kirsch, Bastian, Cathy Hohenegger, Daniel Klocke, and Felix Ament (2022). *Meteorological network observations by APOLLO and WXT weather stations during FESSTVaL 2021, version 00-2*. Integrated Climate Data Center, Universität Hamburg. DOI: 10.25592/UHHFDM.10179.

Kirsch, Bastian, Cathy Hohenegger, Daniel Klocke, Rainer Senke, Michael Offermann, and Felix Ament (2021). *FESST@HH meteorological network measurements, version 00-2*. Integrated Climate Data Center, Universität Hamburg. DOI: 10.25592/UHHFDM.10172.

Kruse, Irene L., Jan O. Haerter, and Bettina Meyer (2022). "Cold pools over the Netherlands: A statistical study from tower and radar observations." In: *Q. J. Roy. Meteor. Soc.* 148.743, pp. 711–726. DOI: 10.1002/QJ.4223.

Kurowski, Marcin J., Kay Suselj, Wojciech W. Grabowski, and Joao Teixeira (2018). "Shallow-to-deep transition of continental moist convection: Cold pools, surface fluxes, and mesoscale organization." In: *J. Atmos. Sci.* 75, pp. 4071–4090. DOI: 10.1175/JAS-D-18-0031.1.

Lammert, Andrea, Verena Grützun, and Erasmia Stamnas (2018). *The SAMD product standard (Standardized Atmospheric Measurement Data)*. Technical note. Zenodo. DOI: 10.5281/ZENODO.1741364.

Langhans, Wolfgang and David M. Romps (2015). "The origin of water vapor rings in tropical oceanic cold pools." In: *Geophys. Res. Lett.* 42, pp. 7825–7834. DOI: 10.1002/2015GL065623.

Lengfeld, Katharina, Marco Clemens, Hans Münster, and Felix Ament (2014). "Performance of high-resolution X-band weather radar networks – The PATTERN example." In: *Atmos. Meas. Tech.* 7, pp. 4151–4166. DOI: 10.5194/AMT-7-4151-2014.

Li, Zhujun, Paquita Zuidema, Ping Zhu, and Hugh Morrison (2015). "The sensitivity of simulated shallow cumulus convection and cold pools to microphysics." In: *J. Atmos. Sci.* 72, pp. 3340–3355. DOI: 10.1175/JAS-D-14-0099.1.

Madhavan, Bomidi Lakshmi, John Kalisch, and Andreas Macke (2016). "Shortwave surface radiation network for observing small-scale cloud inhomogeneity fields." In: *Atmos. Meas. Tech.* 9.3, pp. 1153–1166. DOI: 10.5194/AMT-9-1153-2016.

Markowski, Paul M., Jerry M. Straka, and Erik N. Rasmussen (2002). "Direct surface thermodynamic observations within the rear-flank downdrafts of nontornadic and tornadic supercells." In: *Mon. Weather Rev.* 130, pp. 1692–1721. DOI: 10.1175/1520-0493(2002)130<1692:DSTOWT>2.0.CO;2.

Markowski, Paul and Yvette Richardson (2010). *Mesoscale meteorology in midlatitudes*. Wiley-Blackwell, p. 407.

Meyer, Bettina and Jan O. Haerter (2020). "Mechanical forcing of convection by cold pools: Collisions and energy scaling." In: *J. Adv. Model Earth Sy.* 12.11. DOI: 10.1029/2020MS002281.

Mueller, Cynthia K. and Richard E. Carbone (1987). "Dynamics of a thunderstorm outflow." In: *J. Atmos. Sci.* 44, pp. 1879–1898. DOI: 10.1175/1520-0469(1987)044<1879:DOATO>2.0.CO;2.

Murphy, Benjamin, Sebastian Müller, and Roman Yurchak (2021). *GeoStat-Framework/PyKrige (v1.6.1)*. DOI: 10.5281/ZENODO.5380342.

Nissen, Silas Boye and Jan O. Haerter (2021). "Circling in on convective self-aggregation." In: *J. Geophys. Res.-Atmos.* 126.20. DOI: 10.1029/2021JD035331.

Nuijens, Louise and A. Pier Siebesma (2019). "Boundary layer clouds and convection over subtropical oceans in our current and in a warmer climate." In: *Curr. Clim. Change Rep.* 5.2, pp. 80–94. DOI: 10.1007/S40641-019-00126-X.

Orlanski, Isidoro (1975). "A rational subdivision of scales for atmospheric processes." In: *Bull. Am. Meteorol. Soc.* 56.5. URL: https://www.jstor.org/stable/26216020.

Peters, Karsten, Cathy Hohenegger, and Daniel Klocke (2019). "Different representation of mesoscale convective systems in convection-permitting and convection-parameterizing NWP models and its implications for large-scale forecast evolution." In: *Atmosphere* 10.9, p. 503. DOI: 10.3390/ATMOS10090503.

Provod, M., J. H. Marsham, D. J. Parker, and C. E. Birch (2016). "A characterization of cold pools in the West African Sahel." In: *Mon. Weather Rev.* 144, pp. 1923–1934. DOI: 10.1175/MWR-D-15-0023.1.

Redl, Robert, Andreas H. Fink, and Peter Knippertz (2015). "An objective detection method for convective cold pool events and its application to Northern Africa." In: *Mon. Weather Rev.* 143, pp. 5055–5072. DOI: 10.1175/MWR-D-15-0223.1.

Rio, C., F. Hourdin, J.-Y. Grandpeix, and J.-P. Lafore (2009). "Shifting the diurnal cycle of parameterized deep convection over land." In: *Geophys. Res. Lett.* 36, p. L07809. DOI: 10.1029/2008GL036779.

Rochetin, Nicolas, Cathy Hohenegger, Ludovic Touzé-Peiffer, and Najda Villefranque (2021). "A physically based definition of convectively generated density currents: Detec-

tion and characterization in convection-permitting simulations." In: *J. Adv. Model. Earth Sy.* 13.7. DOI: 10.1029/2020MS002402.

Romps, David M. and Nadir Jeevanjee (2016). "On the sizes and lifetimes of cold pools." In: *Q. J. Roy. Meteor. Soc.* 142, pp. 1517–1527. DOI: 10.1002/QJ.2754.

Ross, Andrew N., Adrian M. Tompkins, and Douglas J. Parker (2004). "Simple models of the role of surface fluxes in convective cold pool evolution." In: *J. Atmos. Sci.* 61, pp. 1582–1595. DOI: 10.1175/1520-0469(2004)061<1582:SMOTRO>2.0.CO;2.

Rotunno, R., J. B. Klemp, and M. L. Weisman (1988). "A theory for strong, long-lived squall lines." In: *J. Atmos. Sci.* 45, pp. 463–485. DOI: 10.1175/1520-0469(1988)045<0463:ATFSLL>2.0.CO;2.

Satoh, Masaki, Bjorn Stevens, Falko Judt, Marat Khairoutdinov, Shian-Jiann Lin, William M. Putman, and Peter Düben (2019). "Global cloud-resolving models." In: *Curr. Clim. Change Rep.* 5.3, pp. 172–184. DOI: 10.1007/S40641-019-00131-0.

Schlemmer, Linda and Cathy Hohenegger (2014). "The formation of wider and deeper clouds as a result of cold-pool dynamics." In: *J. Atmos. Sci.* 71, pp. 2842–2858. DOI: 10.1175/JAS-D-13-0170.1.

– (2016). "Modifications of the atmospheric moisture field as a result of cold-pool dynamics." In: *Q. J. Roy. Meteor. Soc.* 142, pp. 30–42. DOI: 10.1002/QJ.2625.

Siebesma, A. Pier, Sandrine Bony, Christian Jakob, and Bjorn Stevens, eds. (2020). *Clouds and climate: Climate science's greatest challenge*. 1st ed. Cambridge University Press. DOI: 10.1017/9781107447738.

Smagorinsky, J. (1963). "General circulation experiments with the primitive equations: I. The basic experiment." In: *Mon. Weather Rev.* 91.3, pp. 99–164. DOI: 10.1175/1520-0493(1963)091<0099:GCEWTP>2.3.CO;2.

Stevens, Bjorn et al. (2020). "The added value of Large-eddy and storm-resolving models for simulating clouds and precipitation." In: *J. Meteorol. Soc. Jpn.* 98.2, pp. 395–435. DOI: 10.2151/JMSJ.2020-021.

Stewart, I. D. and T. R. Oke (2012). "Local climate zones for urban temperature studies." In: *Bull. Am. Meteorol. Soc.* 93.12, pp. 1879–1900. DOI: 10.1175/BAMS-D-11-00019.1.

Stull, Roland B. (2017). *Practical meteorology: An algebra-based survey of atmospheric science*. UBC, p. 940. ISBN: 978-0-88865-176-1.

TE Connectivity (2015). *High humidity environments mini probe (MRBD)*. Last access: 7 October 2021. URL: https://www.te.com/commerce/DocumentDelivery/DDEController?Action=showdoc&DocId=Data+Sheet\%7FMRBD_10K3MRBD1\%7FA\%7Fpdf\%7FEnglish\%7FENG_DS_MRBD_10K3MRBD1_A.pdf\%7FGA10K3MRBD1.

Terai, C. R. and R. Wood (2013). "Aircraft observations of cold pools under marine stratocumulus." In: *Atmos. Chem. Phys.* 13, pp. 9899–9914. DOI: 10.5194/ACP-13-9899-2013.

Tompkins, Adrian M. (2001). "Organization of tropical convection in low vertical wind shears: The role of cold pools." In: *J. Atmos. Sci.* 58, pp. 1650–1672. DOI: 10.1175/1520-0469(2001)058<1650:OOTCIL>2.0.CO;2.

Torri, Giuseppe and Zhiming Kuang (2019). "On cold pool collisions in tropical boundary layers." In: *Geophys. Res. Lett.* 46, pp. 399–407. DOI: 10.1029/2018GL080501.

Torri, Giuseppe, Zhiming Kuang, and Yang Tian (2015). "Mechanisms for convection triggering by cold pools." In: *Geophys. Res. Lett.* 42, pp. 1943–1950. DOI: 10.1002/2015GL063227.

Touzé-Peiffer, Ludovic, Raphaela Vogel, and Nicolas Rochetin (2022). "Cold pools observed during EUREC4A: Detection and characterization from atmospheric soundings." In: *J. Appl. Meteorol. Clim.* 61.5, pp. 593–610. DOI: 10.1175/JAMC-D-21-0048.1.

Vaisala (2017). *Weather Transmitter WXT530 Series user guide*. Last access: 14 January 2021. URL: https://www.vaisala.com/sites/default/files/documents/WXT530-Users-Guide-M211840EN.pdf.

Vogel, Raphaela (2017). "The influence of precipitation and convective organization on the structure of the trades," PhD thesis. Universität Hamburg. Chap. 4, p. 124.

Vogel, Raphaela, Heike Konow, Hauke Schulz, and Paquita Zuidema (2021). "A climatology of trade-wind cumulus cold pools and their link to mesoscale cloud organization." In: *Atmos. Chem. Phys.* 21.21, pp. 16609–16630. DOI: 10.5194/ACP-21-16609-2021.

Wackernagel, Hans (2003). *Multivariate geostatistics: An introduction with applications*. 3rd ed. Springer, p. 387. ISBN: 3-540-44142-5.

Wakimoto, Roger M. (1982). "The life cycle of thunderstorm gust fronts as viewed with Doppler radar and rawinsonde data." In: *Mon. Weather Rev.* 110, pp. 1060–1082. DOI: 10.1175/1520-0493(1982)110<1060:TLCOTG>2.0.CO;2.

Wing, Allison A. (2019). "Self-aggregation of deep convection and its implications for climate." In: *Curr. Clim. Change Rep.* 5.1, pp. 1–11. DOI: 10.1007/S40641-019-00120-3.

Zuidema, Paquita, Giuseppe Torri, Caroline Muller, and Arunchandra Chandra (2017). "A survey of precipitation-induced atmospheric cold pools over oceans and their interactions with the larger-scale environment." In: *Surv. Geophys.* 38, pp. 1283–1305. DOI: 10.1007/S10712-017-9447-X.

de Szoeke, Simon P., Eric D. Skyllingstad, Paquita Zuidema, and Arunchandra S. Chandra (2017). "Cold pools and their influence on the tropical marine boundary layer." In: *J. Atmos. Sci.* 74, pp. 1149–1168. DOI: 10.1175/JAS-D-16-0264.1.

van den Heever, Susan C. et al. (2021). "The Colorado State University Convective CLoud Outflows and UpDrafts Experiment (C3LOUD-Ex)." In: *Bull. Am. Meteorol. Soc.* 102, E1283–E1305. DOI: 10.1175/BAMS-D-19-0013.1.

von Kármán, Theodore (1940). "The engineer grapples with nonlinear problems." In: *Bull. Am. Meteorol. Soc.* 46.8, pp. 615–683. DOI: 10.1090/S0002-9904-1940-07266-0.

## EIDESSTATTLICHE VERSICHERUNG

Hiermit erkläre ich an Eides statt, dass ich die vorliegende Dissertationsschrift selbst verfasst und keine anderen als die angegebenen Quellen und Hilfsmittel benutzt habe.

*Hamburg, den 15. August 2022*

Bastian Kirsch

# Hinweis / Reference

Die gesamten Veröffentlichungen in der Publikationsreihe des MPI-M
„Berichte zur Erdsystemforschung / Reports on Earth System Science“,
ISSN 1614-1199

sind über die Internetseiten des Max-Planck-Instituts für Meteorologie erhältlich:
**http://www.mpimet.mpg.de/wissenschaft/publikationen.html**

*All the publications in the series of the MPI -M*
*„Berichte zur Erdsystemforschung / Reports on Earth System Science“,*
*ISSN 1614-1199*

*are available on the website of the Max Planck Institute for Meteorology:*
***http://www.mpimet.mpg.de/wissenschaft/publikationen.html***